Surface Patterning and Rotordynamic Response of Annular Pressure Seals Used in Turbomachinery

Hanxiang Jin

Dissertation submitted to the faculty of the Virginia Polytechnic Institute and State University in partial fulfillment of the requirements for the degree of

Doctor of Philosophy
In
Engineering Mechanics

Alexandrina Untaroiu, Chair
Anne E. Staples
Traian Iliescu
Jonathan B. Boreyko
Costin D. Untaroiu

November 20th, 2019
Blacksburg, VA

Keywords: Fluid Dynamics, Annular Pressure Seals, Rotordynamics, Labyrinth Seals, Hole-pattern Seals, Reduced Order Modeling

Surface Patterning and Rotordynamic Response of Annular Pressure Seals Used in Turbomachinery

Hanxiang Jin

ABSTRACT

Rotordynamic instability problems in turbomachinery have become more important in recent years due to rotordynamic components with higher speeds and higher power densities. These features typically lead to increased instability risk in rotor dynamic components as fluids-structure interactions take place. In addition, critical damage of rotordynamic components can result from high level vibrations of supporting bearing system, where the reduced rotor speed can lead to system operating near the rotor critical speed. Therefore, increased accuracy in modeling of rotordynamic components is required to predict the potential instability issues in high performance rotordynamic design. The instability issue may potentially be eliminated in design stage by varying the characteristics of the unstable components. One such turbomachinery component is the annular pressure seal. The annular pressure seals are specifically designed to prevent the fluid leakage from high pressure stage to low pressure stage in turbomachinery. Typical annular pressure seals have two different flow regions, an annular jet-flow region between the rotor and stator, and cylindrical or circumferential indentions on the stator/rotor surface that serve as cavities where flow recirculation occurs. As the working fluid enters the cavities and recirculates, the kinetic energy is reduced, resulting in a reduction of leakage flow. The current challenge is to model with higher precision the interaction between the rotordynamic components and the working fluid. In this dissertation, this challenge was overcome by developing a hybrid Bulk Flow/CFD method to compute rotordynamic responses for the annular pressure seals. In addition, design of experiments studies were performed to relate the surface patterning with the resulting rotordynamic response for the annular pressure seals, in which several different geometry specifications were investigated. This study on annular pressure seal design generated regression models for rotordynamic coefficients that can be used as optimization guidelines. Research topics related to the annular pressure seals were presented in this dissertation as well. The reduced

order model of both hole-pattern seals and labyrinth seals were investigated. The results showed that the flow field representing the flow dynamics in annular pressure seals can be expressed as a combination of first three proper orthogonal decomposition modes. In addition, supercritical state of carbon dioxide (sCO_2) process fluid was examined as the working fluid in a preliminary study to better understand the effects on annular pressure seals. The results showed that the performance and stability in the annular pressure seals using sCO_2 as process fluid can both be improved.

Surface Patterning and Rotordynamic Response of Annular Pressure Seals Used in Turbomachinery

Hanxiang Jin

GENERAL AUDIENCE ABSTRACT

This dissertation focused on understanding the correlations between surface patterning and rotordynamic responses in the annular pressure seals. The annular pressure seals are a specific type of rotordynamic component that was designed to prevent the fluid leakage from high pressure stage to low pressure stage in turbomachinery. As the working fluid enters the cavities and recirculates, the kinetic energy is reduced, resulting in a reduction of leakage flow through the annular pressure seals. Rotordynamic instability becomes an issue that may be related to the annular pressure seals in some cases. In recent years, rotordynamic components with higher rotor speeds and higher power densities are commonly used in industrial applications. These features could lead to increased instability risk in rotor-bearing systems as fluids-structure interactions take place. Therefore, high precision modeling of the rotodynamic components is required to predict the instability issues in high performance rotordynamic design. The instability issue may potentially be eliminated in design stage by varying the characteristics of the potentially unstable components. In this study, the surface patterning and rotordynamic responses were investigated for several different annular pressure seal models with a hybrid Bulk Flow/Computational Fluid Dynamics method. This dissertation provides for the first time regression models for rotordynamic coefficients that can be used as optimization guidelines. Research topics related to the annular pressure seals were presented in this dissertation as well. The reduced order model of both hole-pattern seals and labyrinth seals were investigated. The results showed that the flow field representing the flow dynamics in annular pressure seals can be expressed as a combination of first three proper orthogonal decomposition modes. In addition, supercritical state of carbon dioxide (sCO_2) process fluid was examined to better understand the effects of working fluid on annular pressure seals. The results showed that the performance and stability in the annular pressure seals using sCO_2 as process fluid can both be improved.

ACKNOWLEDGMENTS

I would like to express my sincere appreciation to my supervisor Dr. Alexandrina Untaroiu for her expertise, guidance, encouragement and consistent support that helped me managed to overcome the difficulties in this research. Without her help, this work would not have been possible.

I am grateful to the Biomedical Engineering and Mechanics department for the support to complete my doctoral degree.

Special thanks to my friend Gen Fu for his help in my research.

At last, I would like to thank my parents for their love and support.

Table of Content

List of Figures

List of Tables

Chapter 1. Introduction

Rotordynamic instability problems in turbomachinery have become more important in recent years, because of the continuous trend towards higher speeds and higher power densities. These typically lead to an increase in the number and variety of fluids-structure interaction problems in pumps, turbines, and compressors. Instability in rotor-bearing systems can lead to high levels of vibration, which results in destruction of rotating machines or lost production due to reduced speeds and flow rates. Accurate characterization of instability drivers is vital in prediction of the stability, which allows for design changes to reduce deleterious effects. For instance, these changes include the alteration of the system component causing instability.

One such system component is the annular pressure seal. They are specifically design to minimize the leakage flow between high and low pressure sections in turbomachinery. Typical annular pressure seals have two distinct flow regions, an annular jet-flow region between the rotor and stator, and cylindrical or circumferential indentions on the stator/rotor surface that serve as cavities where flow recirculation occurs. As the working fluid enters the cavities and recirculates, its kinetic energy is reduced, resulting in a reduction of leakage flow rate through the seal. The current challenge is to accurately evaluate the interaction between the rotating parts and the surrounding fluid.

The surface patterning of the annular pressure seals is commonly considered to induce a significant effect on the overall performance. In this study, we hypothesize the surface patterning of the annular pressure seals has relative significant effects on the dynamic response as well. As a result, in order to improve the efficiency in terms of both leakage rate and dynamic responses, this dissertation is focused on developing an accurate and computational efficient analysis tool that will allow us to determine the co-dependence between seal design variables and the dynamic properties of the seal. Once the computational framework was developed, different types of annular pressure seals were considered to investigate the dynamics responses understand certain working conditions.

A sensitivity study will be performed to assess the influence seal's surface patterning on both leakage and dynamic response performance. The computational framework will include a combination of computational fluid dynamics (CFD) and bulk flow analysis, a design of experiments (DOE) technique, as well as a reduced order model for flow reconstruction. Different geometry variables were investigated for hole-pattern seals and labyrinth seals. Quadratic polynomial fittings were used to analyze the sensitivity of different design variables with respect to the different outputs. The previous studies were hardly able to give reliable dynamic response information when test data were not available or the complete analysis was very time consuming. Whereas, the hybrid bulk flow/CFD approach, combined with a reduced order model (ROM) proposed to be developed in this study, is introducing a method that balance the efficiency, computational time and resources, with an increased accuracy to assess the dynamic responses. This detailed analysis allows for a more in-depth understanding of the interaction effects from varying all of these design parameters altogether, as opposed to studying them as one variable at a time. Response maps generated from the calculated results is expected to illustrate the effects of each corresponding design parameter on seal leakage as well as the co-dependence among design parameters selected. The results of this study could provide guidance for improving future designs of the annular pressure seals.

1.1 Background

In turbomachinery, applications of non-contacting annular pressure seals to prevent leakage flow and increase machine efficiency are very common in rotordynamic systems either at the end of stages or in-between stages. Rotors in turbomachinery are usually operating at high speeds and a certain amount of leakage is allowable through the non-contacting annular pressure seals. The leakage flow is reduced by the conversion of available pressure head into dissipated kinetic energy. This is accomplished by forcing the fluid through a small restrictive gap, and then dissipating the kinetic energy in an expansion chamber before the next gap is encountered. Examples of the annular pressure seals are shown in Figure 1-1**Error! Reference source not found.**, in which the two images on the top are reprinted from [1].

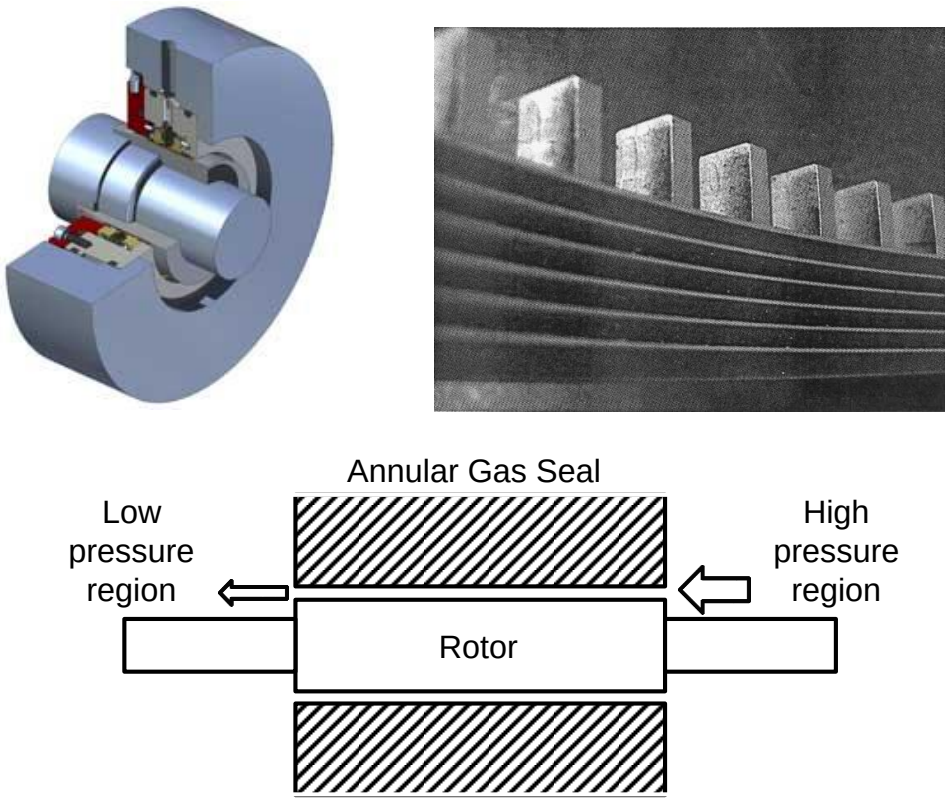

Figure 1-1: Annular Pressure Seals

Comparing to the leakage rate prediction, the rotordynamic responses is becoming a more important issue after decades of development in this field. As the requirement from industry for smaller size and lighter components, as well as higher performance of the turbomachine, the rotor system could be vulnerable to various excitations, including fluid flow excitation in components, such as the annular pressure seals.

The annular pressure seals with smooth rotor/honeycomb stator have been used since the 1960s to reduce the leakage between different pressure stages in compressors. Alford [2] in 1965, pointed out that a non-uniform pressure distributions in the labyrinth chambers around the rotor exerts forces on the shaft. However, with higher rotating speeds, under some conditions, such forces can result in an unstable outcome. Childs and Moyer [3] was the first to intentional use honeycomb seals for enhancement of rotordynamics in regard to vibration problems related to the High Pressure Oxygen Turbopump of the Space Shuttle Main Engine. In this case, a smooth stator/grooved rotor of stepped labyrinth seal was

switched to a standard honeycomb stator/smooth rotor seal, this study resolved vibration issues of synchronous and subsynchronous types. The equation of motion in rotor machinery was presented as well, which is

$$\begin{bmatrix} F_X \\ F_X \end{bmatrix} = \begin{bmatrix} K_{XX} & K_{XY} \\ K_{YX} & K_{YY} \end{bmatrix} \begin{bmatrix} X \\ Y \end{bmatrix} + \begin{bmatrix} C_{XX} & C_{XY} \\ C_{YX} & C_{YY} \end{bmatrix} \begin{bmatrix} \dot{X} \\ \dot{Y} \end{bmatrix} + \begin{bmatrix} M_{XX} & M_{XY} \\ M_{YX} & M_{YY} \end{bmatrix} \begin{bmatrix} \ddot{X} \\ \ddot{Y} \end{bmatrix} \quad \textbf{Eqn. 1-1}$$

Where displacement of the rotor is defined as *X*, *Y*; F_X and F_Y are the corresponding reaction forces on *X* and *Y* directions. The matrix of stiffness coefficient **K** is a measure of the resistance of the seal to the lateral (transverse) displacements of the shaft. The matrix of damping coefficients **C** represents the resistance of the seal to the transverse velocities in *X* and *Y* directions of the shaft in the seal, and the mass coefficient matrix **M** is a measure of the seal's resistance to the transverse acceleration of the shaft. The subscription XX and YY are used for direct terms, while the subscription XY and YX are used for cross-coupled terms

The forces developed by compressible gas flow labyrinth seals are much lower than the liquid seal or fluid film bearing counterparts with a factor of one order or higher. Further investigation discovered by Childs [4], indicated that the annular gas seals normally have negligible mass coefficients and these terms are neglected in the rotordynamic analysis. With a centered position assumption, Eqn. 1-1 reduces to

$$\begin{bmatrix} F_X \\ F_Y \end{bmatrix} = \begin{bmatrix} K_{XX} & K_{XY} \\ K_{XY} & K_{XX} \end{bmatrix} \begin{bmatrix} X \\ Y \end{bmatrix} + \begin{bmatrix} C_{XX} & C_{XY} \\ C_{XY} & C_{XX} \end{bmatrix} \begin{bmatrix} \dot{X} \\ \dot{Y} \end{bmatrix} \quad \textbf{Eqn. 1-2}$$

The rotor dynamic coefficients in this simplified equation are direct stiffness K_{XX}, cross-coupled stiffness K_{XY}, direct damping C_{XX} and cross-coupled damping C_{XY}. Where direct mass coefficient M_{XX} and cross-coupled mass coefficient M_{XY} are ignored. In addition, effective damping is a widely used single number measure of stability in a rotordynamic component, which is defined by

$$C_{eff} = C_{XX}\left(1 - \frac{K_{XY}}{\omega C_{XX}}\right) \quad \textbf{Eqn. 1-3}$$

Rotordynamic coefficients of seals carried out by Alford [2] for the annular pressure seals was not considering the details of the circumferential flow, however, a formula for aerodynamic cross-coupling stiffness was included. The first illustration of the rotordynamic coefficients were comprehensively analyzed in labyrinth seals by Kostyuk [5] in 1972. Kostyuk's analysis utilized compressible gas dynamics and the conservation of energy and momentum equations for individual labyrinth chamber. However, the change in cross-sectional area due to eccentricity was not considered by Kostyuk, which was directly related to parallel rotor displacements and cross-coupling. As a result, the model was not able to predict the cross-coupled stiffness, which was the most important quantity that contributed to instability.

In 1973, Hirs [6] published his bulk flow theory for turbulent flow in a lubricant film. It has come to be widely employed for seal analysis. Hirs' bulk-flow theory states that the shear stresses can be obtained through the mean velocity of flow relative to the wall. Hirs's bulk flow is a simple model, derived from Navier-Stokes equations, yet accounts for the turbulent effects. The use of this theory allows us to avoid the Reynolds averaging and Reynolds stresses normally included in the full Navier-Stokes equations. There are a number of existing seal models applying Hirs's bulk flow theory. Often they are classified based on the number of control volumes selected to describe the tooth section.

In 1980, Kostyuk's original model was expanded by Iwatsubo [7], where the variation of the gland cross section area due to rotor eccentricity was included. The resulting equations can be computed by finite difference method. A perturbation from the steady state was used to determine the rotordynamic coefficients. All subsequent "Kostyuk-based" analysis incorporate the time dependency of the area change as introduced by Iwatsubo. In 1986, Childs [8] further explored Iwatsubo's analysis by considering the variation of circumferential area resulted from eccentricity. Childs' analysis not only illustrated a comprehensive derivation of governing equations but also presented a new solution of rotordynamic equations. Several studies have been started afterward to further expand Child’s method [9-13].

In 1984, Wyssmann [14] introduced the first two control volume approach to achieve improvement on the results of previous analysis. The two-control-volume approach models the two axial flow regions. However, the area over the teeth is ignored. To gain more accuracy, a new control volume, covering the volume over the teeth, is taken into consideration. In 1988, Scharrer [15] extended Wyssmann's analysis by including the recirculation velocity into the analysis. In 1986, Rhode [16] presented CFD results, which used to illustrate the evaluation of shear stress in the models as well as recirculation velocity in the analysis. In 1990, Nordmann and Weiser [17] presented a three volume bulk flow method for labyrinth seals, in which the compressible, turbulent flow was included. The continuity, momentum and energy equations were established in every control volume. The description of the fluid shear stresses resulted from the jet flow and the vortex flow were developed as well. After that, several different publications further addressed the three control volume method [18-23].

The analytical methods were then followed by a series of experimental studies. In 1978, Stocker [24] performed a series of experiments in order to determine the aerodynamic performance of conventional labyrinth seals employing abatable and honeycomb lands. In 1980, Benckert and Watcher [25] performed extensive experimental investigations of the destabilizing forces caused by labyrinth seals. In 1983, Wright [26] presented a measurement of equivalent radial and tangential stiffness in a smooth rotor/grooved stator seals with one single tooth. In 1984, Leong and Brown [18] illustrated the same seal model as Wachter and Benchert as validation and extension of their work. In 1986, Childs and Scharrer [27] were the first to present the direct damping coefficients. They measured the rotordynamic coefficients for labyrinth seal with teeth-on-stator (TOS) type and teeth-on-rotor (TOR) type, and compared them under same working conditions. In 1988, Childs and Scharrer [9] redesigned their 1986 rig and pushed shaft speeds up to 16,000 rpm. In 1986, Kanemitsu and Ohsawa [28] presented rotordynamic analysis of 2,400 rpm rotor speed, multistage and interlocking labyrinth seals. In the same year, Hisa et al. [29]compared stepped type of labyrinth seals with standard type under the rotor speeds of 6,000 rpm. In, 1997, Marquette and Childs [30] presented validated high-speed rotor model of leakage

performance and rotordynamic coefficients in an annual liquid seal with and without shaft eccentricity. In 1997, Prasad [31] carried out comparison of computational investigation and experimental work to evaluate the leakage flow in straight-through type of labyrinth seals. In 1990s, Morrison et al [32, 33] used the laser to study 3D flow in a seven-cavity labyrinth seal. In 1997, Kwanka [34] investigated the rotordynamic influence of swirl brakes installed upstream of labyrinth seals of smooth stator and honeycomb surface patterning. In 1999, E.A. Soto [35] was the first to measure rotordynamic data for a labyrinth seal with shunt injection.

Compared to experimental work, Computational Fluid Dynamics (CFD) method is less expensive and time consuming than experimental work. The study of flow in seals using CFD packages, such as FLUENT, CFX, etc, have been used extensively since 1990s [36-46]. To further understand the phenomenon behind the fluid leakage reduction process, the characteristics of the flow field had to be included in the model. Traditional method to develop such a model is based on utilization of conservation laws for mass, momentum, and energy, which introduce governing equations consisting of significantly coupled large systems of partial differential equations (PDEs). These high dimension PDEs are hardly solvable by analytical methods, instead, numerical methods are commonly used to solve these equations. One of the difficulties to optimizing labyrinth seal geometry design is the huge time consumption for performing the CFD simulations. The CFD simulations boundary conditions include high angular velocities that lead to convergence problems. The solutions take very long time to converge in some of the cases.

To find the possible solutions for these issues, we developed a reduced-order model using proper-orthogonal decomposition and snapshot techniques based on previous studies related to different fields as reported in the literature. In late 1980s, Sirovich [47] presented the method of snapshots to study turbulence. In 1990, Kirby et al. [48] studied jet flow phenomenon using this method. Afterward, in 1995, Cizmas and Hall [49] developed two different descriptions of flow modeling, which are nonlinear/linear description for the mean flow/the small disturbance unsteady flow. In 1998, Ito and Ravindran [50] developed reduced-order models to study the essential physics in some typical problems. In 2003,

Cizmas et al. [51] used POD method to study the phenomenon of a fluidized bed. In 2012, Puragliesi and Leriche [52] presented the coherent structures in a heated cubical three-dimensional differentially cavity with POD method and snapshot technique for the velocity and temperature in the system. In 2013, Iliescu and Wang [53] developed a variational multiscale reduced order model for turbulent Navier-Stokes equations using POD method. In 2017, Iliescu et al [54] illustrated the numerical stability of reduced order models in convection-dominated stochastic systems.

1.2 Research Objectives

There are some main disadvantages for current methods to compute rotordynamic coefficients. For the Bulk flow method, lack of accuracy when test data are not available is the main issue, and it is caused by the use of empirical coefficients determined from experimental data. Full CFD method is more accurate compared to bulk flow method. However, it is much more time consuming, requiring steady state or transient CFD simulation for every case, which takes up to several days to obtain the results. To solve these issues, combining Bulk flow method and Full CFD method resulted in huge time saving compared to Bulk flow method with similar accuracy with Full CFD method. In addition, reduced order model can be of great help in CFD computation process. The three objective of the proposed research are:

(1) Develop a method to compute rotordynamic coefficients efficiently and with higher accuracy

The accurate prediction cases in Bulk flow method only comes from empirical coefficients with an experimental work of same model. Applying the empirical coefficients to another model usually resulted in huge difference compared to actual values. However, if the base state is determined by steady-state CFD analysis, then the friction factors are determined explicitly, an empirical factor is no longer necessarily required. During the CFD analysis, if reduced order model can be applied on the velocity vector basis, with some training simulation, the time consumption of the whole process will be further reduced. Combining Bulk flow, CFD and ROM, the method developed in this study would achieve both efficiency and accuracy.

(2) Investigate the effects of surface patterning of annular pressure seals on the dynamic response

The current industrial annular pressure seals design is mainly considering the performance in terms of leakage rate only. However, when smaller size and higher efficiency are required, the stability margins would become the main issue in the seal design. With the method developed in this study, investigation of the effects of surface patterning of annular pressure seals through a parameter sensitivity study will identify the main co-dependent design variables with influence on the rotordynamic response.

(3) Investigate the reduced order modeling of flow field reconstruction and application of supercritical state working fluid

The reduced order modeling allows construction of the detailed flow field with enough accuracy using only a few modes from the energy composition standpoint. This topic is an initial study for future use to reduce the simulation time in the annular pressure seals. Apart from that, the study of effects of different fluid media in the annular pressure seals are valuable for guiding future seal design. In this dissertation, the effects of supercritical fluid is also investigated as early understanding for future application.

By completing the three objectives, general guidelines of seal geometry design are illustrated to predict not only the performance but also the rotordynamic properties. Compared to previous methods, the method proposed in this study would achieve higher efficiency and higher accuracy.

1.3 Significance

This work is expected to provide an efficient method to evaluate the rotordynamic responses of the annular pressure seals with improved accuracy and efficiency compared to existing methods. Ultimately the presented method will allow to correlate the required surface patterning of the seal with a target dynamic response.

1.4 Outline

The dissertation is composed of six chapters, which are organized as follows. An introduction comprehensive review of the related work in the fields of the annular pressure seals with relative research techniques is discussed in Chapter I, along with the existing gaps that needs to be addressed.

In Chapter II, the details of methodology and techniques used in this research are presented. In particular, the development of a hybrid CFD/Bulk Flow method and Reduced Order Modeling (ROM) for flow field reconstruction, including the derivation of governing equations, proper orthogonal decomposition, and snapshot technique. Introduction of Computational Fluid Dynamics (CFD) and Design of Experiments (DOE) are presented as well for reference.

In Chapter III, case studies associated with hole-pattern seals are presented. This section includes investigation of elliptical shape of hole-pattern seals, investigation of alternately arranged hole-pattern seals, and investigation of hole-pattern seals combining with swirl brakes.

In Chapter IV, case studies associated with labyrinth seals are presented. This section includes investigation of geometry effects of groove shape for labyrinth seals, investigation of labyrinth seals combining with swirl brakes.

In Chapter V, some new methods used to investigate the annular pressure seals are presented, which include flow reconstruction using reduced order modeling and fluid media comparison for high pressure. The use of alternative fuel sources are becoming more common recently. Large density fluctuations of carbon dioxide in the supercritical region can be investigate for maintaining compressor inlet conditions close to the critical point, which can be used to reduce the ratio of compressor work to the back work.

Finally, Chapter VI contains a summary of the expected contributions of this work and ideas to extend them further.

Chapter 2. Methodology

2.1 Hybrid CFD/Bulk Flow Method Development

To improve Bulk Flow approach and eliminate the need of an empirical coefficient, the friction factor, the proposed hybrid method is presented here. The theoretical foundation of this method is the Bulk Flow model from Kleynhans' [46] for hole-pattern seals, which include the two-control volume bulk-flow model. The governing equations of a gas hole-pattern seal are:

$$0 = \frac{\partial}{\partial t}[\rho(H + \gamma_c H_d)] + \frac{1}{R}\frac{\partial}{\partial \theta}[\rho UH] + \frac{\partial}{\partial Z}[\rho WH] \quad \textbf{Eqn. 2-1}$$

$$0 = \rho H\frac{\partial W}{\partial t} + \frac{\rho UH}{R}\frac{\partial W}{\partial \theta} + \rho WH\frac{\partial W}{\partial z} + \tau_{sz} + \tau_{rz} \quad \textbf{Eqn. 2-2}$$

$$0 = \rho H\frac{\partial U}{\partial t} + \frac{\rho UH}{R}\frac{\partial U}{\partial \theta} + \rho WH\frac{\partial U}{\partial z} + \tau_{s\theta} + \tau_{r\theta} \quad \textbf{Eqn. 2-3}$$

$$P = \rho z_c R_g T \quad \textbf{Eqn. 2-4}$$

The boundary conditions of the inlet and the outlet can be obtained through Bernoulli's equation considering the contraction and expansion effects:

$$P_i - P(0) = \frac{1 + \xi_i}{2}\rho W^2(0) \quad \textbf{Eqn. 2-5}$$

$$P_e - P(L) = \frac{1 - \xi_e}{2}\rho W^2(L) \quad \textbf{Eqn. 2-6}$$

The wall shear stress can be obtained through Hirs' viscous shear stress model:

$$\tau_{sz} + \tau_{rz} = \frac{1}{2}\rho W[U_s f_s + U_r f_r] \quad \textbf{Eqn. 2-7}$$

$$\tau_{s\theta} + \tau_{r\theta} = \frac{1}{2}\rho[UU_s f_s + (U - R\omega)U_r f_r] \quad \textbf{Eqn. 2-8}$$

The solution of the bulk-flow equations can be achieved from perturbing the flow variables $\phi = [H,W,P,U]$ as

$$\frac{1}{2}\rho\phi = \phi_0(z) + \varepsilon\phi_1(z,\theta,t) \qquad \textbf{Eqn. 2-9}$$

In this equation, ε is the eccentricity ratio of the rotor from center of rotation. The separated equations are then obtained as terms containing ε^0 (zeroth order equations) and terms containing ε^1 (first order equations). The flow the unperturbed system is model by the zeroth order equations, whereas the perturbation effects due to the rotor whirling motion (from the eccentricity of rotor) is model by the first order equations represent. In this study, the zeroth order equations can be replaced by CFD results and therefore dropped.

Next, the first order equations are nondimensionalized. The expression of clearance for the orbit of the rotor is given by:

$$h_1 = -xcos(\Omega t)\cos(\theta) - ysin(\Omega t)\sin(\theta) \qquad \textbf{Eqn. 2-10}$$

And the assumed harmonic response is:

$$\begin{aligned}\bar{\phi}_1 = [\bar{\phi}_{xc}\cos(\bar{\Omega}\bar{t}) + \bar{\phi}_{xs}\sin(\bar{\Omega}\bar{t})]\cos(\theta) \\ + \left[\bar{\phi}_{yc}\cos(\bar{\Omega}\bar{t}) + \bar{\phi}_{ys}\sin(\bar{\Omega}\bar{t})\right]\sin(\theta)\end{aligned} \qquad \textbf{Eqn. 2-11}$$

Substituting into the first order equations and balancing the coefficients of $\cos(\bar{\Omega}\bar{t})$, $\sin(\bar{\Omega}\bar{t})$, $\cos(\theta)$, and $\sin(\theta)$ gives 12 ordinary differential equations of first order.

Since repeated pattern exists in a hole-pattern seal, therefore full circle CFD model can be replaced by sector model with periodic boundary conditions when obtaining the unperturbed base state. In this study, the wall shear stress is not defined in some locations on the stator surface, however, the shear stress on stator wall can be obtained through axial momentum equation of the zeroth order:

$$0 = \rho_0 W_0 H_0 \frac{dW_0}{dZ} + H_0 \frac{dP_0}{dZ} + \tau_{sz} + \tau_{rz} \quad \textbf{Eqn. 2-12}$$

In addition, the zeroth order boundary conditions can be used to obtain the coefficients of inlet loss and exit recovery:

$$P_i - P_0(0) = \frac{1+\xi_i}{2}\rho_0 W^2(0) \quad \textbf{Eqn. 2-13}$$

$$P_0(L) - P_e = \frac{1-\xi_e}{2}\rho_0 W^2(L) \quad \textbf{Eqn. 2-14}$$

Then, the friction factors can be obtained from Hirs' relationship Equation Eqn. 2-7 and Eqn. 2-8. An explicit friction factor model is not required. Without loss of generality, the flow variables are nondimensionalized. At last, all variables required for the perturbation analysis are obtained and the first order equations can be solved

$$P_0(L) - P_e = \frac{1-\xi_e}{2}\rho_0 W^2(L) \quad \textbf{Eqn. 2-15}$$

Where

$$\psi_j = [w_{xc}\ w_{xs}\ w_{yc}\ w_{ys}\ p_{xc}\ p_{xs}\ p_{yc}\ p_{ys}\ u_{xc}\ u_{xs}\ u_{yc}\ u_{ys}] \quad \textbf{Eqn. 2-16}$$

With the boundary conditions

$$\boldsymbol{p_1}(0) = -\frac{1+\xi_i}{2}[p_1(0)w_0^2(0) + 2p_0(0)w_0(0)\boldsymbol{w_1}(0)] \quad \textbf{Eqn. 2-17}$$

$$\boldsymbol{p_1}(1) = -\frac{1-\xi_e}{2}[p_1(1)w_0^2(1) + 2p_0(1)w_0(1)\boldsymbol{w_1}(1)] \quad \textbf{Eqn. 2-18}$$

Where

$$\boldsymbol{p_1}(1) = [p_{xc}\ p_{xs}\ p_{yc}\ p_{ys}]^T \quad \textbf{Eqn. 2-19}$$

$$\boldsymbol{w_1}(1) = [w_{xc}\ w_{xs}\ w_{yc}\ w_{ys}]^T \quad \textbf{Eqn. 2-20}$$

There are 4 boundary conditions left, which are $\boldsymbol{w_1} = 0$. In choked flow, $\boldsymbol{p_1}(1)$ can be replaced by $\boldsymbol{w_1}(1) = 0$. The outlet isothermal Mach number is constant in this case.

As a result, 12 linear differential equations of first order can be solved with bvp5c function in Matlab. The fluid forces are frequency-dependent, which can be obtained through integration of the first order pressure field over the rotor surface:

$$\boldsymbol{F}(\Omega) = -\pi \left[\frac{LRP_i}{C_a}\right] \int_0^1 \boldsymbol{p}_1 dz \quad \textbf{Eqn. 2-21}$$

Where

$$\boldsymbol{F} = [F_{xc}\ F_{xs}\ F_{yc}\ F_{ys}]^T \quad \textbf{Eqn. 2-22}$$

If the rotor is symmetric and the working fluid is gas, the governing equation of rotordynamics can be given by:

$$\begin{bmatrix} C(\Omega) & c(\Omega) \\ c(\Omega) & C(\Omega) \end{bmatrix} \begin{bmatrix} \dot{x} \\ \dot{y} \end{bmatrix} + \begin{bmatrix} K(\Omega) & k(\Omega) \\ k(\Omega) & K(\Omega) \end{bmatrix} \begin{bmatrix} x \\ y \end{bmatrix} = \begin{bmatrix} -F_N(\Omega) \\ -F_T(\Omega) \end{bmatrix} = \begin{bmatrix} F_{xc}(\Omega) + F_{ys}(\Omega) \\ F_{yc}(\Omega) - F_{xs}(\Omega) \end{bmatrix} \quad \textbf{Eqn. 2-23}$$

Where

$$x = r_0 \cos(\theta) \cos(\Omega t) \quad \textbf{Eqn. 2-24}$$

$$y = r_0\, sin(\theta)\, sin\ (\Omega t) \quad \textbf{Eqn. 2-25}$$

Define $t = 0$ in the whirling motion orbit and apply harmonic balance on $\cos(\theta)$ and $\sin(\theta)$ terms, the rotordynamic coefficients of a gas hole-pattern seal are

$$K(\Omega) = -\frac{F_{xc}(\Omega)}{r_0}, \qquad C(\Omega) = -\frac{F_{xs}(\Omega)}{r_0}$$
$$k(\Omega) = -\frac{F_{xc}(\Omega)}{r_0}, \qquad c(\Omega) = -\frac{F_{ys}(\Omega)}{r_0} \qquad \textbf{Eqn. 2-26}$$

and the effective coefficients are

$$K_{eff}(\Omega) = K(\Omega) - \Omega c(\Omega) \qquad \textbf{Eqn. 2-27}$$

$$C_{eff}(\Omega) = C(\Omega) - \frac{k(\Omega)}{\Omega} \qquad \textbf{Eqn. 2-28}$$

2.2 Reduced Order Model for Flow Field Reconstruction

In this study, Reduced Order Modeling used in flow field reconstruction is considered to better understand the energy distribution in the seal clearance region and provide an additional mean to improve the seal design. The scalar functions $u(\boldsymbol{x}, t_i)$ $(i = 1,2, \dots, M)$, which are parameterized by t_i, can be assumed to form a linear infinite-dimensional Hilbert space L^2 on a domain D bounded by subset of $\boldsymbol{R}^n$

The time-average of the sequence, from Cizmas and Hall [49], is defined by

$$\bar{u}(\boldsymbol{x}) = \langle u(\boldsymbol{x}, t_i) \rangle = \frac{1}{M}\sum_{i=1}^{M} u(\boldsymbol{x}, t_i) = \sum_{i=1}^{M} a_k(t_i)\phi_k(\boldsymbol{x}) \qquad \textbf{Eqn. 2-29}$$

The orthogonal basis functions $\phi_k(\boldsymbol{x})$ is independent of time, and orthogonal amplitude coefficients $a_k(t_i)$ is time dependent. These terms can be extracted by POD method to reconstruct the function. In this case, without loss of generality, $\bar{u}(\boldsymbol{x})$ can be assumed as zero.

The optimum condition can be reduced to the eigenvalue problem

$$\int_{\boldsymbol{D}} \langle u(\boldsymbol{x})u^*(\boldsymbol{y})\rangle \phi(\boldsymbol{y})dy = \lambda\phi(\boldsymbol{x}) \qquad \textbf{Eqn. 2-30}$$

Where $\boldsymbol{x}, \boldsymbol{y} \in \boldsymbol{D}$, and optimal basis functions $\{\phi_k\}$ are the eigenfunctions of this integral, which can be obtained by the averaged autocorrelation function

$$\langle \boldsymbol{u}(\boldsymbol{x})\boldsymbol{u}^*(\boldsymbol{y})\rangle = \boldsymbol{R}(\boldsymbol{x},\boldsymbol{y}) = \frac{\boldsymbol{1}}{\boldsymbol{M}}\sum_{\boldsymbol{i=1}}^{\boldsymbol{M}} \boldsymbol{u_i u_i^T} \qquad \textbf{Eqn. 2-31}$$

where the vector

$$\boldsymbol{u_i} = \boldsymbol{u}[\boldsymbol{x}, \boldsymbol{t_i}] = [\boldsymbol{u}(\boldsymbol{x_1}, \boldsymbol{t_i}), \boldsymbol{u}(\boldsymbol{x_2}, \boldsymbol{t_i}), \dots, \boldsymbol{u}(\boldsymbol{x_N}, \boldsymbol{t_i})]^{\boldsymbol{T}} \qquad \textbf{Eqn. 2-32}$$

The integral domain D is $(x_1, x_2, \dots, x_N)$, where x_j is the jth grid point.

If the number of data set for the spatial domain N is higher compared with the observation M, the snapshots method can be used to find the eigenvector of ROM from Sirovich [47]:

$$\boldsymbol{\phi_k} = \sum_{\boldsymbol{i=1}}^{\boldsymbol{M}} \boldsymbol{v_i^k u_i}, \qquad \boldsymbol{k} = \boldsymbol{1, 2, \dots, M} \qquad \textbf{Eqn. 2-33}$$

Considering the equation $(\boldsymbol{x}, \boldsymbol{y})\phi(\boldsymbol{y}) = \lambda\phi(\boldsymbol{y})$, if C is defined as a $M \times M$ symmetric matrix $\phi(\boldsymbol{y})[C_{ij}] = \frac{1}{M}(\boldsymbol{u}_i \cdot \boldsymbol{u}_j)$, the eigenvector of this equation can be solved from

$$\boldsymbol{Cv} = \boldsymbol{\lambda v} \qquad \textbf{Eqn. 2-34}$$

Once the eigenvectors of matrix were calculated, the POD modes are derived, a smaller set of ODEs can be obtained by applying the Galerkin method on a set of PDEs.

For flow field captured by POD of numerical simulation or experimental measurement, the relative energy of mode is defined by

$$E_k = \frac{\lambda_k}{E} = \lambda_k \Big/ \sum_{j=1}^{M} \lambda_j \qquad \text{Eqn. 2-35}$$

where E is the total energy.

2.3 Computational Fluid Dynamics

Computational fluid dynamics (CFD) is a division of fluid mechanics which utilizes numerical analysis to test and fix issues that exist in fluid flows. Computers have been utilized to do the calculations needed to replicate the fluid flow, and the interaction to boundaries with the working fluid. Solutions with higher accuracy had been achieved by higher speed computers recent years. Continuing exploration yields applications that enhances the precision and rate of simulation cases, for examples, turbulence and transient flows. The results of CFD can be validated by experimental work. Even previous performed experimental study can be used as comparison data for current CFD simulations.

CFD is commonly used in various fluid studies, for instance, aerodynamics, turbomachinery, weather prediction, industrial application, and natural science. Recent rotor dynamics response analysis are commonly involved with CFD to achieve higher accuracy.

2.4 Design of Experiments

The design of experiments (DOE) study could be the design of any endeavor that aims to describe or explain the variation of responses under assumptions to change the range of

input data. The expression is connected with experiments in which conditions of influences can be observed to reflect the variation.

At least one independent variable (or more) can be utilized to influence the responses in a design of experiment study, which is termed as “design variables” or “input variables”. The responses subject to changes from the variation of the design variables are referred to as “response variables” or “output variables”. In addition, some of the variables in a design of experimental study could be defined as constant parameters to exclude their effects to the response variables. In a design of experiments study, apart from corresponding dependent and independent design variables, optimization under the potential constraints between design variables can be included as well.

Issues related to validation and reliability may arise during a design of experiments study. Potential solution to these issues including carefully dealing with measurement mistakes and selection of design variables. The goal is to achieve proper precision in statistics.

In this study, design of experiments is used to obtain the effects of factors defining the geometry on the leakage and rotordynamic responses of the annular pressure seals. The geometrical characteristics selected are studied to find the relative parameter sensitivity for shape effects. The design variables are used to generate a design space consisting of a certain number design points. For each design point, a CFD simulation is performed to calculate the leakage rate and then the previous proposed bulk-flow code is used to calculate the corresponding rotordynamic coefficients. The DOE process, including the CFD simulations and the result analysis, is performed using ANSYS and Design Expert software. Quadratic polynomial fitting is then used to analyze the sensitivity of different design variables with respect to different outputs.

The CFD simulation could be further simplified using the proposed reduced order model. With some training transient simulations, the further CFD simulation in same geometry category can be generated with previous obtained vector basis.

Chapter 3. Hole-Pattern Seals

Hole-pattern annular gas seals have proven to be very effective in reducing leakage flow between high and low pressure sections in turbomachinery. This type of seal has two distinct flow regions: an annular jet-flow region between the rotor and stator, and cylindrical indentions in the stator that serve as cavities where flow recirculation occurs. As the working fluid enters the cavities and recirculates, its kinetic energy is reduced, resulting in a reduction of leakage flow rate through the seal. The geometry of the cylindrical cavities has a significant effect on the overall performance of the seal.

In practice, honeycomb seals can be simplified as hole-pattern seals to reduce the cost and difficulty when manufacturing the actual product. In addition, to reduce the damage caused by the potential rub between rotor and stator, soft materials are preferred. For instance, aluminum is commonly used as stator material for hole-pattern seals.

3.1 Elliptical Hole-Pattern Seals

In this case study, the effects of elliptical shape hole pattern geometry on the leakage and dynamic response performance of an industry-relevant hole-pattern seal design are investigated using a combination of computational fluid dynamics (CFD), hybrid bulk flow/CFD analysis, and a design of experiments technique. The design space was defined by varying the values of five geometrical characteristics: the major and minor radius of hole, the angle between the major axis and the axis of the seal, the spacing between holes along the seal axis, and hole spacing in the circumferential direction. Quadratic polynomial fitting was used to analyze the sensitivity of different design variables with respect to the different outputs. This detailed analysis allowed for a greater understanding of the interaction effects from varying all of these design parameters together, as opposed to studying them one variable at a time. Response maps generated from the calculated results demonstrate the effects of each design parameter on seal leakage, as well as the co-dependence between the design parameters. The data from this analysis was also used to generate linear regression models that demonstrate how these parameters affect the leakage rate and the dynamic coefficients, including the effective damping.

3.1.1 Computation Model and Parametrization

The baseline hole-pattern seal model geometry and operating characteristics for this study were selected from the literature. The baseline seal is 86 mm in length. The seal rotor diameter is 114.34 mm with a radial clearance in the jet flow region of 0.2 mm. There is 0.8 mm between the inlet to the seal jet flow region and the first row of holes and a minimum of 0.8 mm to the outlet from the last row of holes. The full 3-dimensional model of the seal can be seen in Figure 3-1. The working fluid is air modeled as an ideal gas at a temperature of 17.4 °C to match the experimental data. The hole-pattern features are on the stator surface while the rotor surface is smooth. The holes are uniformly distributed on the seal inner surface in both axial and circumferential directions.

This study employs a central composite design in five factors that has been reduced by application of fractional factorial method, which is a subset of all the combinations of possible values of design variables [55-57]. The fractional factorial design is widely used in statistics and tests. The design space is defined by varying the values of five geometrical characteristics. The parameterization of the base model includes: the major radius of holes (a), the ratio of major axis radius to minor axis radius (r_{ab}, where minor radius $b = a \cdot r_{ab}$), the angle between major axis of elliptical shape holes and axial direction of seals (θ), the number of holes in axial direction (n_a), and the number of holes in circumferential direction (n_c). The only constraint in this design space is that the holes are not allowed to overlap with each other. This constraint is automatically satisfied if the space between two adjacent holes is greater than zero. The parameterized model is shown in Figure 3-2(a). The angle between the major axis of the elliptical shape holes and the axial direction of the seals is varied from negative 75° to positive 75°. The number of holes in axial direction and number of holes in circumferential direction are determined by varying the spaces between the holes in both directions afterward.

This constraint is achieved by specifying the distance between the holes in axial direction and specifying the distance between a hole in the first axial row and its nearest neighborhood in the second row, which is illustrated in Figure 3-2(b). Since this study is not targeting the optimal design and is mainly focused on the sensitivity of the geometrical

parameters and their effects on the responses, the values of design variables only vary in a certain range around the baseline value. For instance, the range of the major axis radius and minor axis radius lies in the range of +100% and -50% of the radius for the baseline model. The tilt angle range also covers reasonable values in order to reduce the number of potential unfeasible designs. For the space between two consecutive holes, the values selected ensure that they do not interfere nor will the space be too large. In addition, the holes will not exist if Ra<0, so the major axis length and minor axis length have to be greater than zero. Figure 2(b) shows an example of the fluid domain for a particular elliptical hole-pattern seal geometry. As can be seen in Fig. 2a), the design space is uniquely determined by the major radius of holes (a, 5 levels), the ratio of minor radius to major radius (r_{ab}, 5 levels), the tilt angle (θ, 11 levels), the ratio of space to radius in axial direction ($r_a = S_a/R_a$, 5 levels), and the ratio of space to radius in offset direction ($r_r = S_r/R_r$, 5 levels). Note that the actual design variables used are n_a and n_c, which are derived from r_a and r_r, respectively. The depth of hole is kept constant for all the cases since literature show that it has only a marginal influence on the performance of hole-pattern seals [58]. For the parameter sensitivity study, each of the design variables is discretized into 5 levels, except the tilt angle θ, which is discretized into 11 levels for a better resolution. The geometrical parameters selected to be constant in this analysis are listed Table 3-1, while details of the design variables selected are shown in Table 3-2.

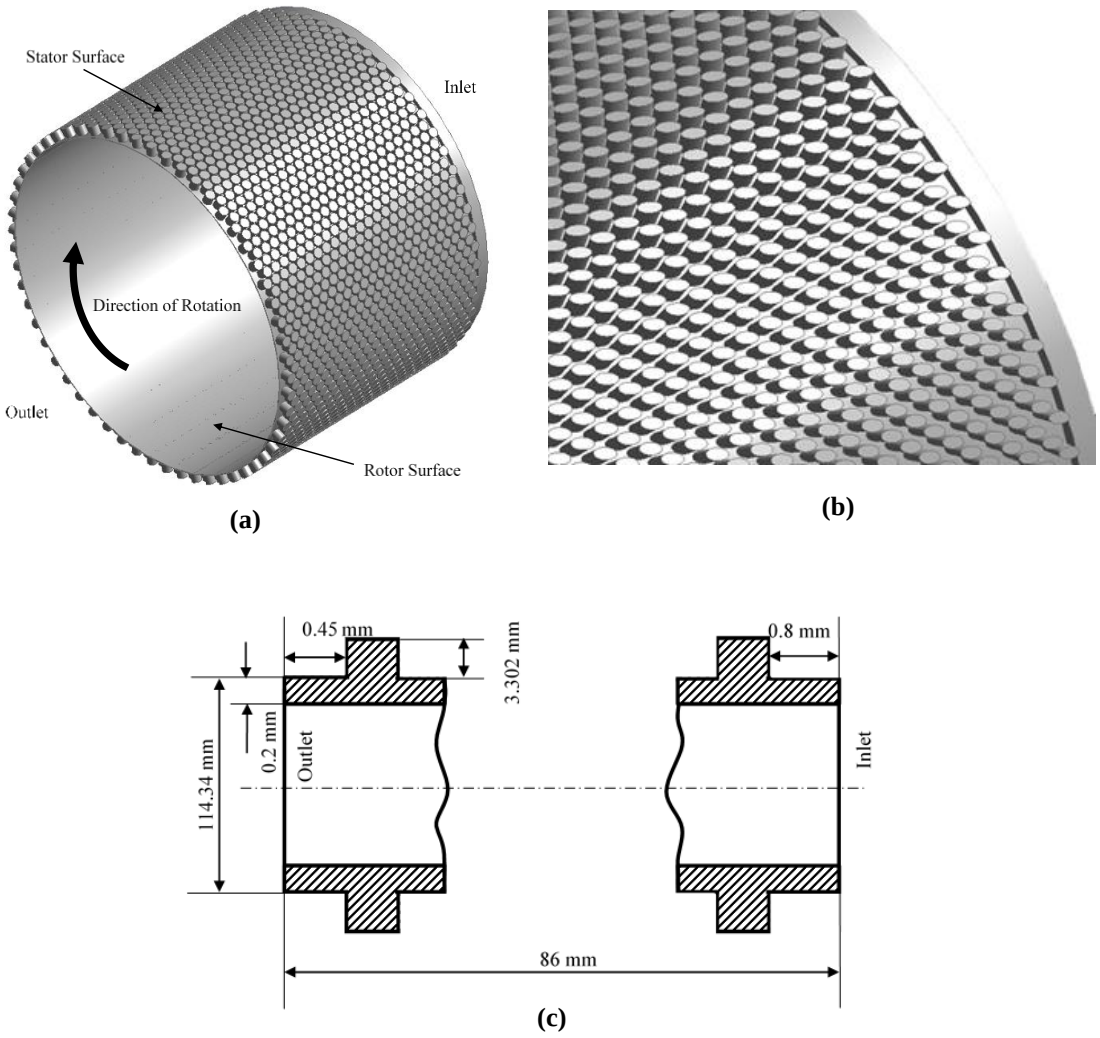

Figure 3-1: Seal Geometry (a) Fluid domain of baseline model, (b) surface pattern of a design point, (c) Cross-section view of baseline model

Table 3-1: Constant Parameters – Elliptical Hole-Pattern Seals

Parameter	Description	Base Value
Dr	Rotor Diameter	114.34 [mm]
Cr	Radial Clearance of Seal	0.204 [mm]
Ls	Seal Length	86 [mm]
Ds	Seal Diameter	114.74 [mm]
H	Depth of Holes	3.302 [mm]
δ_1	Space between Inlet and Holes	0.8 [mm]
δ_2	Space between Outlet and Holes	0.45 [mm]

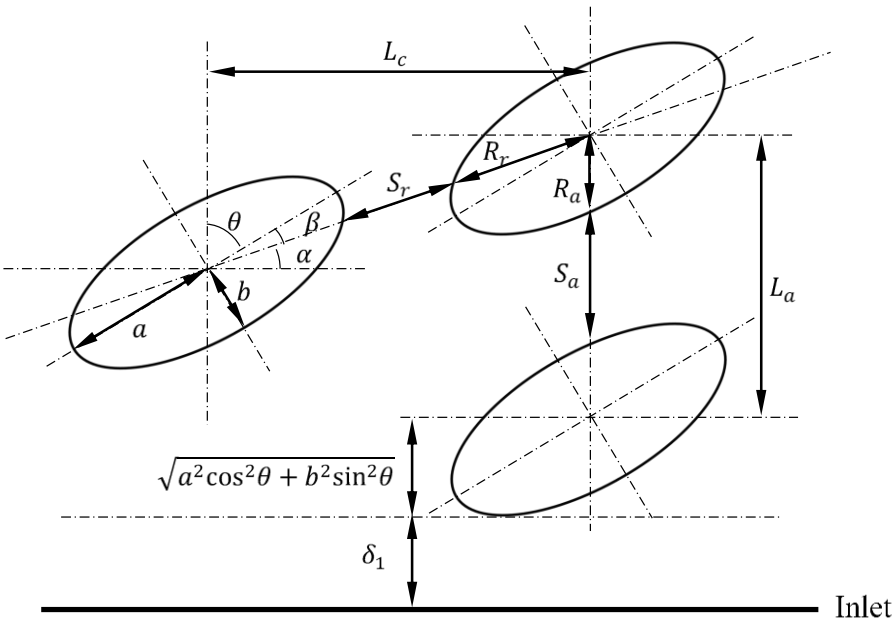

(a)

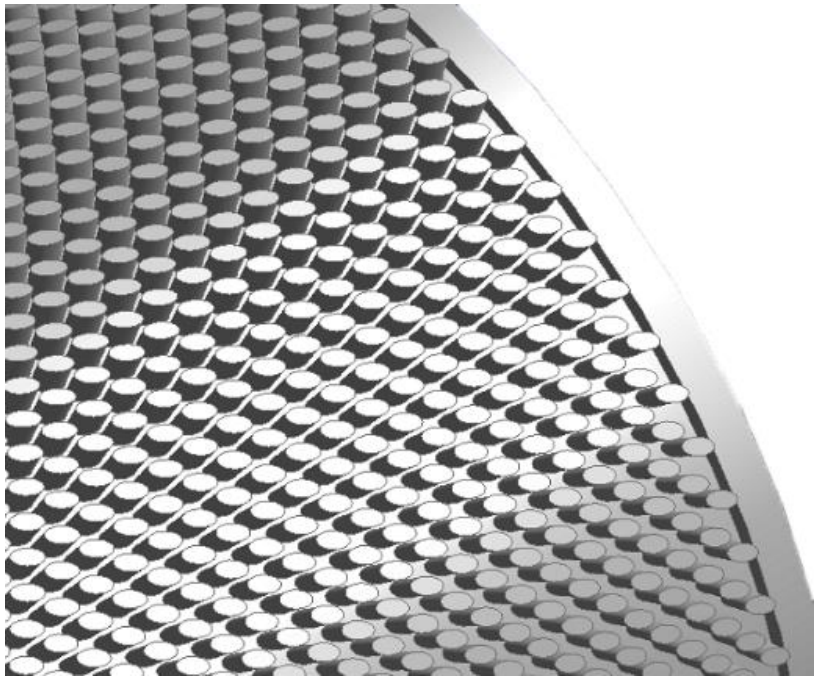

(b)

Figure 3-2 Illustration of (a) geometry variables and constraints for the design space and (b) example of elliptical shape surface patterning obtained through parametrization

Table 3-2: Design Variables – Elliptical Hole-Pattern Seals

Parameter	Description	Base Value	List of Feasible Values in the Design Space
a	Major Radius	1.5875 [mm]	1.5875, 1.984375, 2.38125, 2.778125, 3.175 [mm]
r_{ab}	Ratio of Minor Radius to Major Radius	1	0.5, 0.58, 0.66, 0.74, 0.82
θ	Tilt Angle	0 [°]	-70, -56, -42, -28, -14, 0, 14, 28, 42, 56, 70 [°]
r_a (determines n_a)	Ratio of Space to Radius in Axial Direction	0.277	0.15, 0.25, 0.35, 0.45, 0.55
r_r (determines n_c)	Ratio of Space to Radius in Offset Direction	0.277	0.15, 0.25, 0.35, 0.45, 0.55

As a result, the full factorial design includes 5×5×11×5×5=6,875 design points. Since each CFD simulation takes at least several hours to complete, testing all the possible combinations is impractical. Thus, the Kennard-Stone algorithm is employed to extract the most representative 68 design points among a list of 6,875 design points resulting from the full factorial design. The Kennard-stone algorithm is sequential and consists of maximizing the Euclidean distances between the newly selected design points and the ones already selected. An additional design point is designated by calculating for each design point that is not selected, the distance to each selected compound, and by maximizing the distance to the closet design point already selected [59-61]. In addition, the design space is generated with non-dimensionalized values. As a result, the Eulerian distance calculated in Kennard-Stone algorithm between two adjacent values for all design variables is always 1 when generating the design space. The values of design variables are converted back from non-dimensionalized values after the design space is generated to facilitate CAD updates, CFD simulations, and post-processing the results. Although the dimensionality could be removed by normalizing with the baseline value, this was a necessary step to ensure consistency and easier comparison with the baseline values, since the number of holes in axial and circumferential direction is converted using intermediate design variables during this automated process.

Based on the design variables selected, the following equations are derived to automatically impose constraints, so that the potentially unfeasible designs are removed from the design space.

$$R_a = \frac{ab}{\sqrt{a^2\cos^2\theta + b^2\sin^2\theta}} \quad \textbf{Eqn. 3-1}$$

$$n_a = \frac{L_s - \delta_1 - \delta_2 - 2\sqrt{a^2\cos^2\theta + b^2\sin^2\theta}}{2R_a + S_a} \quad \textbf{Eqn. 3-2}$$

$$L_a = \frac{L_s - 2\sqrt{a^2\cos^2\theta + b^2\sin^2\theta}}{n_a - 1} \quad \textbf{Eqn. 3-3}$$

$$\tan\alpha = \frac{L_a}{2L_c} \quad \textbf{Eqn. 3-4}$$

$$\beta = \frac{\pi}{2} - |\theta| - \alpha \quad \textbf{Eqn. 3-5}$$

$$L_c^2 + \frac{L_a^2}{4} = \frac{4a^2b^2(1+r_r)^2}{a^2\cos^2\theta + b^2\sin^2\theta} \quad \textbf{Eqn. 3-6}$$

$$n_c = \frac{\pi D}{2L_c} \quad \textbf{Eqn. 3-7}$$

where α, β, and L_c have to be solved for simultaneously since L_c is an implicit parameter.

3.1.2 CFD Model and Numerical Analysis

Since the CFD model is periodic with respect to the axis of rotation, the fluid domain is reduced to $1/n_c$ fluid domain sector. A mesh independence study is performed to ensure a robust analysis domain. As a result, a 2.17 million grid elements model showed a good balance between the computational time and the accuracy of the CFD solution and is selected to discretize the base seal model. The subsequent meshes for each individual simulation are then generated automatically according to the mesh sizing specifications that produced the 2.17 million mesh for the baseline geometry. The mesh independence study shows that reducing the number of grid elements in half (1.11 million grid elements) results in a 5% difference in leakage rate value while increasing the number of elements to 4.32 million results in a less than 2% difference on this performance indicator. The alteration of the number of elements in the model is achieved by specifying the maximum

element size in the mesh setup and automatically refinement for elements near the rotor surface. The mesh density inside the cavity will increase evenly while the maximum element size is decreased. Similarly, the mesh density near the rotor surface is also increased evenly as the maximum element size is decreased, but not as fast as the increase of the mesh density inside the cavity. The mesh is shown in Figure 3-3(a) with a detail view near rotor surface in Figure 3-3(b). Unstructured mesh with refinement of element size near the rotor surface is used to capture the flow characteristics in the jet flow region. Selection made for the turbulence model and near-wall treatment to be used in the simulations allows for the y+ value to be greater than 11. The average y+ value is approximately 70 and is found to have a direct correlation with the thickness of the first mesh layer above the rotor wall and the number of inflation layers used to discretize the jet flow region, which is the narrow gap between the rotor and the stator. Once the distance of the first node above the rotor wall is set in the mesh setup, there is relatively low variation in the resulting y+ value. The use of tetrahedral cells, which are numerically inferior to hexahedral grid elements, inside the seal holes was necessary, as the “swept” command in the meshing program failed for a large number of cases due to the curvature of the rotor surface [62]. The CAD model is a sector and as a part of an annulus, the rotor and stator’s surface is not perfectly flat. This slight curvature creates problems when automated generation of both the CAD and mesh is selected. The unstructured mesh is adopted in this study since the sweep method showed to fail for a large part of the feasible geometries considered in the design space.

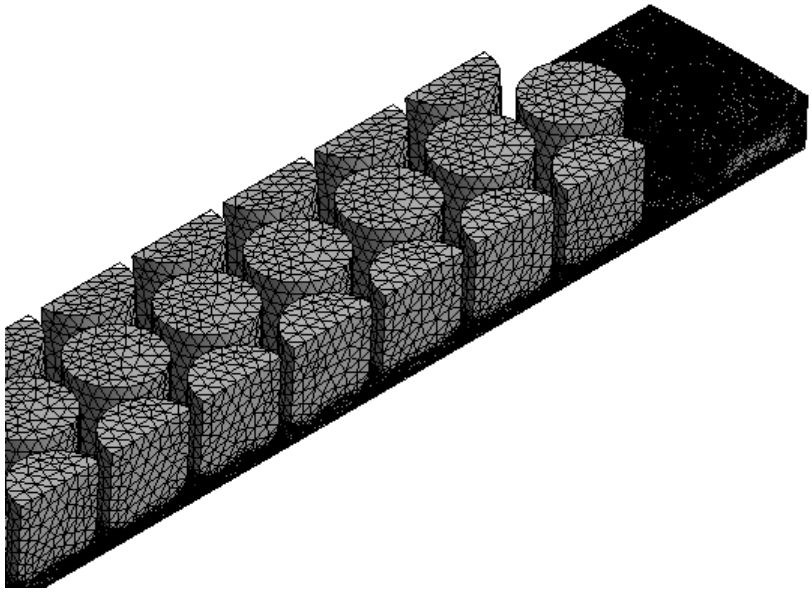

(a)

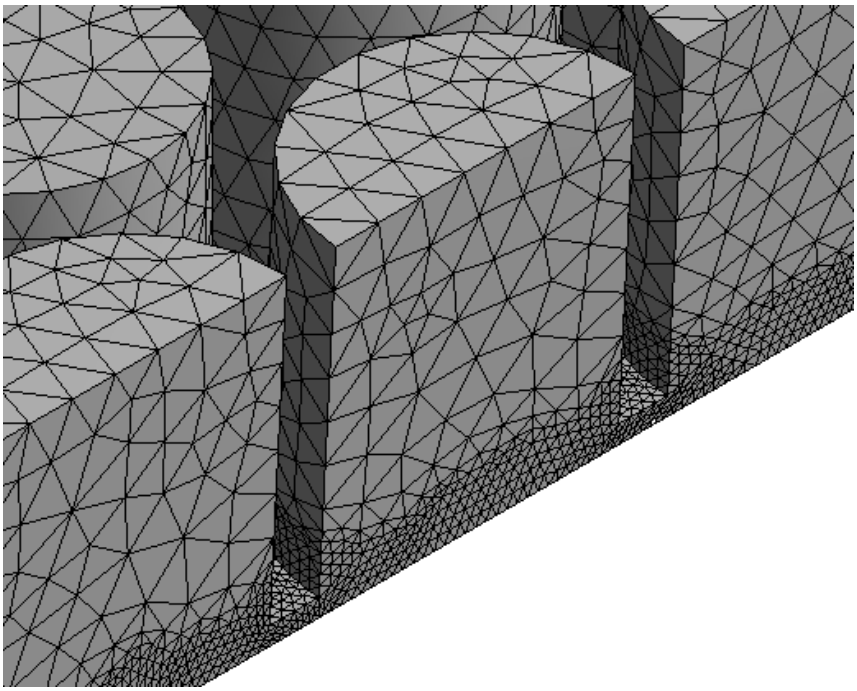

(b)

Figure 3-3 (a) Mesh for baseline model and (b) Detail view

The numerical analysis of the seal models generated for the DOE study is performed in ANSYS CFX package, which was based on Finite Volume Method. The solver is pressure-based and implicit as well. The interpolation, in this case, is second order. The working fluid is air, ideal gas, and a reference pressure of 1 atmosphere. The entire fluid domain was configured in a rotating frame of reference, with 20,200 RPM rotating speed around the axis of the seal and the rotor surface set as counter rotating wall. A sector of the seal is modeled to take advantage of the periodicity, thus periodic rotational symmetry is employed for the left and right boundaries of the sector. This axisymmetric model reduction significantly reduces the computation time for each design point.

Steady-state CFD simulations are performed for all feasible geometries to evaluate the seal performance for each point in the design space. The discretization scheme in this study was the high-resolution advection model. The scalar diffusion scheme is positive definite coefficients (interior) and positive definite values (boundary). Conservation equations for mass and momentum are used within an element.

As literature shows, most of the rotor dynamics codes for prediction of seal performance use the constant temperature assumption. In addition, at least one of the experimental study shows that the temperature difference between seal inlet and outlet is negligible (max 3~4 ℃), thus isothermal conditions are set for all simulation and energy equation is not solved for.

The operating conditions and boundary conditions imposed for the numerical simulation are specified based on the experimental setup. The angular velocity of the rotor is 20,200 rpm, the inlet and outlet pressures are 7 MPa and 3.15 MPa, respectively. The detail of the fluid domain setup is listed in Table 3-3. The Ansys built-in k-ε turbulence model was utilized due to the complex geometry associated with the winding flow path and the relatively unknown turbulent behavior of the fluid in the experimental case [61]. Despite its known limitations, such as the reduced accuracy for separated flows or streamline curvature, this turbulence model has been selected as it provided increased computational robustness and reduced the overall computational time. Each simulation is considered to

be converged when the momentum and continuity RMS convergence target was below 10^{-5}. The CFD results are further post-processed to calculate the leakage rate and to extract the main flow variables to facilitate calculation of dynamic coefficients using an in-house hybrid CFD-bulk flow code [63]. This Matlab code includes solving for the friction factors from CFD results using Hirs' shear stress equations. Then the fluid forces acting on the rotor are computed using the bulk-flow perturbation equations. Then the rotordynamic coefficients are obtained based on the rotordynamic equations of motion.

Table 3-3: Operating Conditions and Boundary Conditions – Elliptical Hole-Pattern Seals

Parameter	Value
Rotor Speed	20200 [rpm]
Inflow Pressure	7 [MPa]
Exit Pressure	3.15[MPa]
Fluid Material	Ideal air
Heat Transfer	Isothermal
Turbulence Model	k-ε
Analysis Type	Steady state

3.1.3 Results and Discussion

In this case study, we selected a relevant seal geometry for which experimental data were available. This facilitated fine-tuning of the CFD setup, including selection of the turbulence model, to match the experimental data, and allowed the validation of the CFD model. Once confidence in the CFD model predictions was gained, only small adjustments to populate the design space were made to the geometrical parameters related to the surface patterning, while the numerical modeling setup was kept identical.

The CFD simulation for the baseline seal model showed a value for the leakage rate of approx. 0.407 kg/s, while the leakage rate measured, as reported in [64], was 0.409 kg/s. The deviation between the CFD result and experimental data was only 0.5%, which validates the baseline CFD model.

A total of 68 CFD simulations were performed from the 5-factor central composite design. The flow pattern for the baseline seal model is shown in Figure 3-4, where one can see the recirculation flow in the cavity and the accelerating flow in the narrow clearance between the rotor and the seal surface. The interaction between these two flow patterns assists in dissipating the fluid kinetic energy and thus reduces the leakage rate. The more intense this interaction is the more efficient the sealing effect could be.

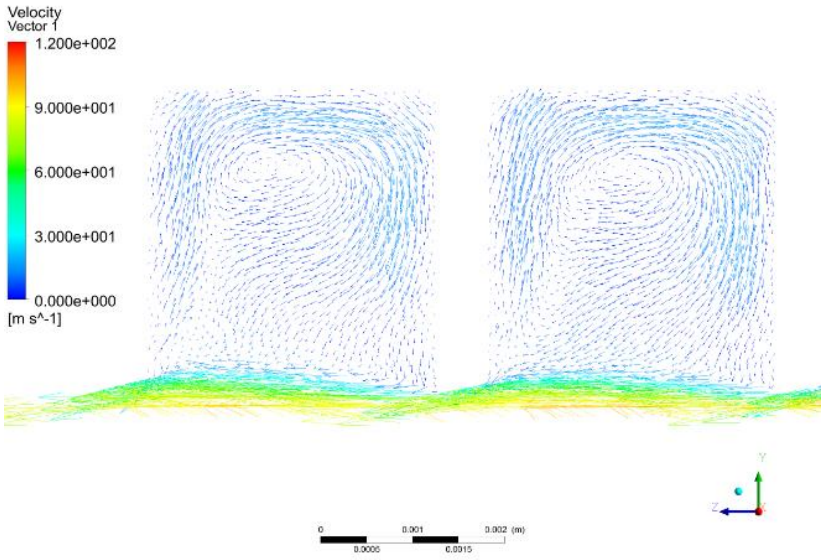

(a)

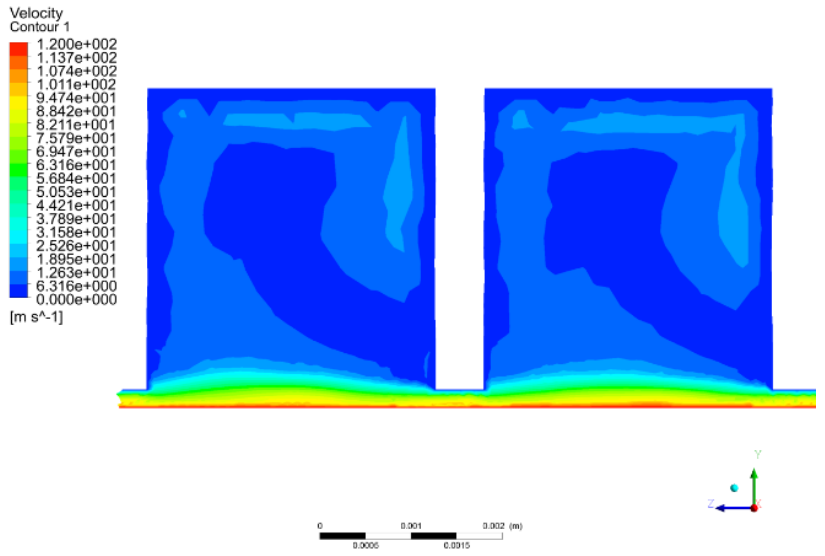

(b)

Figure 3-4 Velocity plot for baseline model (a) Vector plot (b) Contour plot

A sensitivity study for the leakage and rotordynamic coefficients function of the five design variables selected was performed for the design space defined in the previous section. The entire DOE process, including the CFD simulations and the result analysis, was performed using ANSYS and Design Expert software. Quadratic polynomial fitting was then used to determine the sensitivity of different design variables with respect to different outputs.

In this study, five reduced quadratic regression models were generated for the 5 response variables (leakage, direct and cross-coupled stiffness, direct damping and effective damping). These regression models are used to create surface response maps of the parameter's effects on the responses. The reduced regression models are obtained from the full quadratic least squares regression model by backward elimination process. To demonstrate the effectiveness of reduced regression models, preliminary-regression models obtained based on only 40 data points are compared with the final regression models based on all 68 data points using the exact same terms. The coefficients of preliminary regression model terms and final model terms are very close, and the comparison between the prediction using preliminary regression model and the actual 28 data points (the rest data points of the full 68 data which are not used in the preliminary regression models) only shows a maximum of less than 8% difference. As a result, the following final reduced regression models shown are used to generate the response surfaces.

The leakage rates corresponding to all 68 design points range from 0.371 kg/s to 0.476 kg/s. For the baseline model, the leakage is 0.407 kg/s, and the optimal case shows an 8.04% improvement from the baseline model. The reduced regression model as shown in Eqn. 3-8 has 12 coefficients, and the R-squared value is 0.821.

$$\begin{aligned} M_L = {} & 0.318 + 0.133a + 0.364r_{ab} + 2.16 \times 10^{-5}\theta + 9.26 \times 10^{-3}n_c \\ & - 8.74 \times 10^{-3}n_a - 0.103ar_{ab} - 1.98 \times 10^{-3}an_c \\ & - 5{,}86 \times 10^{-3}r_{ab}n_c - 0.0135a^2 - 2.93 \times 10^{-6}\theta^2 \\ & + 1.12 \times 10^{-4}n_a^2 \end{aligned} \qquad \textbf{Eqn. 3-8}$$

The response surfaces for leakage rate are shown in Figure 3-5. Based on the regression model, one can see that leakage response is mainly controlled by the size of the elliptic holes and the number of holes. The number of holes in the circumferential direction affects the leakage response much more compared to the number of holes along the axial direction. The size and number of the holes altogether determine the total area of the elliptical holes. Therefore, this information indicates that the total area of elliptical holes is the most important factor with respect to the leakage rate. A similar observation is reported in [58]. One can also observe that tilt angle θ has little effect on the leakage.

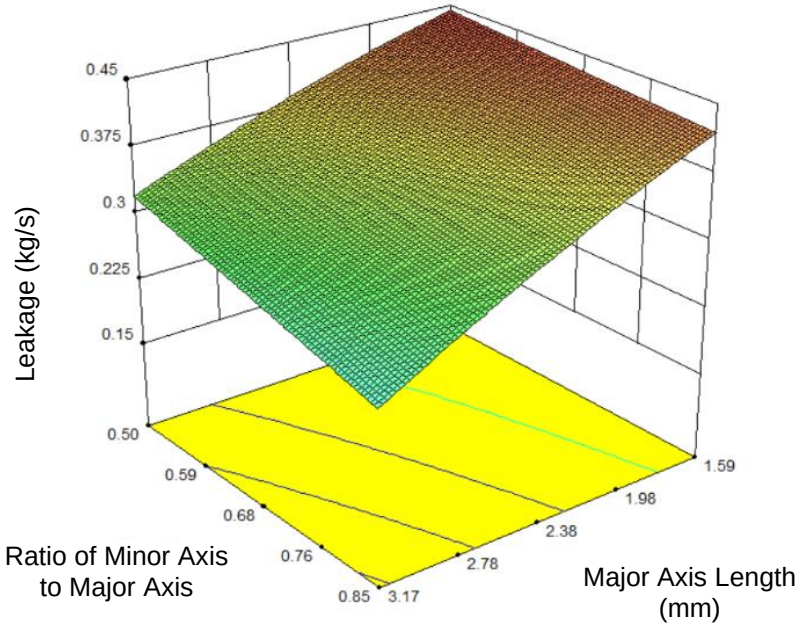

(a)

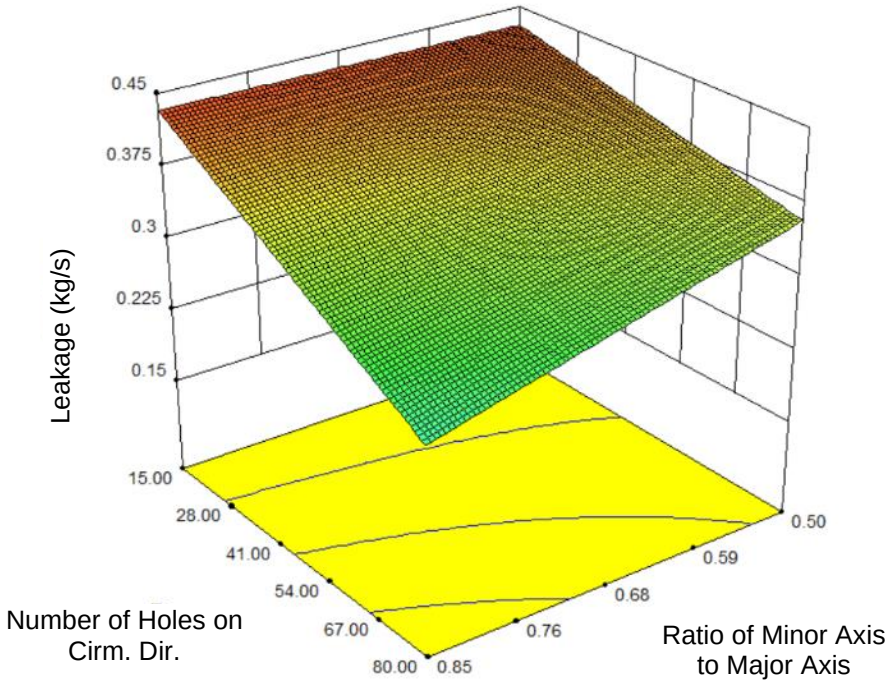

(b)

Figure 3-5 Leakage rate (kg/s) versus two design variables; (a) r_{ab} and a and (b) n_c and r_{ab}

The direct stiffness coefficient of all 68 design points ranges from 35,500 kN/m to 45,200 kN/m. For the baseline model, the direct stiffness was 29,400 kN/m (baseline model was not included in the regression model). The reduced regression model as shown in Eqn. 3-9, which has 13 coefficients, and the R-squared value is 0.986.

$$\begin{aligned} K_{XX} = {} & 5.25 \times 10^7 + 9.68 \times 10^{6a} + 6.88 \times 10^6 r_{ab} + 2.15 \times 10^5 n_c \\ & + 1.36 \times 10^6 n_a - 9.65 \times 10^6 a r_{ab} - 2.12 \times 10^5 a n_c \\ & - 5.91 \times 10^5 a n_a - 3.17 \times 10_5 r_{ab} n_c - 8.64 \times 10^5 r_{ab} n_a \\ & - 1.22 \times 10_4 n_c n_a + 1.28 \times 10^7 r_{ab}^2 + 2.\mathbf{71} \times 10^3 n_c^2 \end{aligned} \qquad \textbf{Eqn. 3-9}$$

The response surfaces for the direct stiffness are presented in Figure 3-6. The regression model shows that the direct stiffness is influenced by the major axis radius a and the number of holes in both the axial and circumferential directions. The tilt angle θ has very little effect on the direct stiffness since it is not contained in the regression model. The direct stiffness is reduced when there are smaller and fewer holes generating the pattern.

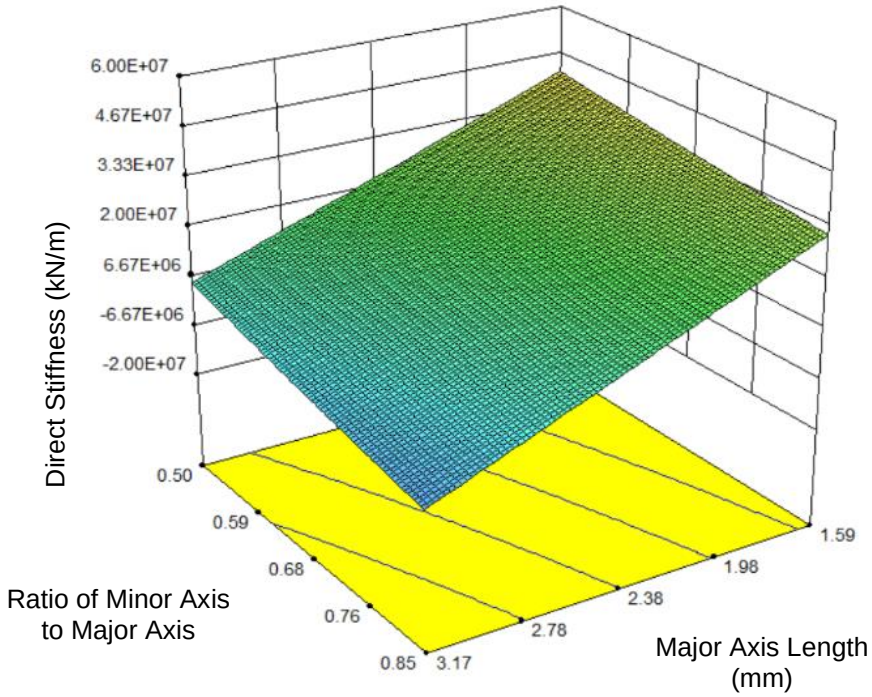

(a)

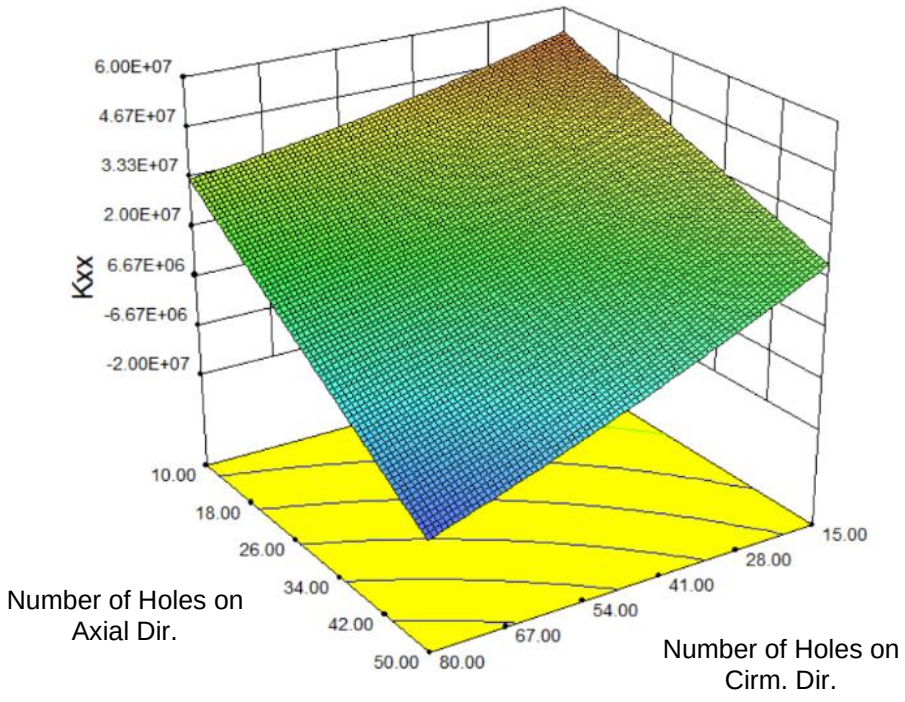

(b)

Figure 3-6 Response surfaces for the direct stiffness (N/m) versus design variables; (a) r_{ab} and a and (b) n_a and n_c

The cross-coupled stiffness for all 68 design points ranges from 5,260 kN/m to 22,000 kN/m. For the baseline model, the cross-coupled stiffness is 5,240 kN/m (baseline model was not included in the regression model). As shown in Eqn. 3-10, the reduced regression model has 14 coefficients, and the R-squared value is 0.974.

$$\begin{aligned} K_{XY} = {} & 1.90 \times 10^8 - 4.36 \times 10^7 a - 8.25 \times 10^7 r_{ab} + 8.51 \times 10^4 \theta \\ & - 1.25 \times 10^6 n_c - 2.29 \times 10^6 n_a - 4.95 \times 10^3 a\theta \\ & - 6.77 \times 10^4 r_{ab}\theta - 8.09 \times 10^2 \theta n_a + 7u.97 \times 10^3 n_c n_a \\ & + 4.97 \times 10^6 a^2 + 3.63 \times 10^7 r_{ab}^2 + 6.05 \times 10^3 n_c^2 \\ & + 1.99 \times 10^4 n_a^2 \end{aligned} \quad \textbf{Eqn. 3-10}$$

Figure 3-7 illustrates the response surfaces from the regression model of the cross-coupled stiffness coefficients. It can be seen that the number of holes along both the axial and circumferential directions have more influence on the cross-coupled stiffness than any other design variable. The tilt angle, which was initially believed to contribute more to the cross-coupled stiffness by making an analogy with the effect of swirl-brakes typically utilized to remove the fluid pre-swirl from the inlet of the seals, was not as important as initially expected. As this DOE study indicates, the patterning or the way the holes are distributed on the surface of the seal is much more important than the actual shape of the hole. The response surface for θ vs. r_{ab} is relatively flat as can be seen in Figure 3-7(b), which indicates that the effects of these two design variables are insignificant. Similar to the direct stiffness coefficient, the value of the cross-coupled stiffness coefficient is reduced when there are smaller and fewer holes on the seal surface.

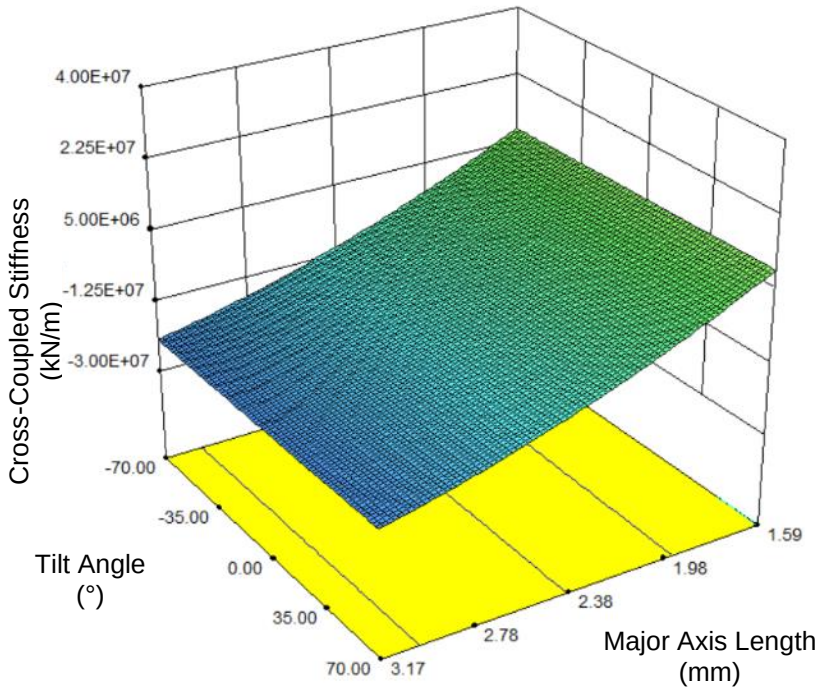
4.00E+07
2.25E+07
5.00E+06
-1.25E+07
-3.00E+07
Cross-Coupled Stiffness
(kN/m)
-70.00
-35.00
0.00
35.00
70.00
Tilt Angle
(°)
3.17
2.78
2.38
1.98
1.59
Major Axis Length
(mm)

(a)

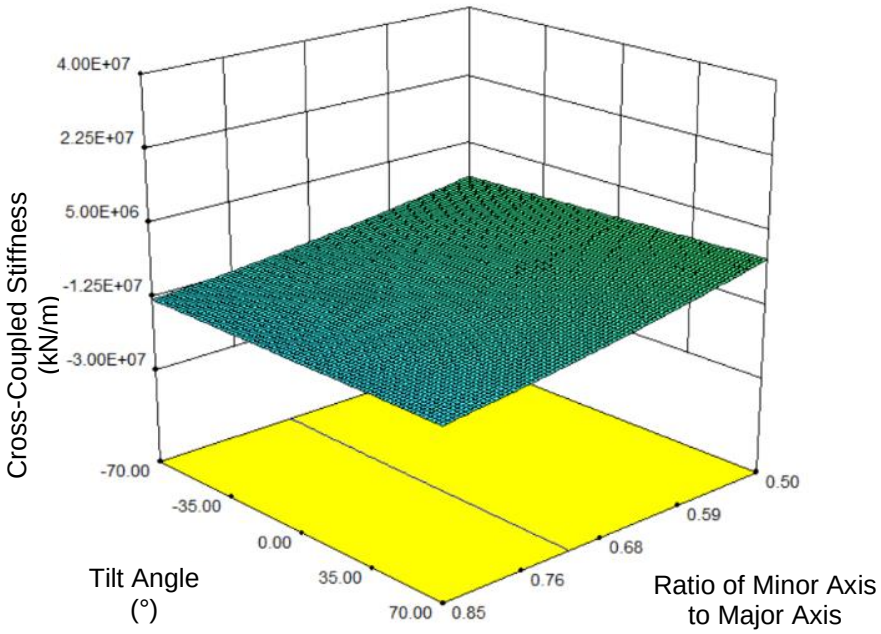
4.00E+07
2.25E+07
5.00E+06
-1.25E+07
-3.00E+07
Cross-Coupled Stiffness
(kN/m)
-70.00
-35.00
0.00
35.00
70.00
Tilt Angle
(°)
0.85
0.76
0.68
0.59
0.50
Ratio of Minor Axis
to Major Axis

(b)

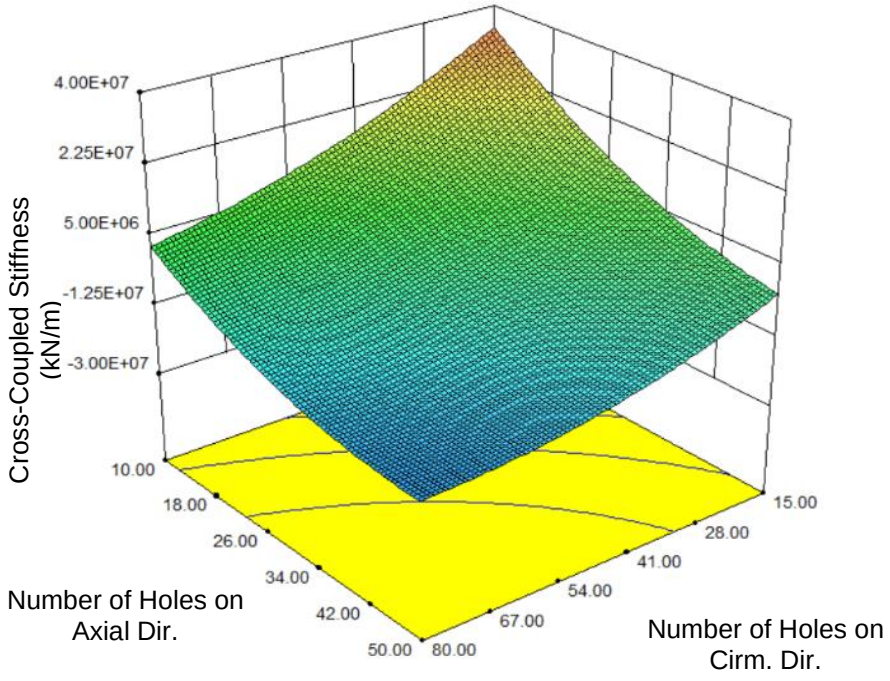

(b)

Figure 3-7 Response Surfaces of Cross-coupled Stiffness (N/m) versus design variables: (a) θ and a , (b) θ and r_{ab} , (c)n_a and n_c

The direct damping of all 68 design points range from 4,880 kNs/m to 14,700 kNs/m. For the baseline model, the direct damping is 4,060 kNs/m (baseline model was not included in the regression model). The reduced regression model shown in Eqn. 3-11 has 13 coefficients, and the R-squared value is 0.981.

$$\begin{aligned} C_{XX} = {} & 1.37 \times 10^5 - 2.99 \times 10^4 a - 7.45 \times 10^4 r_{ab} - 862 n_c \\ & - 1.74 \times 10^3 n_a + 4.12 \times 10^3 a r_{ab} + 149 r_{ab} n_c \\ & + 286 r_{ab} n_a + 3.65 n_c n_a + 3.05 \times 10^3 a^2 \\ & + 2.38 \times 10^4 r_{ab}^2 + 3.96 n_c^2 + 14.6 n_a^2 \end{aligned} \qquad \textbf{Eqn. 3-11}$$

Figure 3-8 shows the response surfaces for the direct damping. Similarly to direct stiffness response, the tilt angle θ again is not contained in the regression model. This means that θ is not possibly related to or influencing the direct damping. In this case, the number of holes in axial and circumferential directions is more important compared to any other design variable.

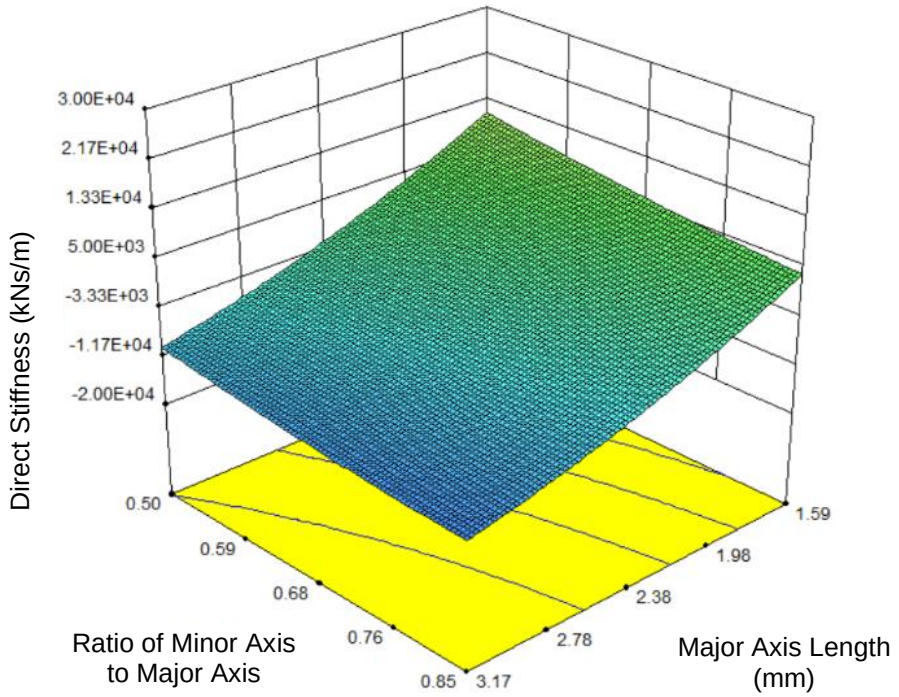

(a)

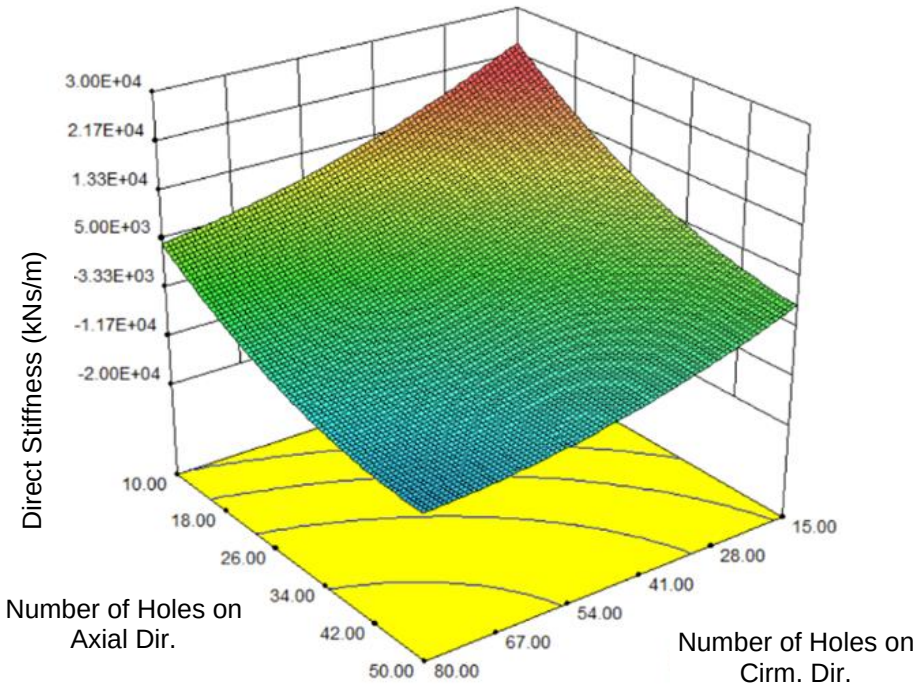

(b)

Figure 3-8 Response Surfaces of Direct Damping (Ns/m) versus design variables: (a) r_{ab} and a , (b) n_a and n_c

The effective damping for all 68 design points ranges from 1,720 kNs/m to 5,760 kNs/m. For the baseline model, the effective damping was 1,590 kNs/m. The reduced regression model, which is shown in Eqn. 3-12, has 17 coefficients, and the R-squared value is 0.940.

$$C_{eff} = 3.03 \times 10^4 - 6.41 \times 10^3 a - 6.13 \times 10^3 r_{ab} - 33.0\theta - 175 n_c - 482 n_a + 1.90 a\theta + 24.3 r_{ab}\theta + 2.214 \theta n_c + 677 a^2 + 6.53 \times 10^{-2}\theta^2 + 1.17 n_c^2 + 5.10 n_a^2 \quad \textbf{Eqn. 3-12}$$

The response surfaces for the effective damping are illustrated in Figure 3-9. Based on the regression model and the response surfaces, one can see that the tilt angle θ and the ratio of major axis radius to minor axis radius, which represents the effect of the elliptical groove shape, are much less important to the effective damping compared to the other three design variables. The response surface for θ vs. r_{ab} is nearly flat, while the response surface for n_a vs. n_c has an noticeable slope.

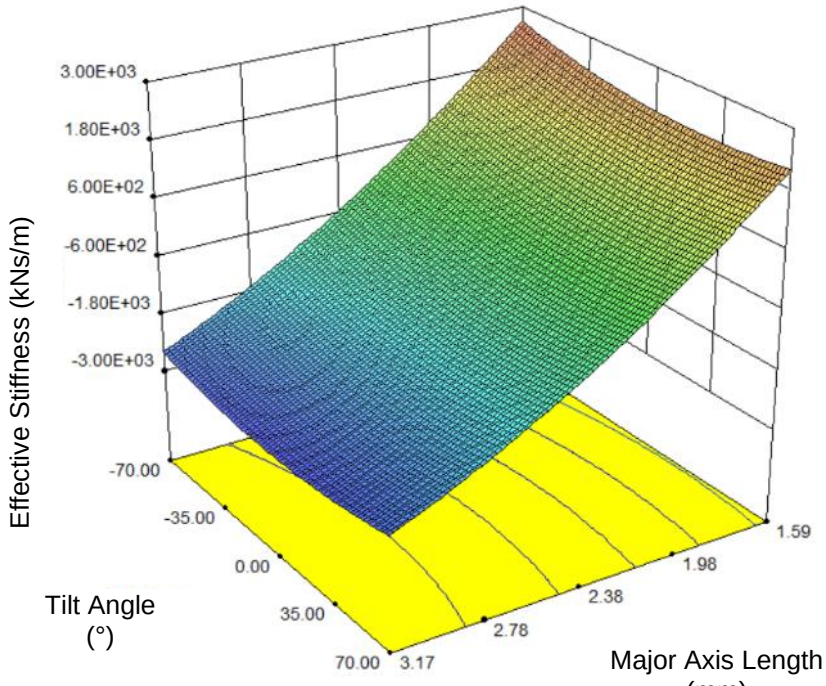

(a)

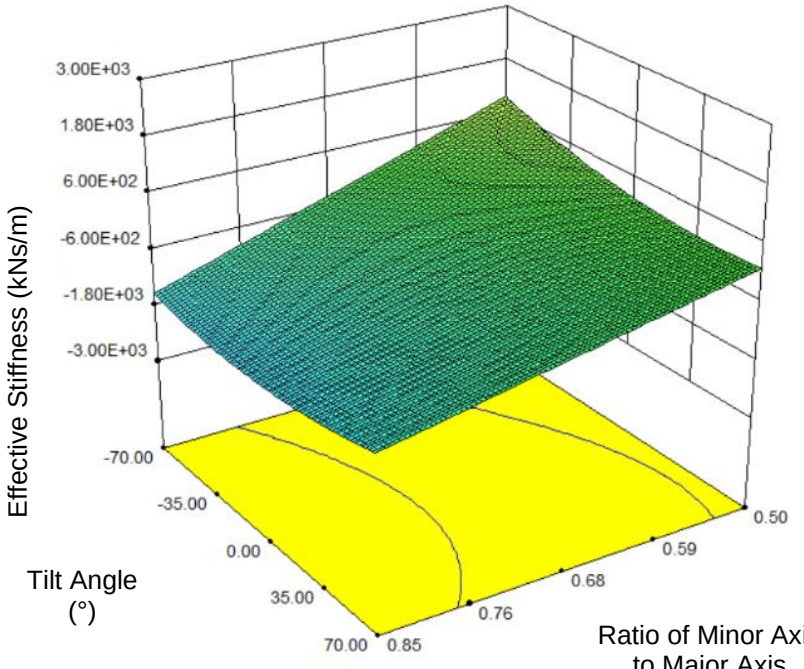

(b)

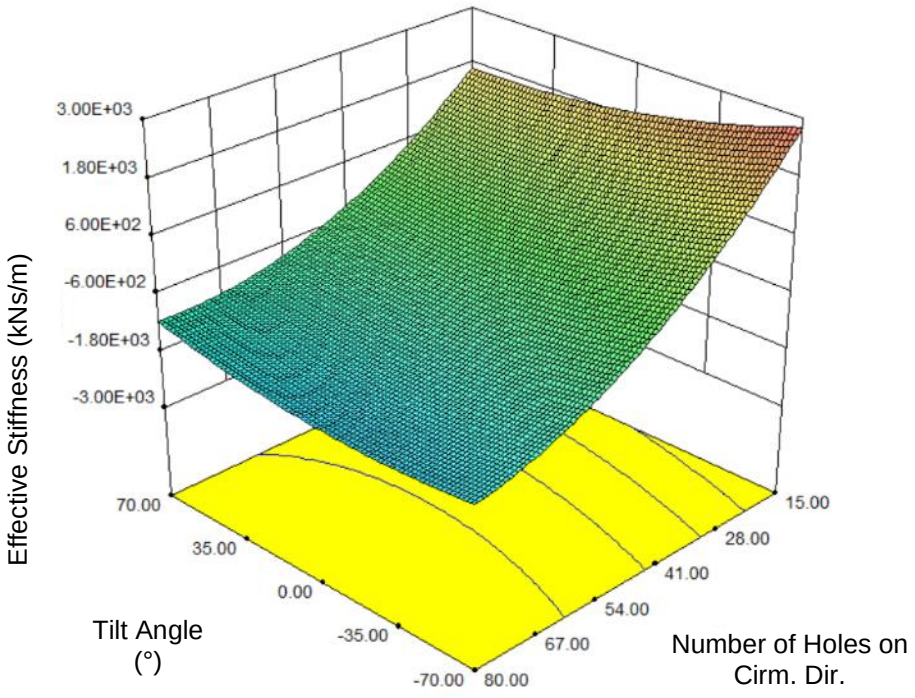

(c)

Figure 3-9 Response Surfaces of Effective Damping versus (a) θ and a, (b) θ and r_{ab} , (c) n_c and θ

The validation of the regression models for all 5 responses can be seen in Figure 3-10. From these figures, one can observe that the regression models for the rotordynamic coefficients are more accurate compared to the regression model for the leakage rate. The values from the design points scatter in a much larger area in the figure showing predicted vs. actual value, which is also relatively far from the regression model. On the other hand, the predicted values are located much closer to the regression model for all four rotordynamic coefficients responses.

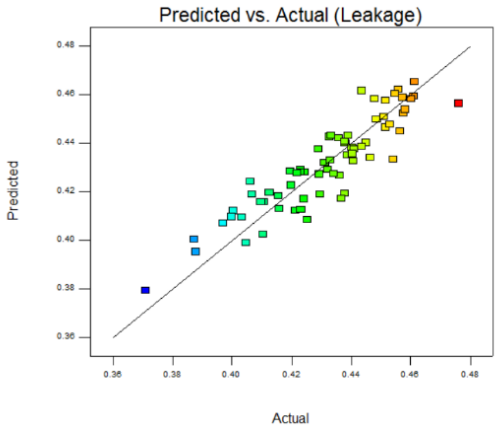

(a)

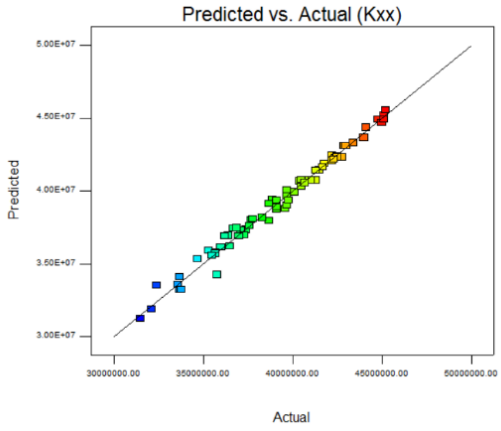

(b)

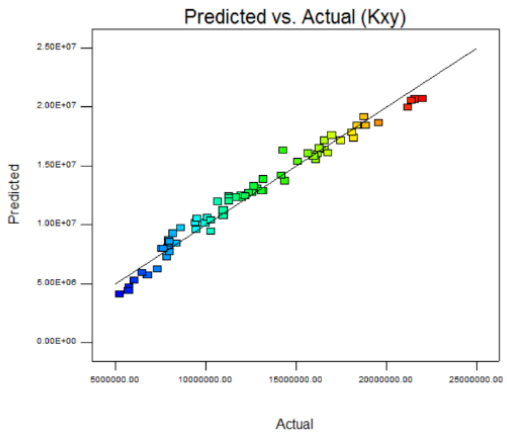

(c)

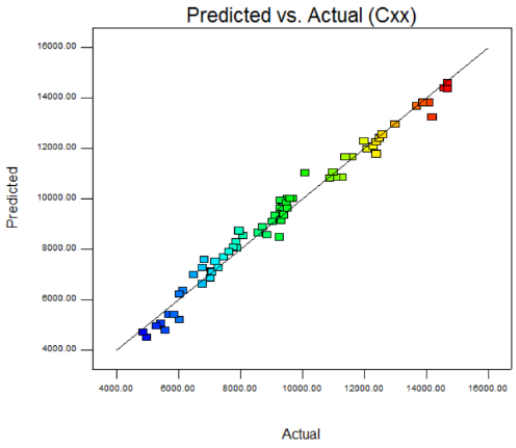

(d)

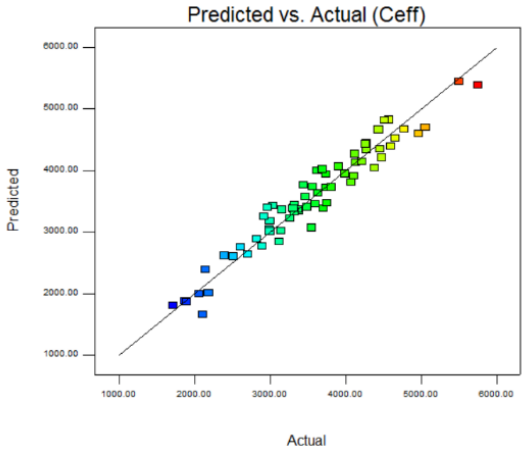

(e)

Figure 3-10 Comparison of predicted regression model with actual values from all design points for (a) Leakage rate, (b) Direct Stiffness, (c) Cross Coupled Stiffness, (d) Direct Damping, and (e) Effective Damping Coefficient

Some examples of high performance and low performance seal design, from the leakage rate perspective, are given in Figure 3-11 and Figure 3-12. Figure 3-11 illustrates a high performance example of a surface pattern leading to a minimal value of the leakage rate, while Figure 3-12 shows the opposite, a patterning that is fairly inefficient at dissipating the fluid kinetic energy to reduce the leakage. The details of the geometries, as well as the pressure distributions, can be observed from the contour plots. In addition, the difference between the two geometries for both velocity and pressure is shown in Figure 3-13 and Figure 3-14. One can observe a greater pressure difference near the inlet, while the velocity difference is obvious in the clearance region between rotor surface and stator surface. Figure 3-13(a) and Figure 3-14(a) show the side by side comparison, and Figure 3-13(b) and Figure 3-14(b) show the subtractive differences. Please note that the non-overlapping part of the two geometries selected for comparison are shown as white gaps or missing regions in the figure. Comparing side by side the two seal geometries shown in Figure 3-13(a), one can observe that the high performance one has much larger total hole area, while the low performance one has a relatively smaller total hole area. The vortices formed inside the holes can be observed from the vector plots. It can be seen that there is only one

vortex inside the cavity for the low performance geometry. For the high performance geometry, there is one vortex at the bottom of the cavity and another one forms near the rotor surface. This interaction between the vortex and the jet flow in the clearance region, as well as the interaction between the two vortices in the cavity, has the ability to enhance the kinetic energy dissipation with a significant positive effect on the leakage rate. Note that the vortices inside the hole are influenced by both the shape and the orientation of the holes in the pattern.

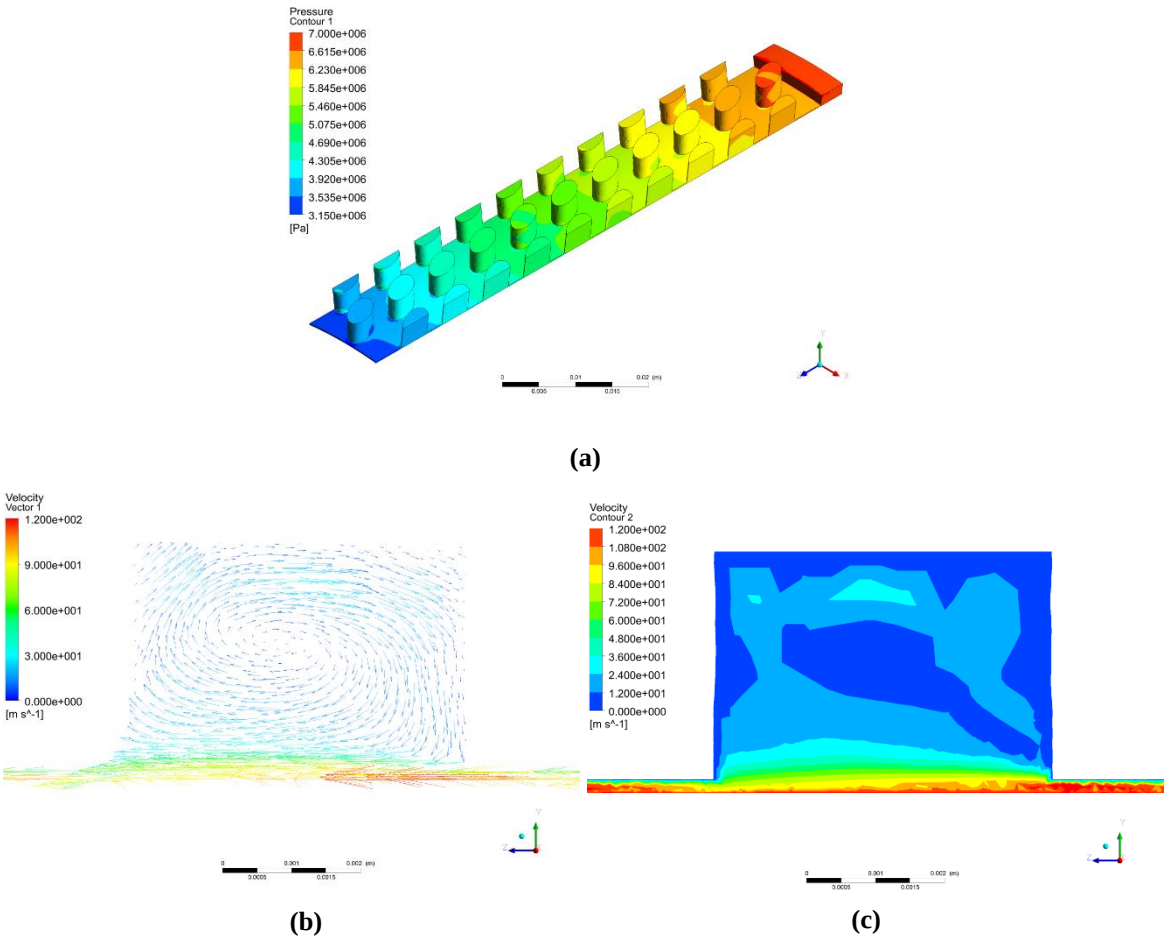

Figure 3-11 Seal geometry with high performance leakage rate characteristics: (a) Pressure contour, (b) Velocity plot, (c) Velocity contour

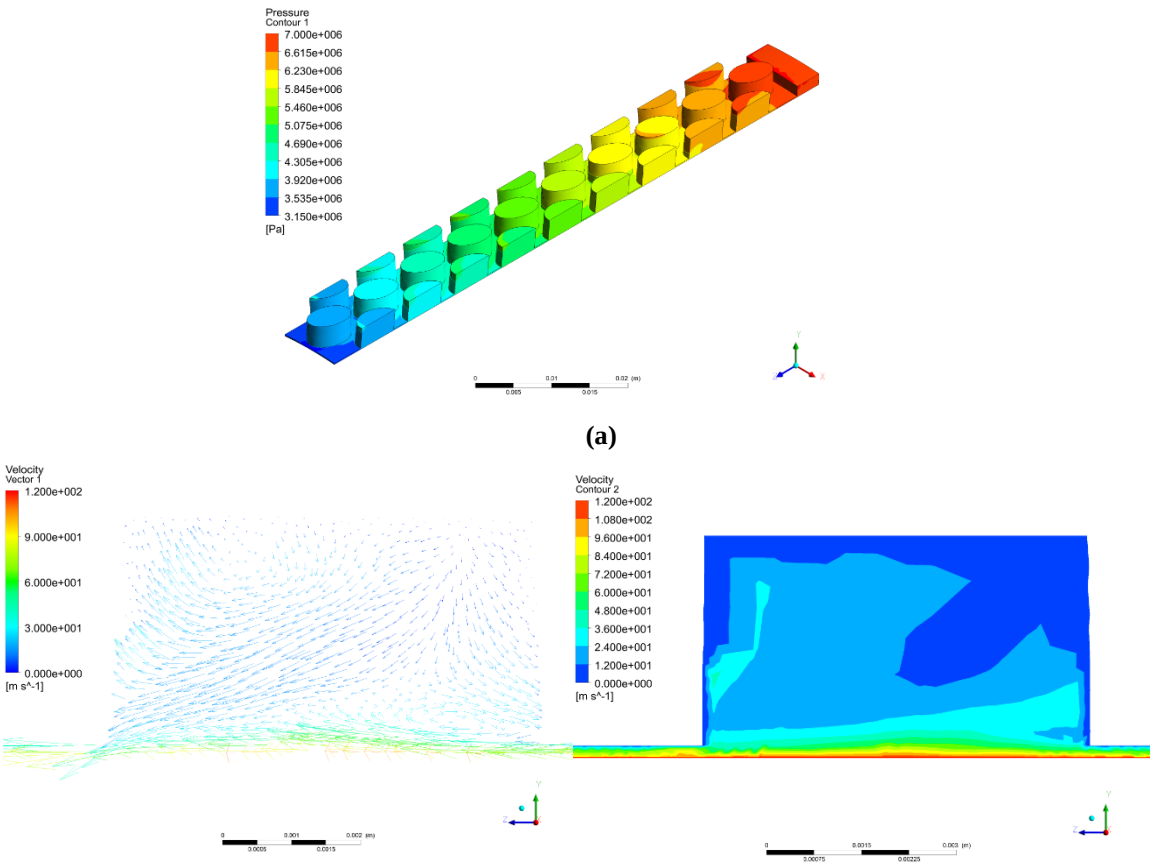

Figure 3-12. Seal geometry with a low performance leakage rate characteristics: (a) Pressure contour, (b) Velocity plot, (c) Velocity contour

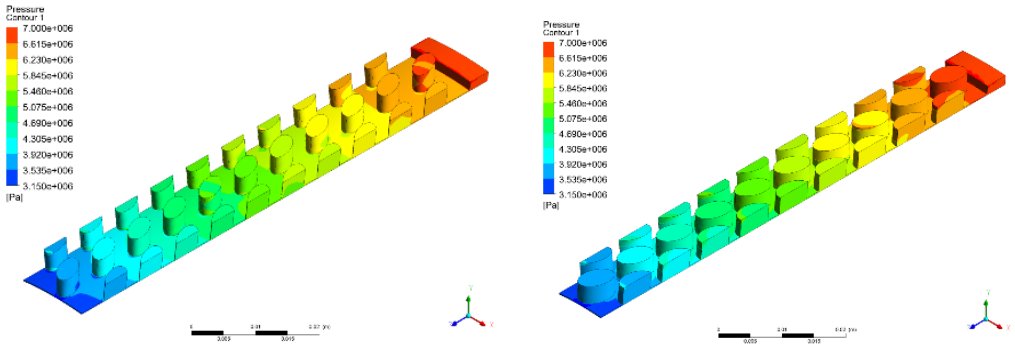

(a)

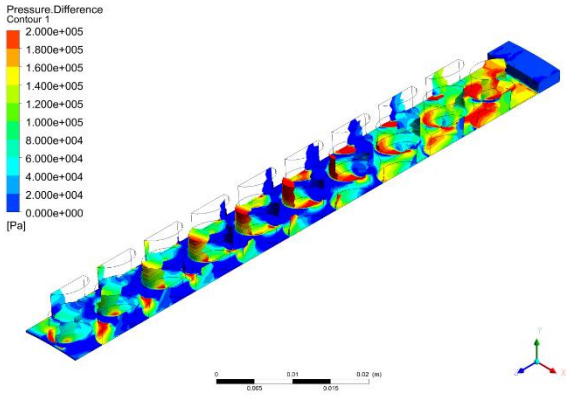

(b)

Figure 3-13. Pressure contours-Comparison between the high and low performance leakage rate seal models: (a) Side by side comparison (b) Difference plot for pressure for the two seal models

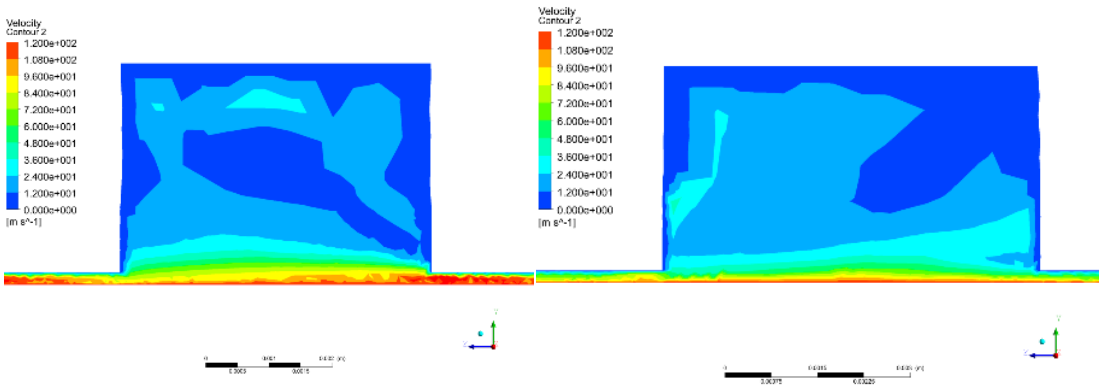

(a)

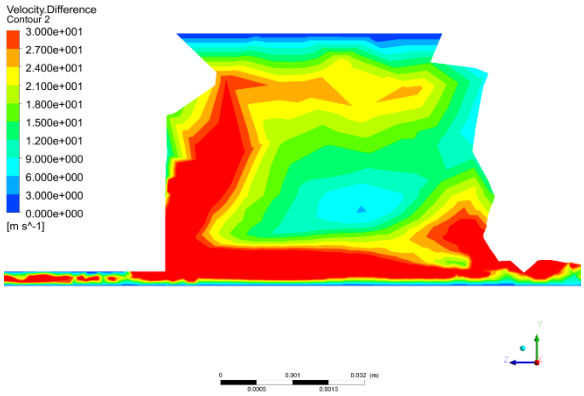

(b)

Figure 3-14. Velocity contours-Comparison between the high and low performance leakage rate seal models: (a) Side by side comparison (b) Difference plot (no overlap region is shown in white)

Figure 3-15, Figure 3-16, Figure 3-17 and Figure 3-18 illustrate a similar comparison of a high performance geometry and low performance seal geometry from the perspective of the effective damping coefficient. From the pressure contour figure, the low performance geometry example of effective damping has a greater number of holes along the axial direction. In addition, the sizes of the holes are also smaller for the low performance geometry. For the high performance geometry example, the orientation of the hole is negative, and the space between holes is also larger. From the vector plot in Figure 3-16, one can see a large vortex anchored in the half-part closer to the bottom of the cavity. For the low performance geometry example exhibiting a lower effective damping coefficient, one can see that a vortex forms in the half part of the cavity closer to the rotor. There is also a large stagnation region near the bottom of the cavity. In Figure 3-17, one can observe

that the difference in pressure between the high and low effective damping coefficient seal models is relatively small relative to the leakage rate comparison in Figure 3-13and Figure 3-14. Similar trends can be observed in Figure 3-18 for the difference in velocity. Note that the red color area near the clearance region in Figure 3-18, indicating a higher pressure difference, results from the geometry difference (on one geometry it is the groove, on the other geometry it is the stator surface). On the other hand, in the area where the two design points have the same geometry (such as the clearance region for both geometries), the difference is much smaller. Stability characteristics of the two seals are compared through the effective damping coefficient, a lower value indicating that the seal performs worse from a rotordynamic standpoint.

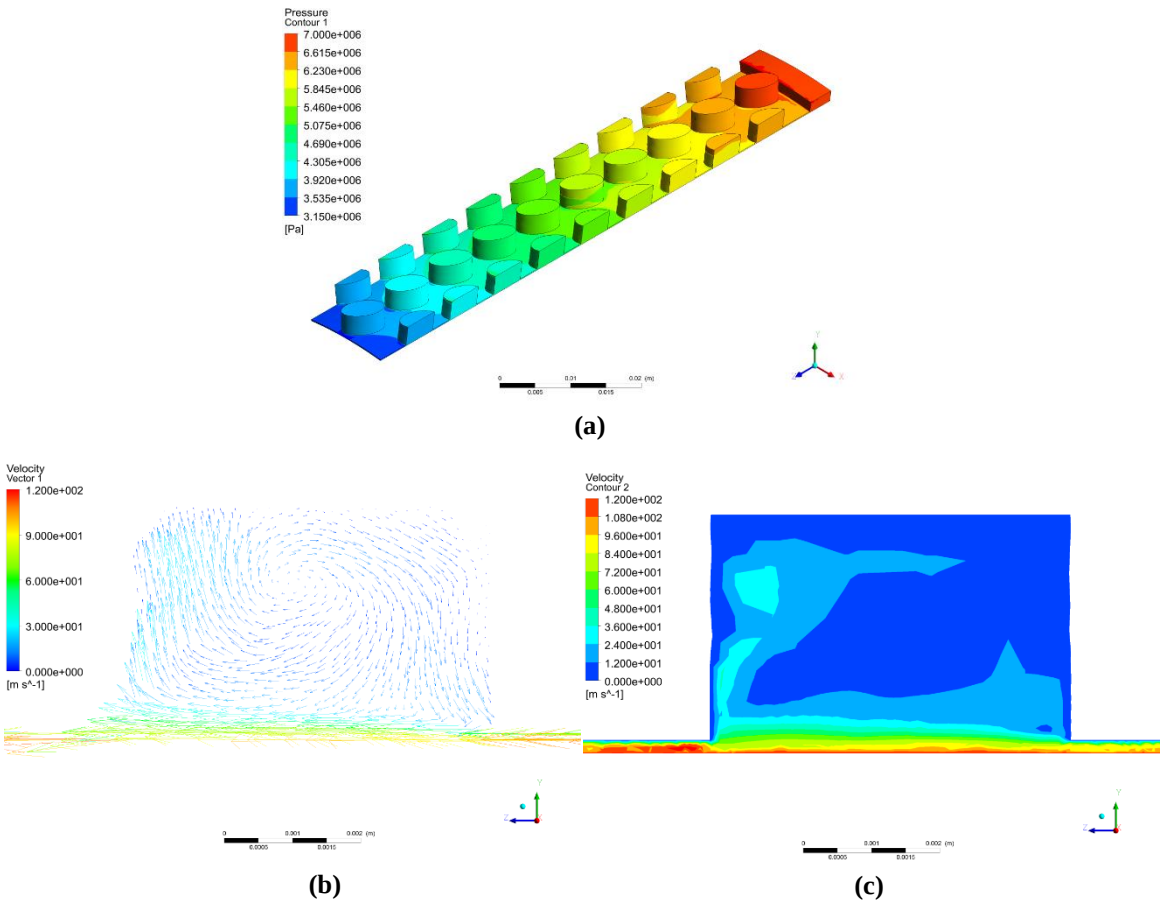

Figure 3-15. High performance seal geometry - corresponding to a higher effective damping coefficient compared to baseline design which indicates a better stability potential: (a) Pressure contour, (b) Velocity plot, (c) Velocity contour

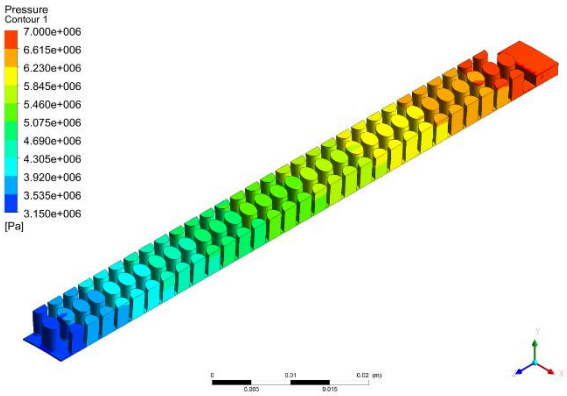

(a)

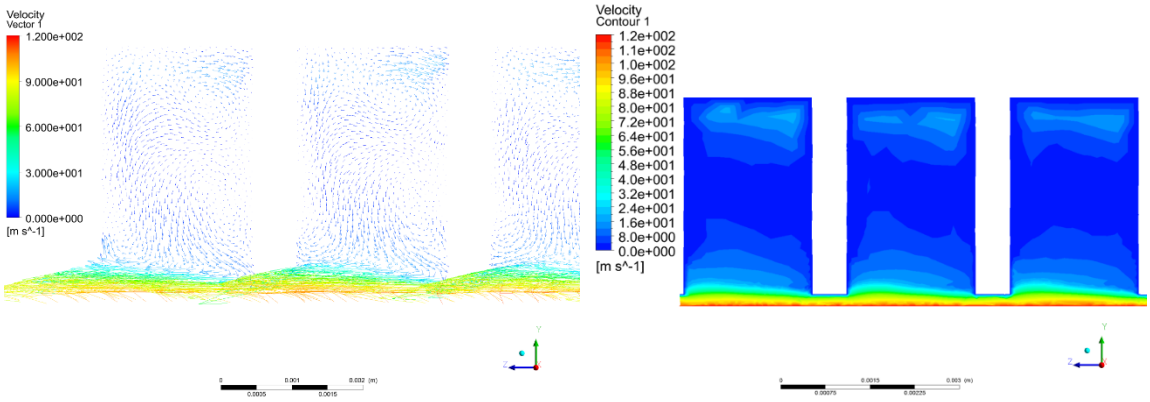

(b) **(c)**

Figure 3-16. Low performance seal geometry - corresponding to a lower effective damping coefficient compared to baseline design, which indicates a poorer stability potential: (a) Pressure contour, (b) Velocity plot, (c) Velocity contour

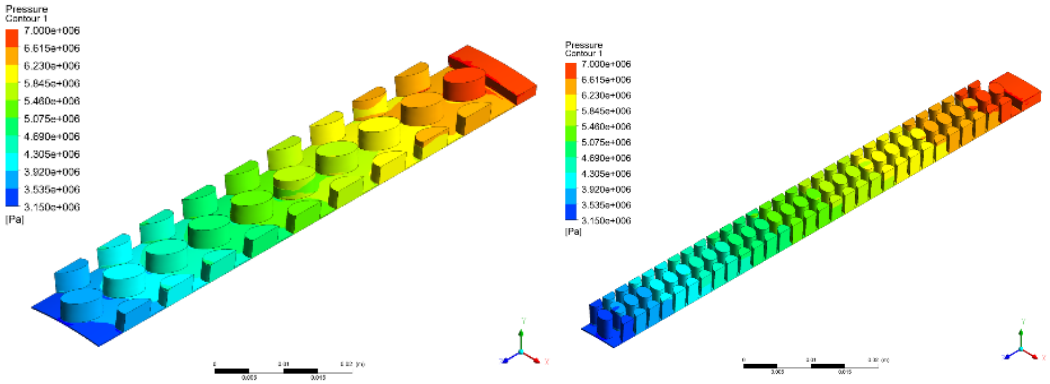

(a)

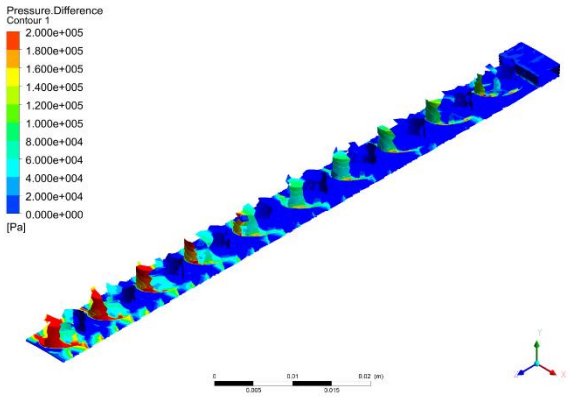

(b)

Figure 3-17. Pressure contours-Comparison between the high and low performance seal geometry for effective damping coefficient: (a) Side by side comparison, (b) Difference plot

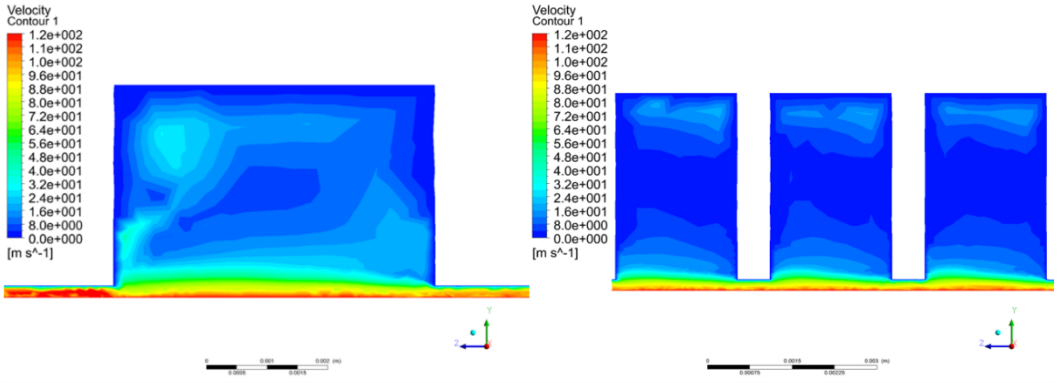

(a)

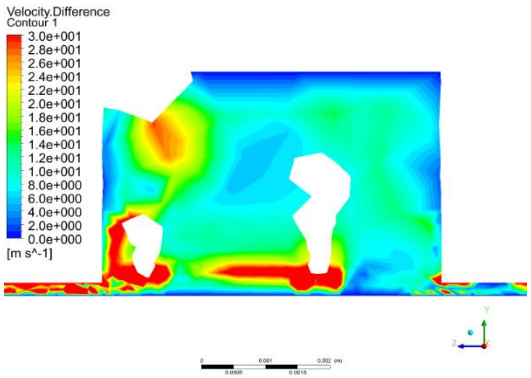

(b)

Figure 3-18. Velocity contour-Comparison between the high and low performance seal geometry for effective damping coefficient: (a) Side by side comparison, and (b) Difference plot

In this case study, the effects of elliptical groves on the leakage and dynamic response performance of an industry-relevant hole-pattern seal design were investigated using a combination of CFD, hybrid bulk flow/CFD analysis, and design of experiments techniques. A CFD model of the baseline hole-pattern seal was developed and validated against the experimental data. A DOE study was then performed to investigate the effect that various elliptical shape cavities has on the leakage rate across the seal and the rotordynamic characteristics. CFD simulations were run for multiple patterning configurations to evaluate performance and dynamic characteristics at each point in the design space.

The elliptical grooves patterning was found to influence the leakage rate, which is sensitive to the total area occupied by the holes since the ratio of major axis radius to minor axis

radius alters the resulting area of the holes. The leakage rate was found to decrease as the total area of the holes increased. The tilt angle had no significant influence on the leakage rate since it does not contribute to the total area of the grooves. For the seal model that exhibited best performance in terms of the leakage rate, two vortices are formed in each cavity instead of only one, one is near the bottom of the cavity and another one near the rotor surface. It is believed that this interaction between the vortex and the jet flow in the clearance region, as well as the interaction between the two vortices inside the cavity, has the ability to enhance the kinetic energy dissipation and has a positive effect on reducing the leakage rate.

With respect to the rotordynamic properties, the direct stiffness and direct damping coefficients were found to be strongly related to the number of holes in both the axial and circumferential directions. The cross-coupled stiffness, cross-coupled damping, and the effective damping were also sensitive to the length of the major axis, in addition to the pattern of the grooves. The tilt angle was found to be a relatively minor factor for rotordynamic coefficients corresponding to the parameter ranges selected in this study, in which the length of major axis is only twice as much as the minor axis length. Future work to investigate the impact of elliptical groove patterning on the rotordynamic properties could consider a larger ratio of the major to minor axis length ($a > 4b$).

3.2 Alternately Arranged Surface Patterning of Hole-Pattern Seals

The performance of annular seals depends on the geometry of the leakage path as it facilitates the dissipation of the fluid kinetic energy. The goal of this study is to investigate potential correlations between the characteristics of the alternately arranged surface pattern and the corresponding rotor dynamic properties of the seal in addition to mapping its performance.

Various patterning arrangements lining the stator surface are considered and the relative seal performance change is investigated using a hybrid method that calculates the seal dynamic response for each point in the design space. The design parameters selected in this DOE study are the diameters of alternately arranged holes that are replicated in both axial

and circumferential direction to construct the pattern, the hole depths for both types of holes, and the number of holes in both axial and circumferential directions. A sensitivity study is conducted to analyze the influence of each geometrical parameter on the seal response. Regression models are then generated for each response, including the leakage rate and the rotor dynamic coefficients. Quadratic regression models are used in this study to represent the relationship between the objective functions and the design parameters. The goal is to achieve a minimum leakage rate as well as an improved dynamic response. The results of the baseline model and the best performing design are compared. The results show that the patterning arrangements have crucial effects on the leakage rate as well as the dynamic coefficients of the seal. The results of this study are found to be helpful in designing a hole-pattern seal that can concurrently satisfy constraints on both the leakage rate and the rotor dynamic response while maintaining same design envelope

3.2.1 Computation Model and Parametrization

The original CFD model for this study is inspired by literature [44]. There is a 4 mm upstream region before the main seal region in the baseline model, which allows more accurate pre-swirl conditions to be taken into account. The size of the holes in this study is not uniform, which is different than the baseline model from the literature. The full 3D models for both baseline and one of the DOE design points are shown in Figure 3-19. The constant parameters for the CFD model are shown in Table 3-4.

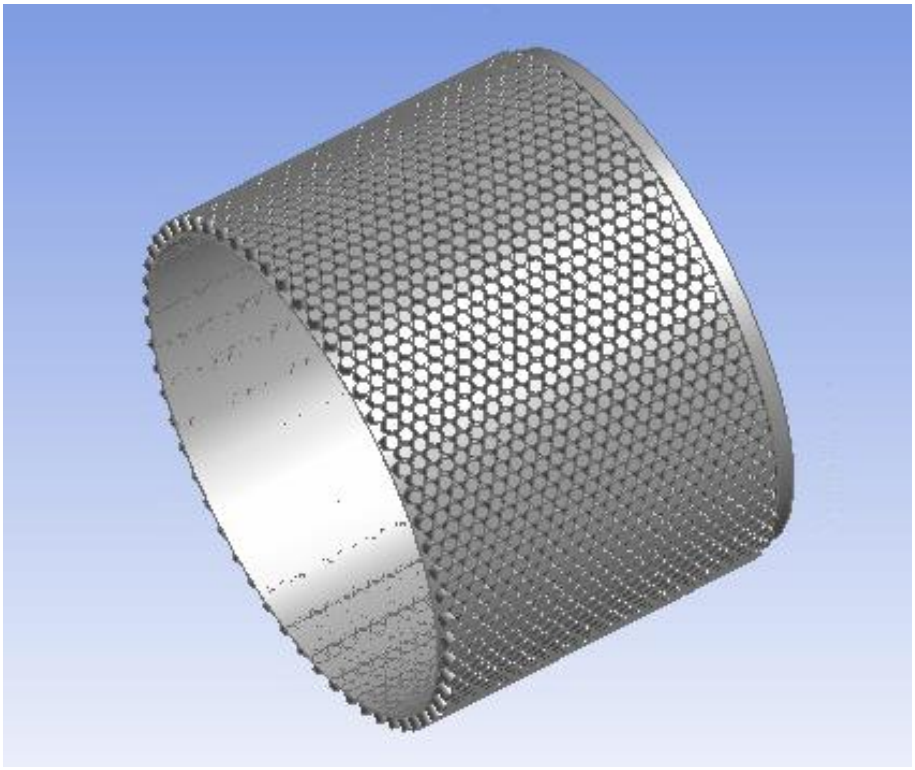

(a)

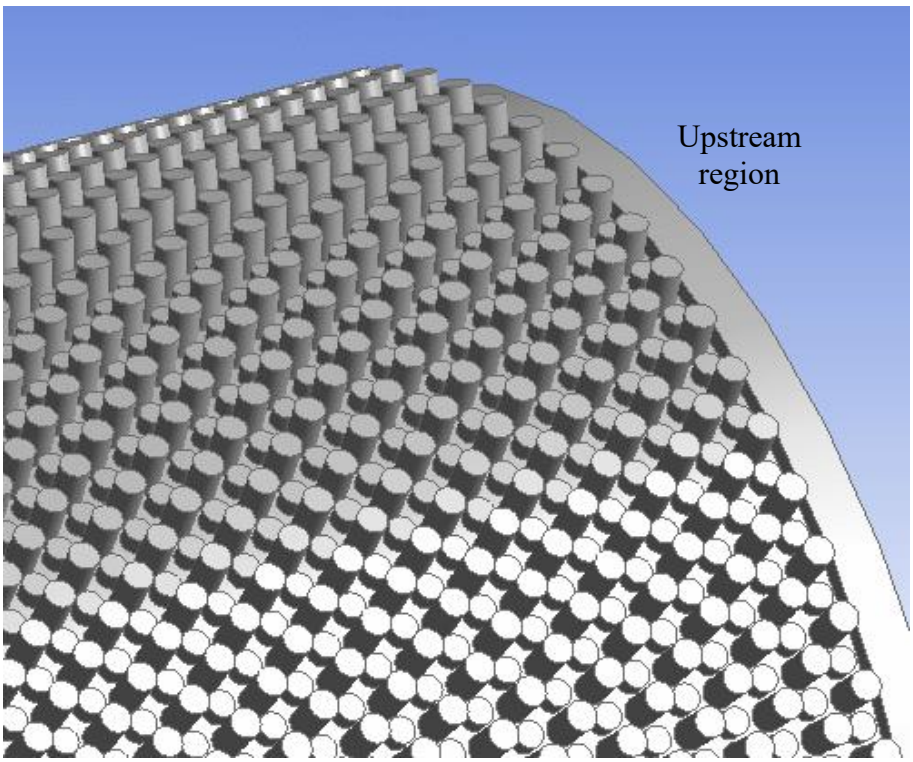

(b)

Figure 3-19. Full 3D Fluid Domain for (a) Baseline Model (b) One of the Design Points

Table 3-4: Constant Parameters – Alternatively Arranged Hole-Pattern Seals

Parameter	Description	Base Value
Dr	Rotor Diameter	114.34 [mm]
Cr	Radial Clearance of Seal	0.20 [mm]
Ls	Seal Length	86 [mm]
Ds	Seal Diameter	114.74 [mm]
δ_1	Space between Inlet and Holes	0.8 [mm]
δ_2	Space between Outlet and Holes	0.45 [mm]

A central composite design with six factors applying the fraction factorial method is used in this study The six design variables vary six important characteristics describing the design space, and include the radius of larger holes R_1, the ratio of smaller hole radius to larger hole radius c ($c = R_2 / R_1$, where R_2 is the radius of smaller holes), the depth of larger holes H_1, the depth of smaller holes H_2, the number of holes in axial direction N_1 and the number of holes in circumferential direction N_2. Constraints are selected to avoid potentially unfeasible designs. For instance, the holes are prevented to overlap with each other. This can be achieved by specifying the distances on both axial direction and circumferential direction between two adjacent holes. The number of holes in both directions can be calculated based on the distances between adjacent holes. As a result, the intermediate design variables used to generate the design space without considering constraints include the radius of the larger holes R_1 (4 levels), the ratio of smaller hole radius to larger hole radius (4 levels), the depth of the larger holes H_1 (4 levels), the depth of the smaller holes H_2 (4 levels), the ratio of space to radius in the axial direction ($r_a = L_a/R_1$, 5 levels), and the ratio of space to radius in the offset direction ($r_c = L_c/R_2$, 5 levels). The design variables are listed in Table 3-5, while variables L_a and L_c are illustrated in Figure 3-20. The range for each design variable is selected based on the base value with an approximate ±50% deviation depending on the specific design variable considered. Note that these ranges are just some reasonable values that work well for the baseline seal model selected, not strict rules that must be followed.

Table 3-5: Design Variables – Alternatively Arranged Hole-Pattern Seals

Design Variables	Intermediate Design Variables	Description	Base Value	Feasible Values
R_1	R_1	Radius of Larger Holes	1.5875 [mm]	1.1906,1.5875, 1.9844,2.3812 [mm]
c	c	Ratio of Smaller Hole Radius to Larger Hole Radius	1	0.9,0.75, 0.6,0.45
$\boldsymbol{H_1}$	H_1	Hole Depth	3.3020 [mm]	1.6510,2.4765, 3.3020,4.1275 [mm]
$\boldsymbol{H_2}$	$\boldsymbol{H_2}$	Hole Depth	3.3020 [mm]	1.6510,2.4765, 3.3020,4.1275 [mm]
$\boldsymbol{N_1}$	$\boldsymbol{r_a}$	Ratio of Space to Radius in Axial Direction	0.277	0.1, 0.2, 0.3, 0.4
$\boldsymbol{N_2}$	$\boldsymbol{r_c}$	Ratio of Space to Radius in Circumferential Direction	0.277	0.1, 0.2, 0.3, 0.4

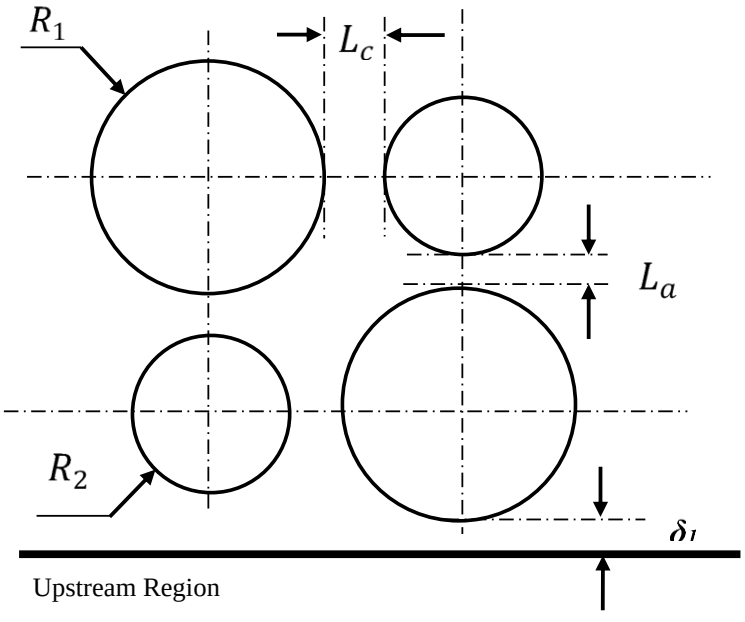

Figure 3-20. Illustration of Geometry Parameters

The six variables used in the parameter sensitivity analysis are still the original six design variables (R_1, c, H_1, H_2, N_1, N_2), and their relationship with the intermediate design variables (R_1, c, H_1, H_2, r_a, r_b) is listed in Eqn. 3-13 to Eqn. 3-16. Note that N_1 and N_2 need to be rounded to the closest integer.

$$L_a = (R_1 + R_2) \cdot r_a \quad \textbf{Eqn. 3-13}$$

$$N_1 = (L_s - R_1 - R_2)/(R_1 + R_2 + L_a) \quad \textbf{Eqn. 3-14}$$

$$L_c = (R_1 + R_2) \cdot r_c \quad \textbf{Eqn. 3-15}$$

$$N_2 = (\pi D - R_1 - R_2)/(R_1 + R_2 + L_c) \quad \textbf{Eqn. 3-16}$$

For the six design variables and the 4 levels for each design variable, the full factorial design includes 46 = 4,096 design points. Performing CFD simulations for all 4,096 design points is nearly impossible since each design point takes hours to finish computing. Therefore, the Kennard-stone algorithm is used on the full design space to identify and select the most representative 25 design points in order to capture the most important features in the novel surface patterning proposed in this study, which shows it is from the result analysis. The Kennard-stone algorithm is sequential and functions by maximizing the Euclidean distances between the newly selected design points and the points already selected. Additional design points are selected by calculating the distance from each not selected design point to each selected compound and maximizing the distance to the closest design point already selected. In this study, the distances for each design variable are normalized before applying Kennard-stone algorithm.

3.2.2 CFD Model and Numerical Analysis

The computational fluid dynamics analysis of the labyrinth seal models is performed in ANSYS CFX v16. Since there is axis symmetry and a repeated pattern in the model, only $1/N_2$ sector of the fluid domain with periodic boundary condition is used in the CFD simulation of each design point. This helps significantly reduce the computational time for the DOE study. Based on a detailed mesh independence study performed for the baseline

seal model, a 2.17 million grid elements model is selected as the best trade-off between computational time and accuracy of the solution. All CFD models with a higher mesh resolution result in a less than 2% difference in leakage rate response [58]. Near the rotor surface, a finer mesh with inflation layers is used to capture the most important flow features. A detailed view of the mesh is shown in Figure 3-21. The mesh for each independent design point is automatically generated using the mesh sizing setup for the 2.17 million grid element model for the baseline seal configuration.

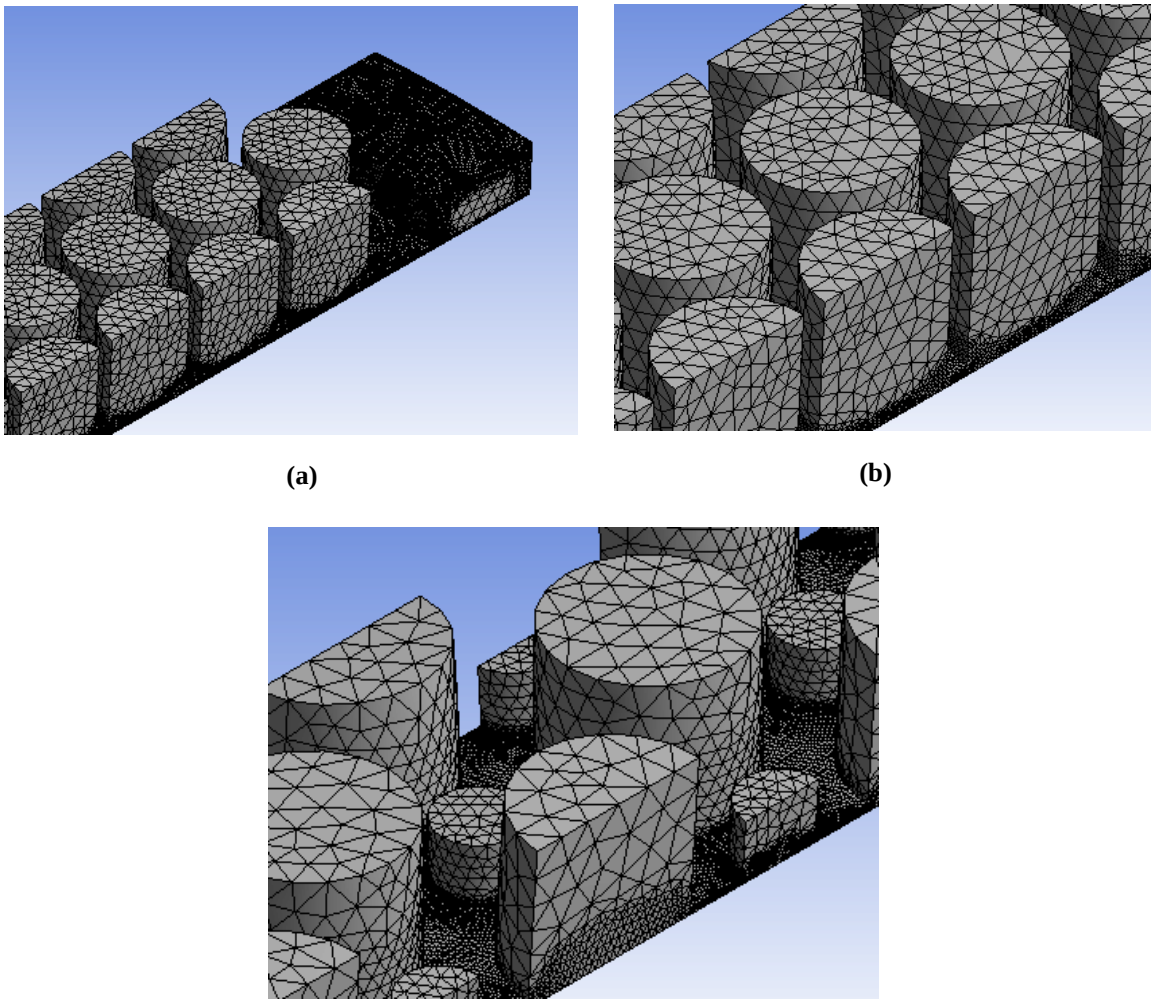

(a) **(b)**

(c)

Figure 3-21. View of Mesh for Baseline Model (b) Detail View (c) One of the Design Point

The operating conditions are specified based on the experimental setup from the literature. The whole fluid domain has a 20,200 RPM rotational speed, and the rotor surface is counter rotating. The inlet pressure is set to 7 MPa, and outlet pressure is 3.15 MPa. The turbulence model is k-ε. The steady state simulation results are initially generated for the baseline seal model. For each of the design points, the results of the baseline model simulation are used as an initial condition to further save time for CFD simulation. The setup of CFX-pre is shown in Figure 3-22. A list of the CFD setup is shown in Table 3-6.

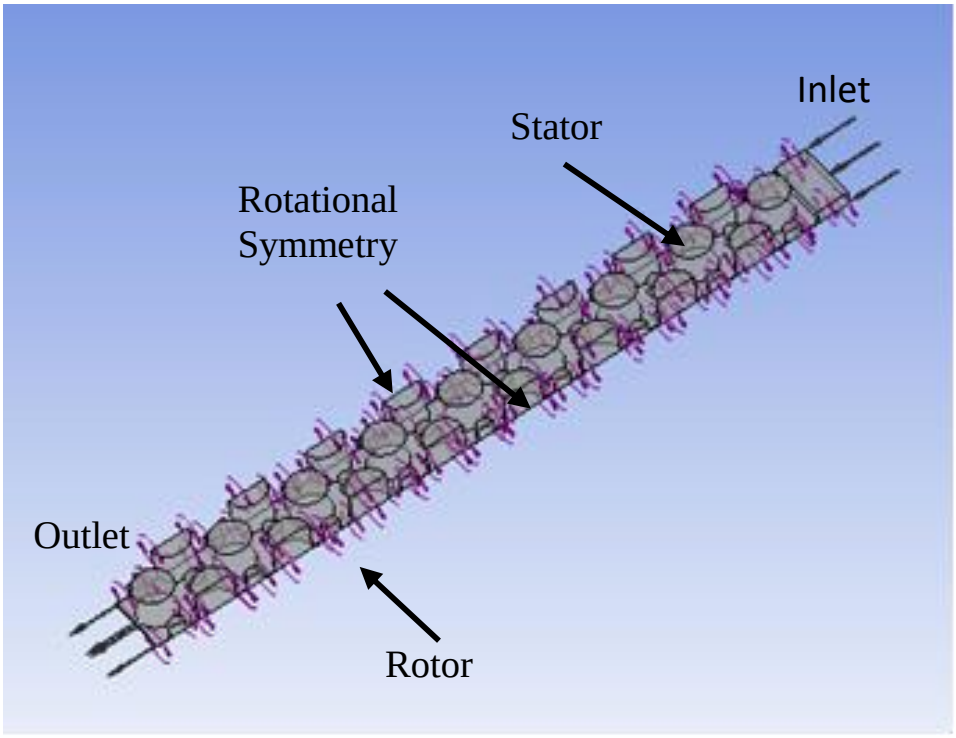

Figure 3-22. CFD Setup View - Alternately Arrange Hole-Pattern Seals

Table 3-6: Boundary Conditions – Alternately Arrange Hole-Pattern Seals

Parameter name	Value
Rotor Rotating Speed	20,200 [rpm]
Inflow Pressure	7 [MPa]
Exit Pressure	3.15[MPa]
Fluid Material	Ideal Air
Heat Transfer	Isothermal
Turbulence Model	k-ε
Analysis Type	Steady State

For the baseline seal model, the CFD results are compared to the measured value for the leakage rate, indicating less than 1% difference. The simulation result correlates well with the experimental data, thus validating the CFD model.

3.2.3 Results and Discussion

The responses of the design space, including the leakage rate obtained directly from CFD simulation and the rotor dynamic coefficients derived using the hybrid CFD/Bulk flow method, are used to generate reduced quadratic regression models. These reduced quadratic regression models are obtained performing backward elimination on full quadratic least squares regression models.

The leakage rate ranges from 0.369 kg/sec to 0.445 kg/s in the design space. For the baseline model, the leakage was 0.407 kg/sec, and the optimal case shows 9.3% improvement from the baseline model. The R-squared value is 0.9668. The reduced regression model for the leakage rate is given by Eqn. 3-17.

$$\begin{aligned} Leakage = {} & 0.480 + 0.044R_1 - 0.059c + 0.055H_1 \\ & + 2.79316 \times 10^{-3}N_1 - 1.23 \times 10^{-4}N_2 \\ & - 2.69 \times 10^{-3}R_1N_1 - 9.48 \times 10^{-4}R_1N_2 - 0.039cH_1 \\ & + 9.83 \times 10^{-4}cN_2 - 6.17 \times 10^{-4}H_1N_1 \end{aligned} \qquad \textbf{Eqn. 3-17}$$

The response surfaces for leakage rate are shown in Figure 3-23. From literature [58], the leakage rate is proportional to the total area of the holes on the seal surface. The response surface indicates that the ratio of smaller hole radius to larger hole radius is not that important to the leakage rate. The number of holes and the radius of the larger holes affect the leakage since they contribute more to the total area of the holes. In practice, in order to reduce the leakage rate, the total area of the holes on the seal surface should be as high as possible. The alternate arranged pattern proposed in this study is a good way to adjust the total area of holes leading to an efficient and novel seal surface patterning.

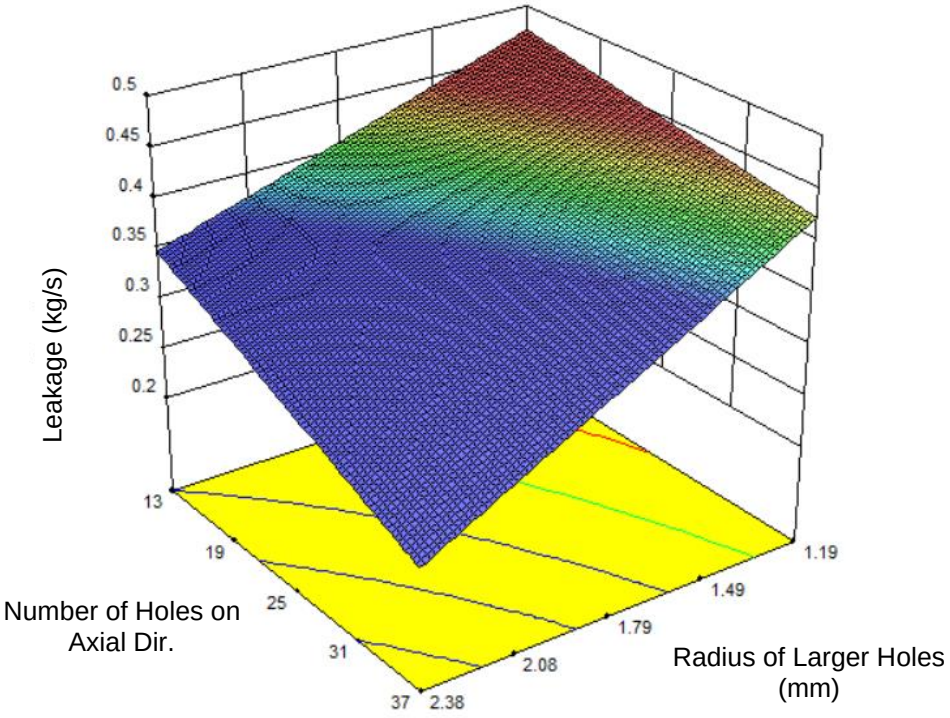
Leakage (kg/s)
0.5
0.45
0.4
0.35
0.3
0.25
0.2
13
19
25
31
37
Number of Holes on Axial Dir.
2.38
2.08
1.79
1.49
1.19
Radius of Larger Holes (mm)

(a)

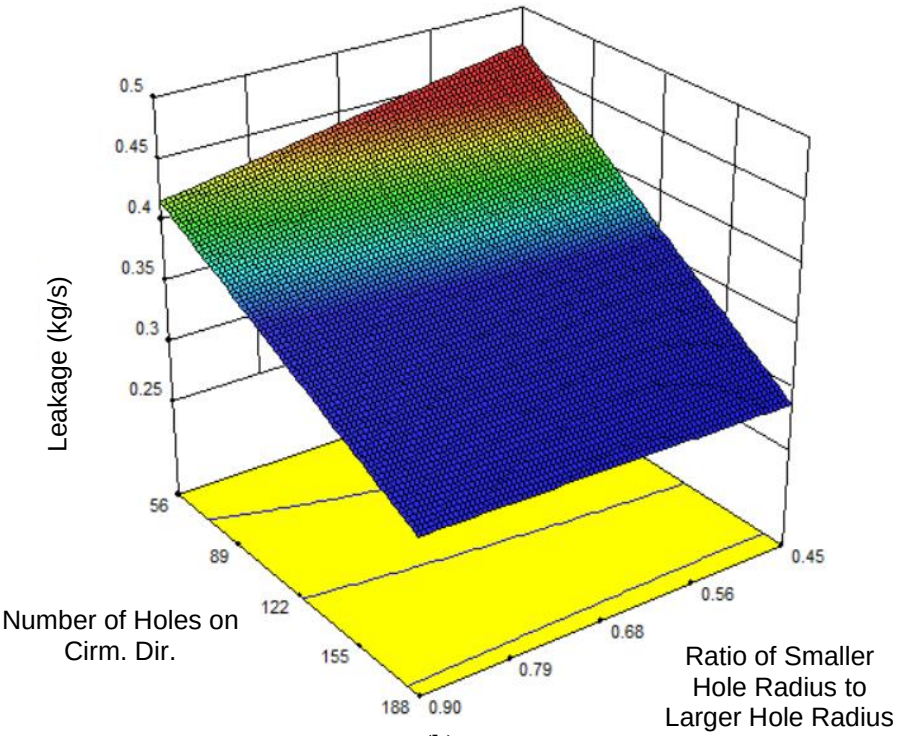
Leakage (kg/s)
0.5
0.45
0.4
0.35
0.3
0.25
56
89
122
155
188
Number of Holes on Cirm. Dir.
0.90
0.79
0.68
0.56
0.45
Ratio of Smaller Hole Radius to Larger Hole Radius

(b)

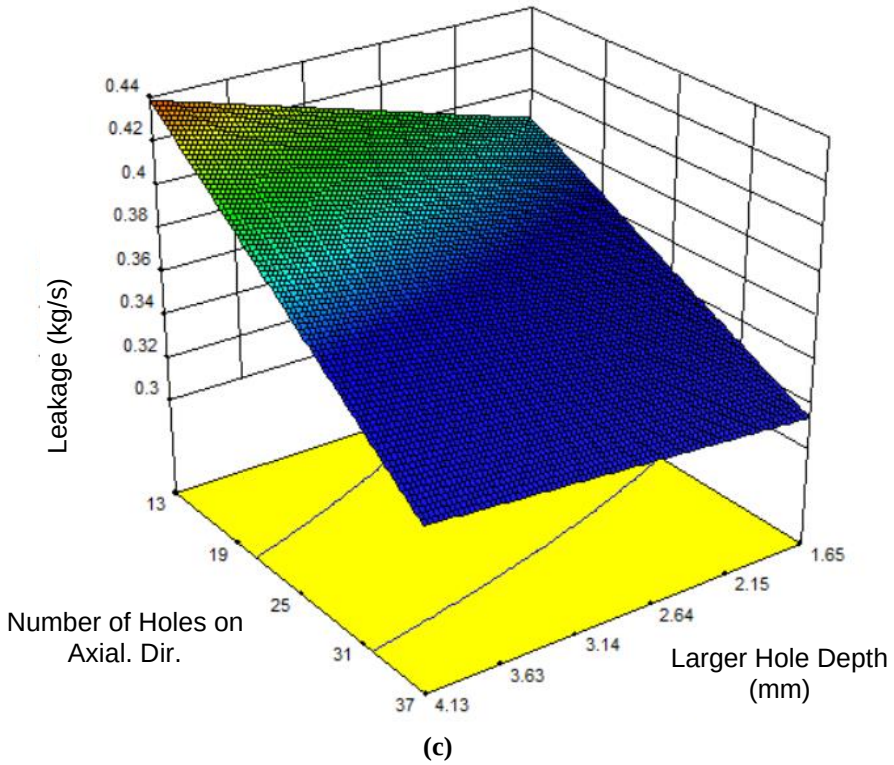

(c)

Figure 3-23 Response surfaces - leakage rate (kg/sec) (a) N_1 vs. R_1 (b) N_2 vs. c (b) N_1 vs. H_1

The direct stiffness ranges from 22,170 kN/m to 50,980 kN/m in the design space considered. For the baseline model, the direct stiffness was 29,400 kN/m. The R-squared value is 0.9809. The reduced regression model is given by Eqn. 3-18.

$$K_{XX} = 2.01 \times 10^8 - 8.99 \times 10^7 R_1 + 8.93 \times 10^7 c - 3.54 \times 10^6 H_1 - 3.59 \times 10^6 H_2 - 1.80 \times 10^6 N_1 - 4.29 \times 10^5 N_2 + 8643 N_1 N_2 + 1.83 \times 10^7 R_1^2 - 7.95 \times 10^7 c^2 \quad \textbf{Eqn. 3-18}$$

The response surfaces for the direct stiffness are shown in Figure 3-24. From the regression model, the direct stiffness is mainly determined by the number of holes, in both axial and circumferential directions. Since the number of holes in both directions determines the basic pattern of the alternately arranged hole-pattern, one can observe that the pattern of

the holes is essential to the direct stiffness. From the regression model, one can see that direct stiffness is higher if the number of holes in both directions is reduced.

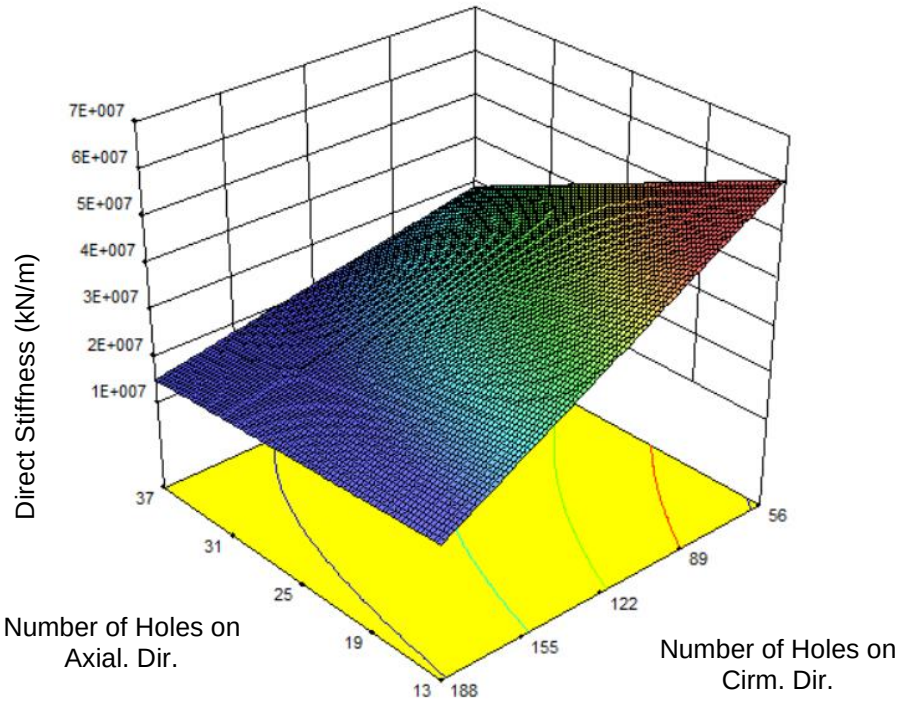

Figure 3-24 Response surfaces - direct stiffness (N/m) N_1 vs. N_1

The cross-coupled stiffness ranges from 4,230 kN/m to 33,220 kN/m in the design space. For the baseline model, the cross-coupled stiffness is 5,240 kN/m. The R-squared value is 0.9604. The reduced regression model is given by Eqn. 3-19.

$$K_{XY} = 1.745 \times 10^8 - 8.24 \times 10^7 R_1 - 9.00 \times 10^6 c - 1.72 \times 10^7 H_1 - 1.95 \times 10^6 H_2 - 1.60 \times 10^6 N_1 - 1.03 \times 10^5 N_2 + 2.59 \times 10^6 R_1 H_1 + 3.03 \times 10^5 H_1 N_1 + 1.43 \times 10^7 R_1^2 \quad \textbf{Eqn. 3-19}$$

The response surfaces for cross-coupled stiffness are shown in Figure 3-25. Only the three design variables related to the larger holes are present in these response surfaces, which implies that the geometry of the smaller holes does not have a significant effect on cross-coupled stiffness. The depth of holes also does not contribute significantly to this response. Increasing the radius of the holes and reducing the number of holes in the axial direction would increase this response.

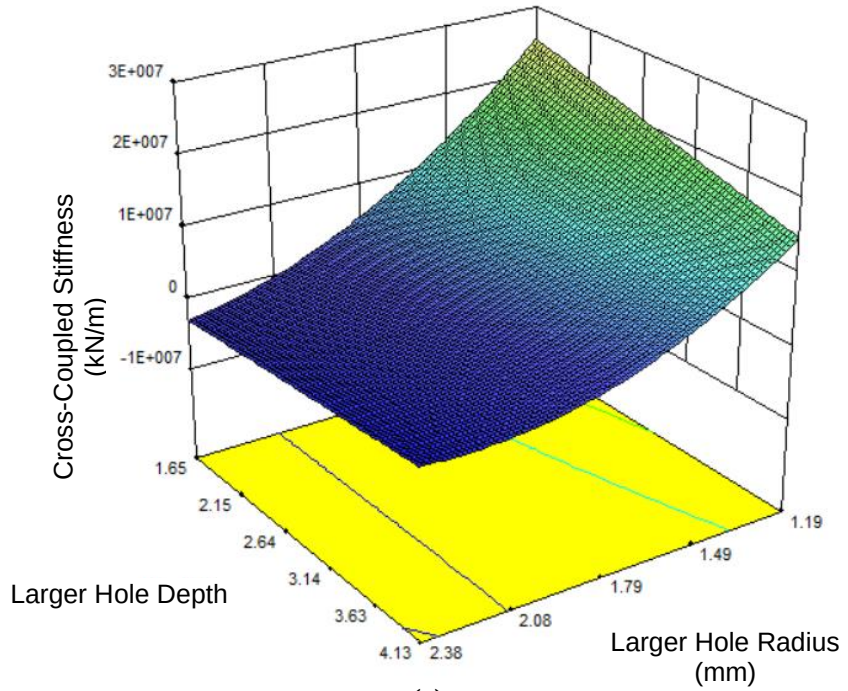

(a)

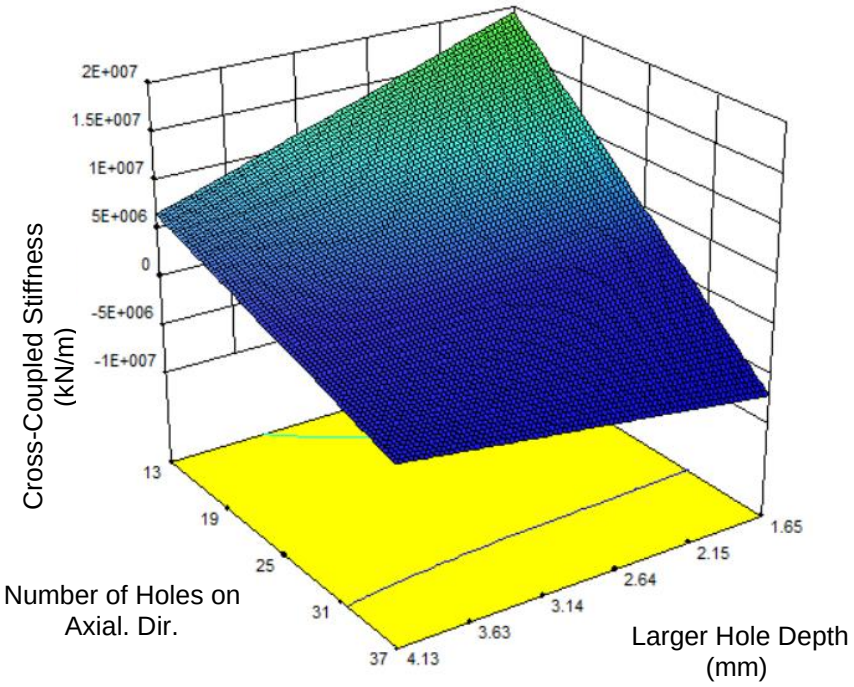

(b)

Figure 3-25 Response Surfaces of Cross-coupled Stiffness (N/m) (a) H_1 vs. R_1 (b) N_1 vs. H_1

The direct damping ranges from 3,070 kNs/m to 22,320 kNs/m in the design space. For the baseline model, the direct damping is 4,060 kNs/m. The R-squared value is 0.9594. The reduced regression model is given by Eqn. 3-20.

$$C_{XX} = 49200 - 1586R_1 - 6381c - 3883H_1 - 3907H_2 - 368N_1 + 54.8N_2 - 73.2R_1N_2 + 633H_1H_2 \quad \textbf{Eqn. 3-20}$$

The response surfaces for the direct damping are shown in Figure 3-26. The effect of both hole depths for the larger holes and smaller holes is relatively significant. From Figure 3-26(a), one can see that part of the response surface is relatively flat, which means that if the hole radius is small, the effect of the number of holes in the circumferential direction is also small; and this phenomenon also holds for the effect of the hole radius if the number of holes in the circumferential direction is small. Note that the negative number shown in Figure 3-26(a) is just from the response surface, no actual design point has a negative direct damping. Decreasing the number of holes in both directions would significantly increase direct damping. Increasing the larger hole diameter and the number of holes in the circumferential direction would reduce this response.

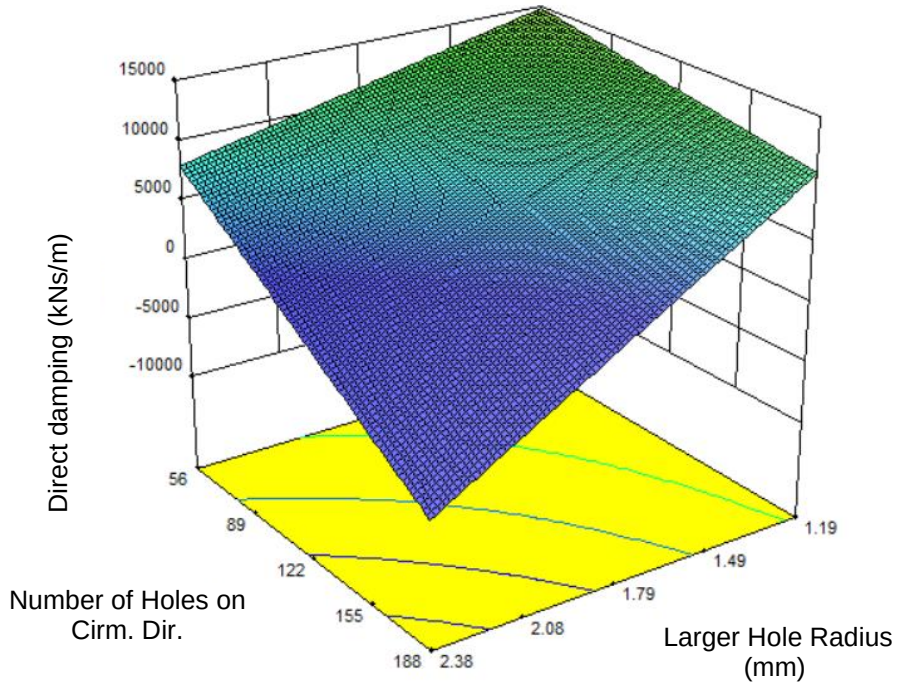

(a)

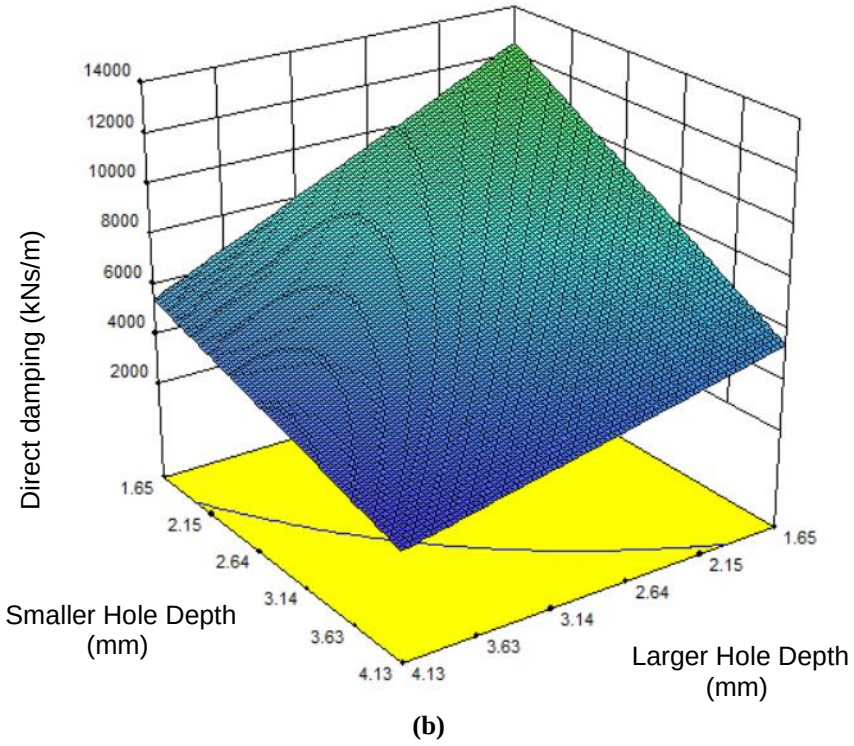

(b)

Figure 3-26 Response Surfaces of Direct Damping (Ns/m) (a) N_2 vs. R_1 (b) H_2 vs. H_1

The effective damping for all 25 design points ranges from 1,475 kNs/m to 9,973 kNs/m. For the baseline model, the effective damping was 1,590 kNs/m. The R-squared value is 0.9641. The reduced regression model is given by Eqn. 3-21.

$$C_{eff} = 13635 - 3647R_1 - 5148H_1 - 1316H_2 - 68.1N_1 + 649R_1H_1 - 426R_1H_2 + 345H_1H_2 + 698H_1^2 \quad \textbf{Eqn. 3-21}$$

The response surfaces for the effective damping are shown in Figure 3-27. One can observe that the most important design variables related to the effective damping is the hole depth for both the larger and smaller holes. In the previous study, the hole depth is set to be uniform all over the stator. However, in this study, by setting up two different hole depths set on adjacent rows, the effective damping is found to vary significantly. The noteworthy effect of alternating hole depths is shown in Figure 3-27(c). The effect of the hole radius is

less important than the hole depth, and this can be observed in Figure 3-27(a) and Figure 3-27(b). In order to achieve a higher effective damping, the number of holes in both directions should not be very high. Increasing the depth of the holes would also decrease the effective damping. The reason for the change induced by modifying the depth of holes may come from introducing a similar effect to the swirl brakes. These attempt to block the circumferential flow, reduce the circumferential velocity, and consequently reduces the cross-coupling effects leading to lower values for the cross-coupled stiffness.

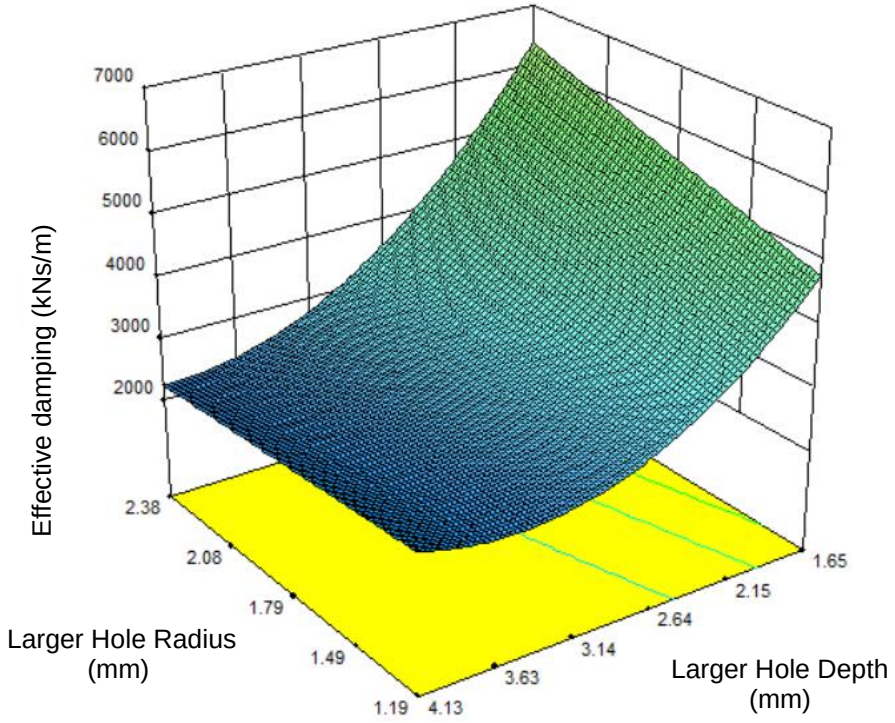

(a)

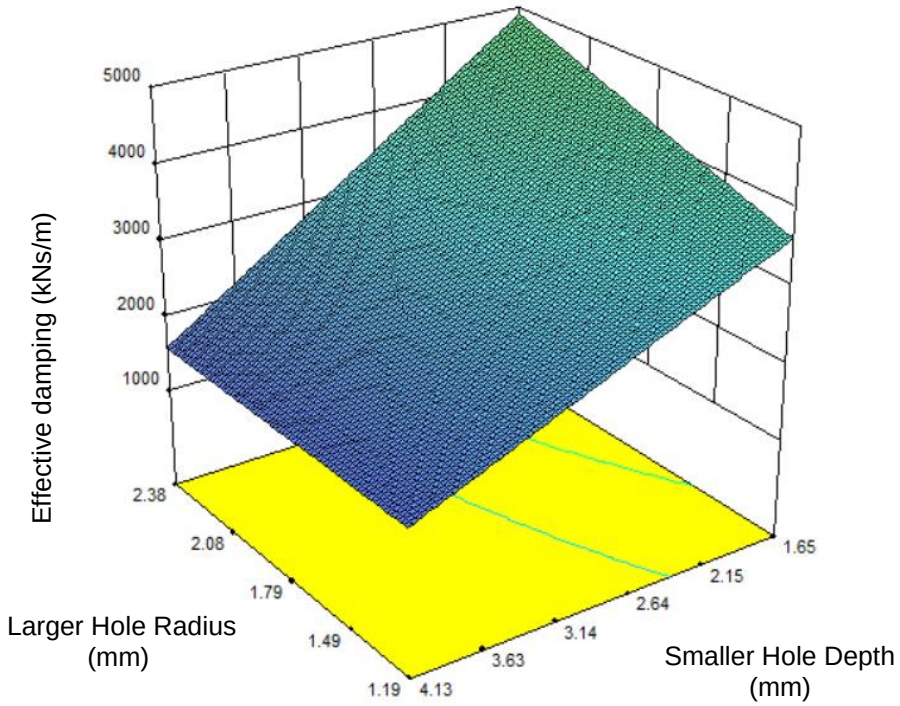

(b)

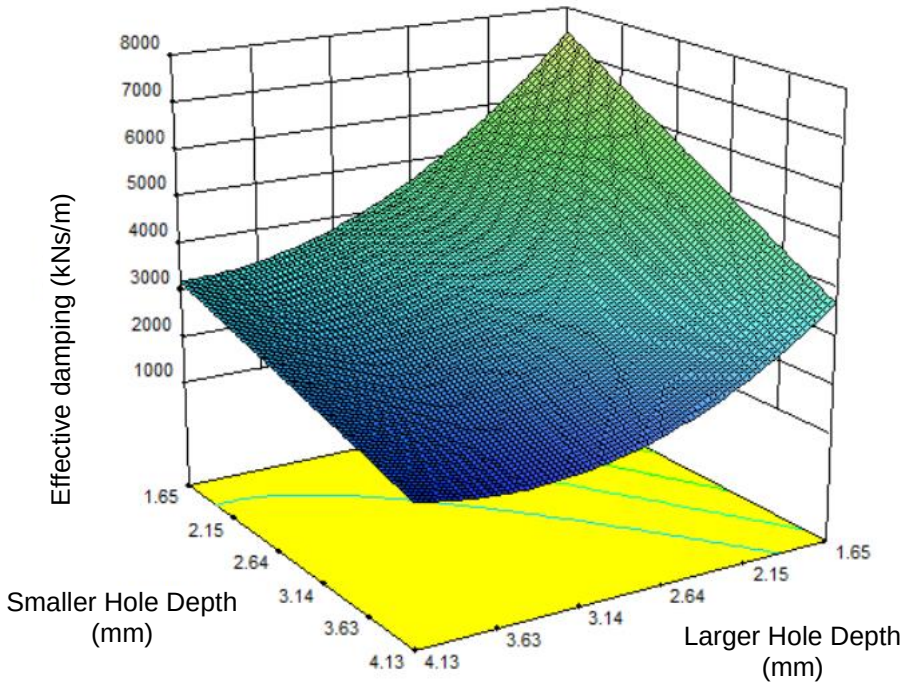

(c)

Figure 3-27 Response Surfaces of Effective Damping (a) R_1 vs. H_1 (b) R_1 vs. H_2 (c) H_2 vs. H_1

A good example of a geometry leading to a higher value of the effective damping is given in Figure 3-28. Although the different depths for holes in adjacent rows are not necessary for obtaining a higher effective damping, a large difference exists in this model. In this case, the larger hole radius is nearly the same as the smaller hole radius which shows the relatively small effect of the size difference. The vector plot is shown in Figure 3-28(b). A simple vertex pattern is observed in both the shallow and deep cavities. The leakage rate performance is not as good as the effective damping in this model, which shows that all optimized design goals may not be able to achieve at the same time.

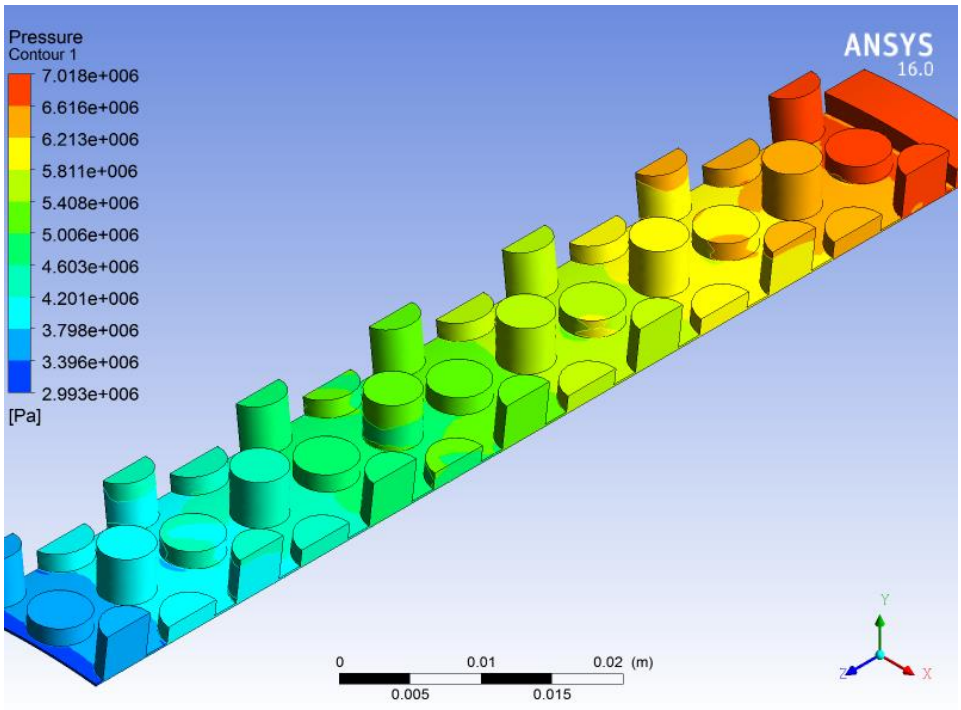

(a)

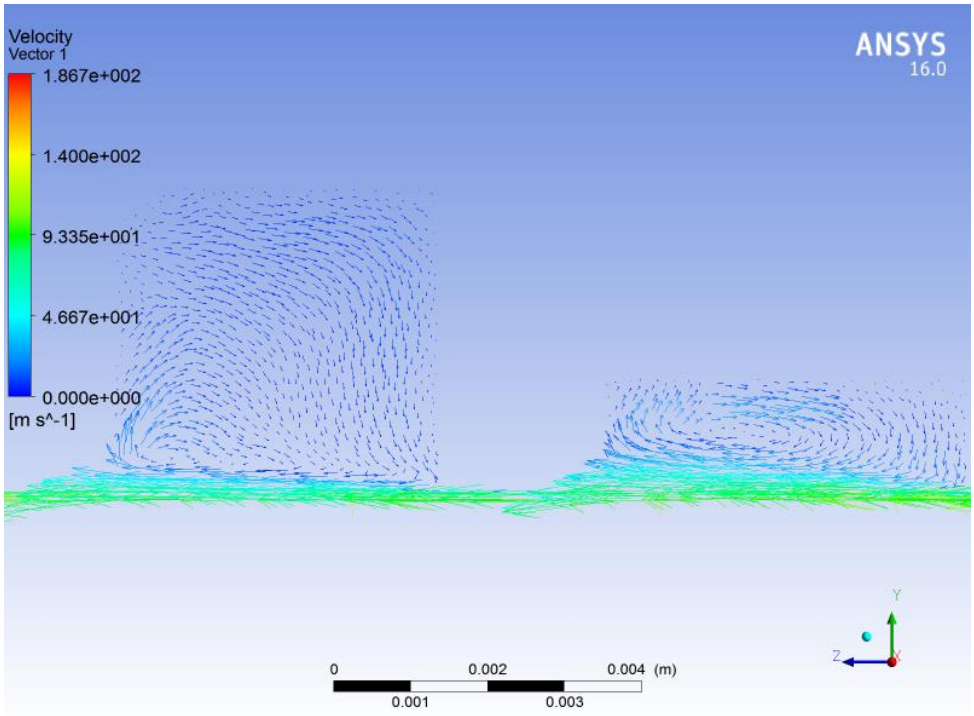

(b)

Figure 3-28 Example of Geometry with High Effective Damping Pressure Profile (b) Vector Plot

The alternately arranged hole-pattern effect on seal performance has been investigated in this study. Response surfaces for both leakage rate and rotor dynamic coefficients have been generated and the results shows that the alternately arranged hole-patterning has a significant effect on rotor dynamic response.

In terms of the leakage rate response, the results of this study agree well with the trends reported in the literature. The leakage rate is reduced when the total area of the holes on the stator surface increases. From the response surfaces generated from quadratic regression model, the radius of the larger holes and the number of holes in both directions are identified as relatively important factors. In order to minimize the leakage rate, the total area of the holes should be as high as possible.

For the effective damping, the regression model showed that the depth of the holes, for both larger holes and smaller holes, is very important for this response. The previous

studies mostly considered uniform hole depths, but in actuality, employing different depths on an alternately arranged hole-pattern design can significantly affect the dynamic characteristics of the seal.

The response surfaces generated in this study give a better understanding for the effect of varying the values of the design variables. Not only can the idea of using the alternately arranged pattern in the hole-pattern seal design improve the rotor dynamic response, but the regression model presented in this study can also be very helpful for an actual industrial seal design application. The sensitivity study in this study gives a new way to optimize the rotor dynamic response when designing a hole-pattern seal. As the roughness patterns have an effect on both leakage and dynamic response of a seal, a particular roughness pattern combination could be devised to satisfy different design requirements.

This study highlighted two important aspects that can lead to novel and more efficient seal designs: first, the use of the Design of Experiments methods to reduce the number of CFD cases that need to be run to perform a parametric analysis; second, concept of different arrangements for alternate hole-patterns. Typically, in practice, the entire annular seal surface is roughened with the same pattern. For future seal patterning designs, the depth of the holes is recommended to be modified separately using the alternately arranged hole-patterning. This is a novel feature of the seal's surface texturing that has not yet been considered in industry and warrants further investigations.

Chapter 4. Labyrinth Seals and Swirl Brakes

4.1 The Effects of Swirl Brakes Design on Labyrinth Seals

In non-contact annular labyrinth seals used in turbomachinery, the fluid pre-rotation in the direction of shaft rotation increases effectively the fluid velocity in the circumferential direction and could generate destabilizing fluid forces exerting on the rotor. Swirl brakes are typically employed to reduce the fluid pre-rotation at the inlet of the seal. The inlet flow separates as it follows the swirl brakes, and the ratio of the circumferential velocity away from the boundary layers to the velocity of the rotor surface varies consequently. Effective swirl brakes can suppress significantly the destabilizing fluid forces as it is effectively reducing the tangential velocity. In literature, it was shown that leakage rate can also be reduced by using swirl brakes with "negative-swirl".

In this case study, a labyrinth seal with inlet swirl brakes was selected as the baseline design and seal performance was evaluated using ANSYS-CFX. The design of experiments technique was used to illustrate the influence of various design variables to the seal performance. The design space consists of swirl brake's length, width, curvature at the ends, the tilt angle, as well as the number of swirl brakes in the circumferential direction. Simple random DOE sampling method with Euclidean distances for the design matrix is used to generate the design points. The steady-state CFD simulations were then performed for each design point to analyze the performance of the swirl brakes. The quadratic polynomial fitting was used to evaluate the sensitivity of the average circumferential velocity with respect to the design variables, which gives a qualitative estimation for the performance of the swirl brakes. The results provide a better understanding of which design variables are critical and more effective in reduction of the destabilizing forces acting on the rotor and thus will support the swirl brake design for the annular pressure seals.

The previous studies on swirl brakes mostly looked at swirl brakes with one fixed vane shape. In this paper, a parameter sensitivity study is performed using Design of Experiments technique to determine the effects of different geometry factors in design of

swirl brakes. The corresponding results are analyzed to study how the geometry variables are influencing the seal performance in terms of the leakage rate as well as the fluid circumferential velocity. Based on literature, the circumferential velocity is directly related to the stability of the system. To further study the key factor of the response, a derived parameter from two of the design variables is also given in the results section.

4.1.1 Computational Model and Parametrization

In this case study, the geometric parameters of the swirl brake model were chosen based on the results presented by an experimental study [1]. The model contains the swirl brakes and the labyrinth seal mounted downstream. The corresponding fluid domain is shown in Figure 4-1. The swirl brakes are evenly distributed along the circumferential direction. The geometric parameters of the labyrinth seal are fixed, while five geometric parameters associated with the swirl brakes were selected as design variables.

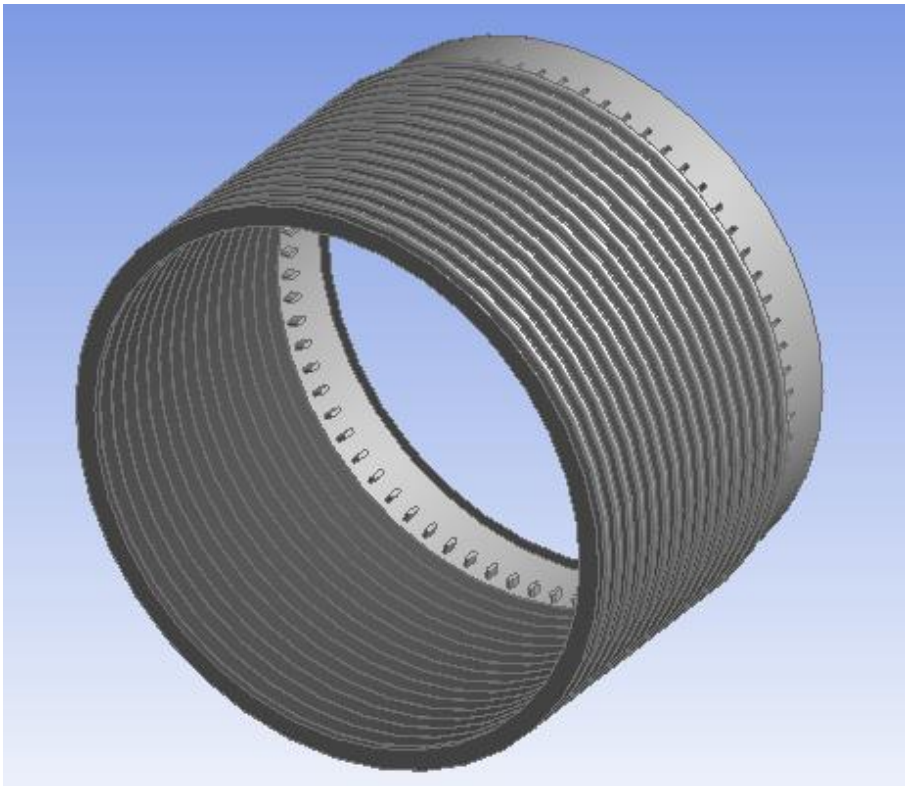

(a)

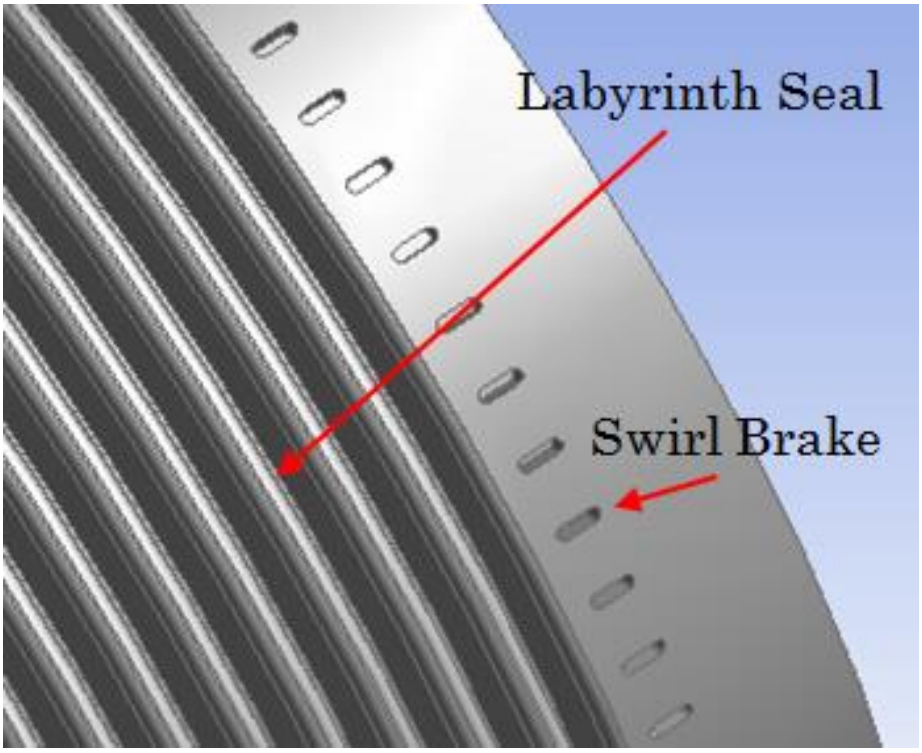

(b)

Figure 4-1 Fluid domain of the seal model. (a) Overview of the fluid domain. (b) Zoom in view of labyrinth seal and swirl brake

The model parameters associated with the geometry of the labyrinth seals and the clearance of the swirl brakes, which were kept constant in this study, are listed in

Table 4-1 and are illustrated in Figure 4-1. The baseline value of the five design variables for the swirl brakes as well as the variation ranges are listed in Table 4-2. They are also shown in Figure 4-2.

To reduce the number of unfeasible design points, a number of constraints were introduced in this model. These limiting features are similar to those used in literature [65-69]. The distance between the labyrinth seal and one end of the swirl brake was fixed Figure 4-3. On the other hand, it was imposed that the swirl brakes cannot extend to reach the inlet section. Therefore, the projected length of the swirl brakes along the axial direction is not allowed to exceed a certain value Figure 4-4. In addition, the swirl brakes are constrained

to avoid overlap with each other. Therefore, there is a minimum distance imposed along the circumferential direction between the two adjacent swirl brakes Figure 4-5.

Table 4-1 Constant Parameters – Swirl Brakes

Parameter	Description	Base Value
dr	Rotor Diameter	114.3 [mm]
cr	Radial Clearance of Seal	0.204 [mm]
ds	Seal Length	69.482 [mm]
sh	Labyrinth Seal Groove Height	4.2989 [mm]
sb	Labyrinth Seal Groove Width	4.0632 [mm]
θs	Labyrinth Seal Groove Incline Angle	15 [degree]
dg	Distance between Grooves	0.2794 [mm]
rc	Labyrinth Seal Groove Chamfer Radius	1.016 [mm]
c	Radial Clearance of Swirl Brakes	0.254 [mm]
h	Swirl Brakes Height	2.013[mm]

Table 4-2 Design Variables – Swirl Brakes

Parameter	Description	Base Value	Lower/Upper Bound
a	Length	2.2352 [mm]	1.016/8.9408 [mm]
b	Width	1.016 [mm]	0.254/2.3876 [mm]
r	Head Length	0.508 [mm]	0.127/1.6938 [mm]
θ	Tilt Angle	0 [degree]	-65/65 [degree]
n	Number of holes in circumferential direction	72	25/150

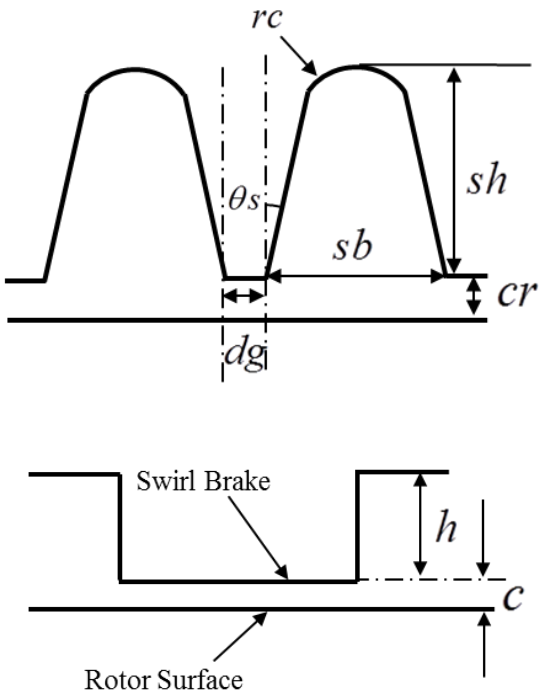

Figure 4-2 Fixed parameters

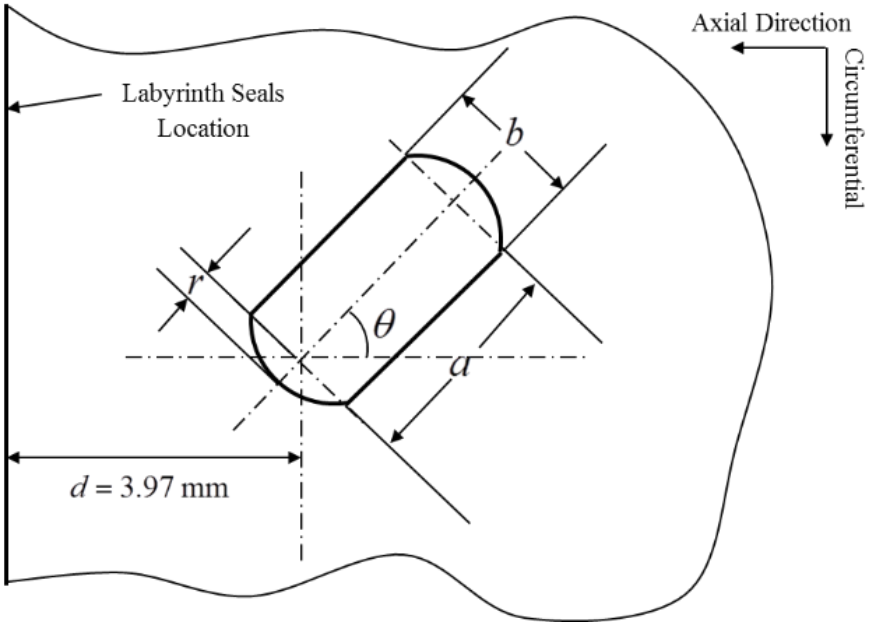

Figure 4-3 Design variables

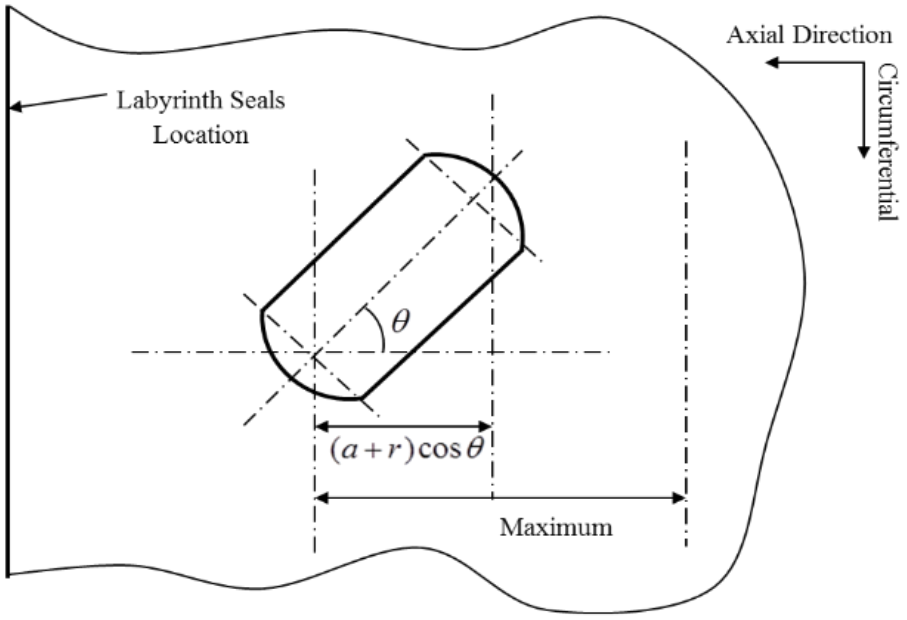

Figure 4-4 Constrain - axial direction

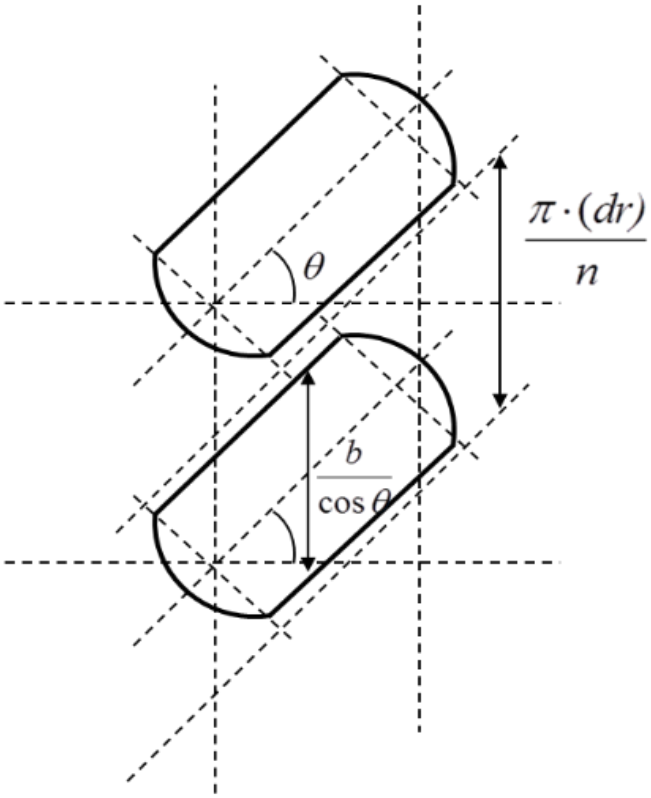

Figure 4-5 Constraint - circumferential direction

4.1.2 CFD Model and Numerical Analysis

The CFD model of the seal-swirl brakes assembly was created in ANSYS Design ModelerTM after all the geometry parameters were defined. The repeated pattern was used to simplify the fluid domain to 1/n fluid domain, with cyclic boundary condition on the two sides along the circumferential direction. This simplification reduced considerably the total simulation time. Unstructured mesh is used with inflations layers on both rotor surface and stator surface. The complete fluid domain and the sector model used in the CFD simulations are shown in Figure 4-6.

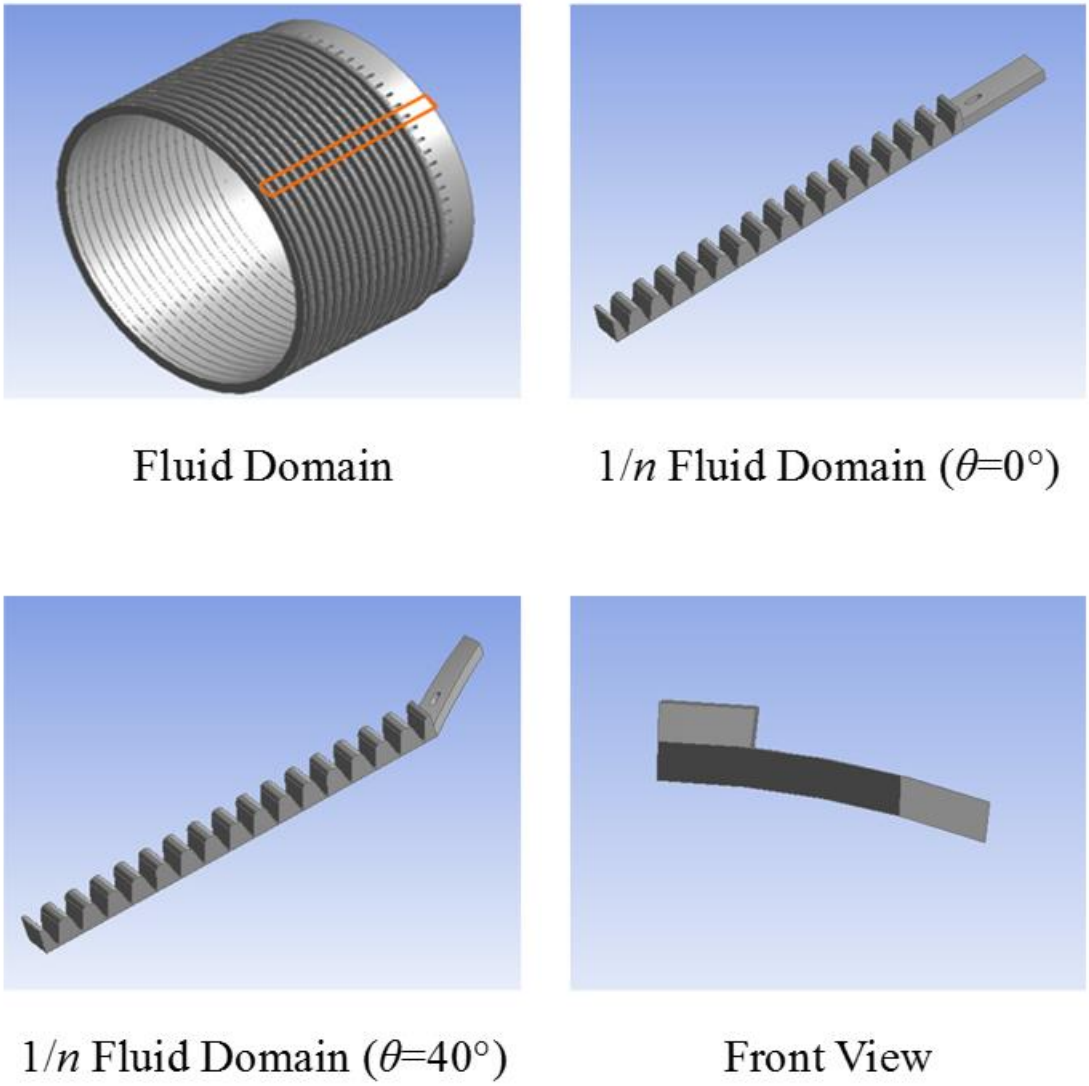

Figure 4-6 360 degree fluid domain and sector fluid domain

A mesh convergence study was performed for mesh setup of the baseline model. In this study, the mesh density is varied by defining the maximum element size across the domain. The same model with three different mesh densities show nearly same results in terms of the average pressure along the axial direction (Figure 4-7). For the average circumferential velocity along the axial direction, it is shown that higher mesh density beyond the 2,630,000 elements will not result in a significantly more accurate result (less than 1.2% difference). Thus, a model with 2,630,000 elements mesh was used in the DOE study. The overall mesh and a zoom in view for the inflation layer are shown in Figure 4-8.

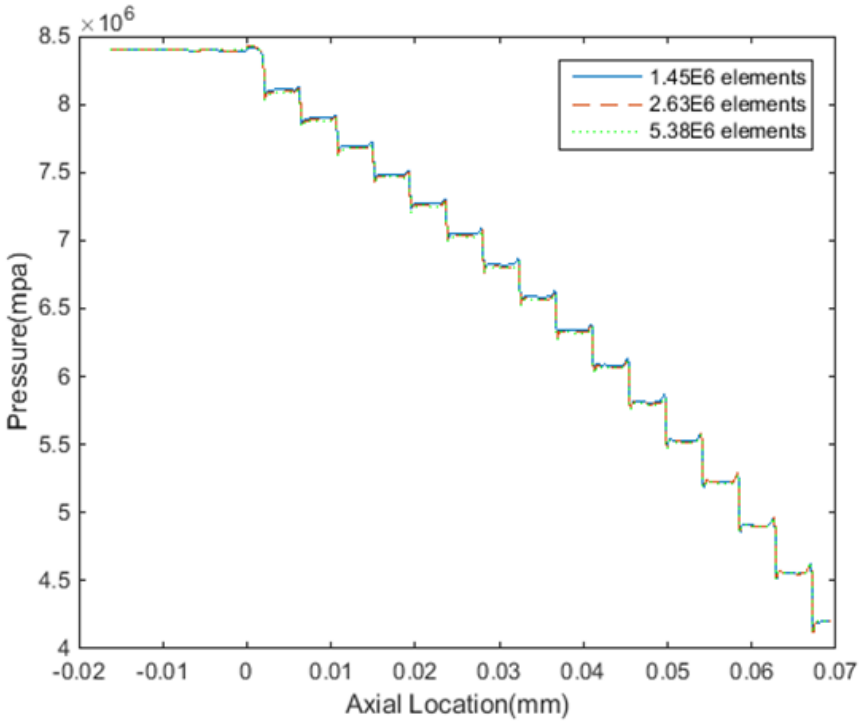

(a)

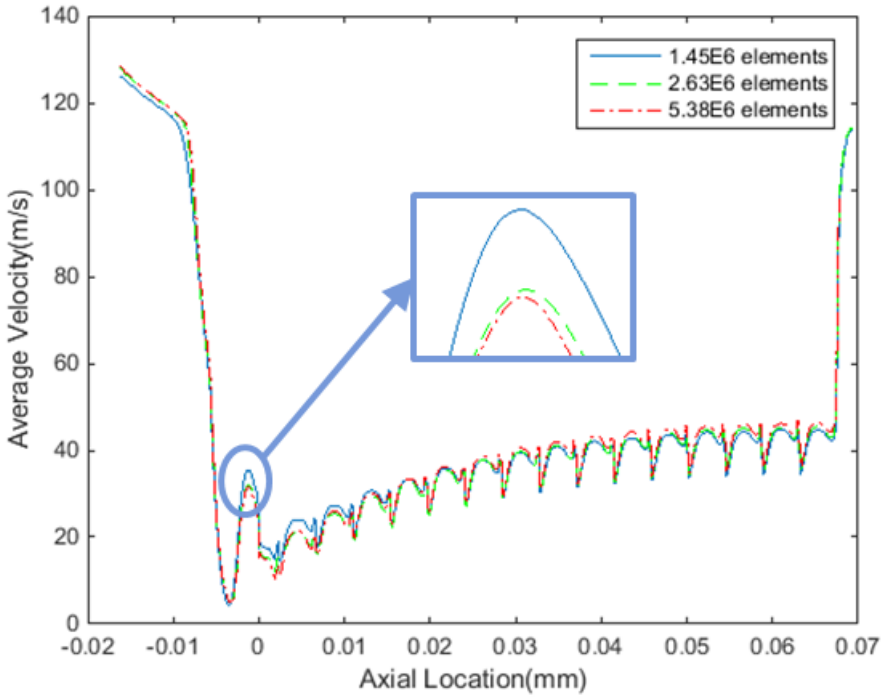

(b)

Figure 4-7 Plots with different meshes for (a) pressure (b) average velocity

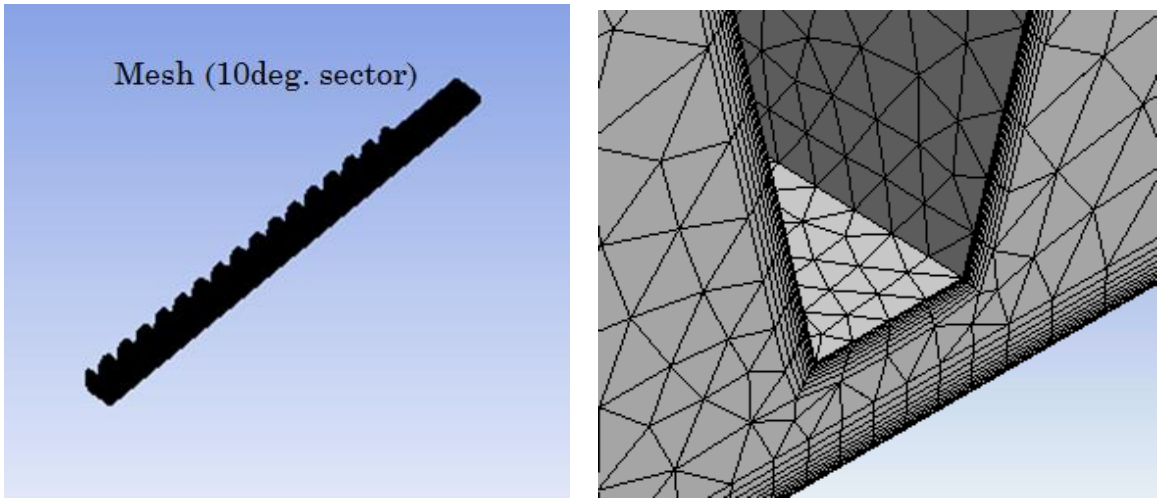

(a) **(b)**

Figure 4-8 Mesh of the 1/36 sector model. (a) Overview of the 1/36 sector mesh. (b) Mesh of the grooves.

The CFD simulations were performed using ANSYS CFX package. The fluid field was simulated under a steady state, isothermal condition. The operating conditions and boundary conditions were specified based on the experimental study from Childs et al.[1]. The whole fluid domain was assigned a 20,200 rpm angular velocity, and the rotor surface is counter rotating (Figure 4-9). The inlet and outlet pressure is 84 bar and 42 bar, respectively. The turbulence model in the domain is k-ε in conjunction with a scalable wall function. Details of fluid domain setup are listed in Table 4-3.

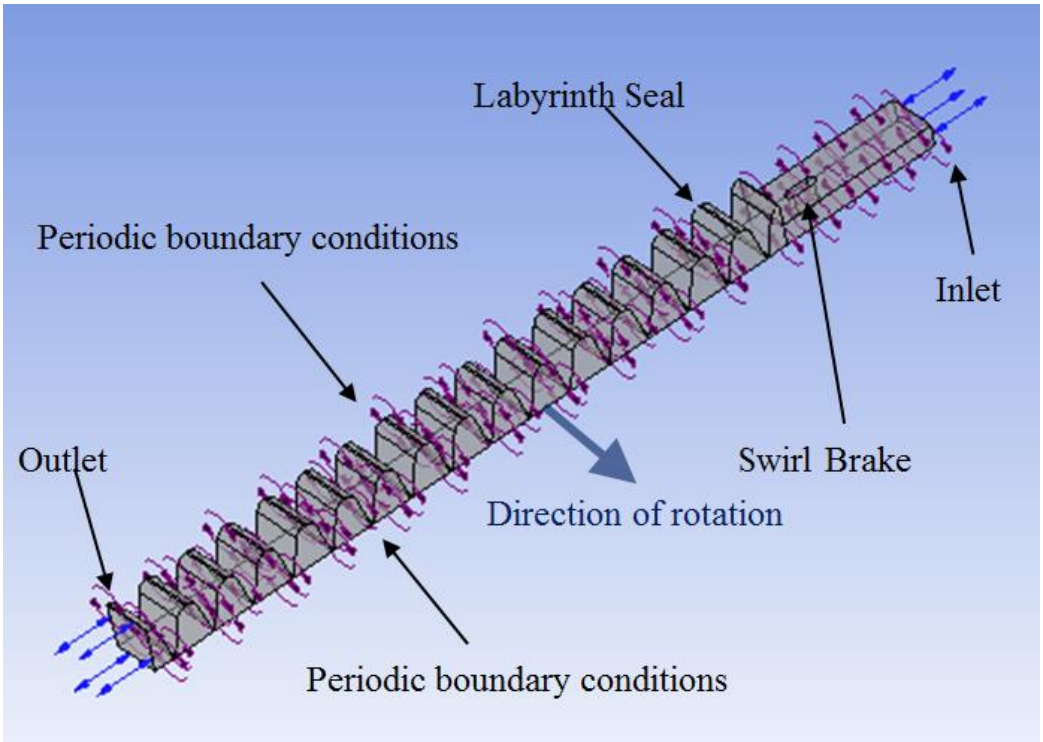

Figure 4-9 Fluid domain setup of swirl brakes

Table 4-3 Operating conditions and boundary conditions – Swirl Brakes

Parameter	Value
Rotor speed	20200 [rpm]
Inlet Pressure	84 [bar]
Inlet flow angle	45 [degree]
Outlet Pressure	42 [bar]
Working Fluid	Ideal air
Heat transfer	Isothermal
Turbulence Model	k-ε
Analysis Type	Steady state

4.1.3 Results and Discussion

The DOE results are analyzed with the statistics tools. The effects of initial 5 design variables are given first. In addition, to illustrate the real factor for circumferential velocity response, a derived parameter is presented.

The leakage rate and average tangential velocity at certain locations in the fluid domain were extracted from the CFX-post. The average tangential velocities were recorded in three different locations along the axial direction, which are the clearance region near inlet, near outlet and halfway between inlet and outlet (Figure 4-10). From this data, the average circumferential velocity V_t was estimated as the mean value of the circumferential velocity in those three locations. The rotor dynamic coefficients were not analyzed directly in this study. Instead, the circumferential velocity V_t was used to give a qualitative performance estimation of the cross-coupled coefficients. From Childs et al. [70], a lower circumferential velocity will result in reduced destabilizing cross-coupled stiffness coefficients.

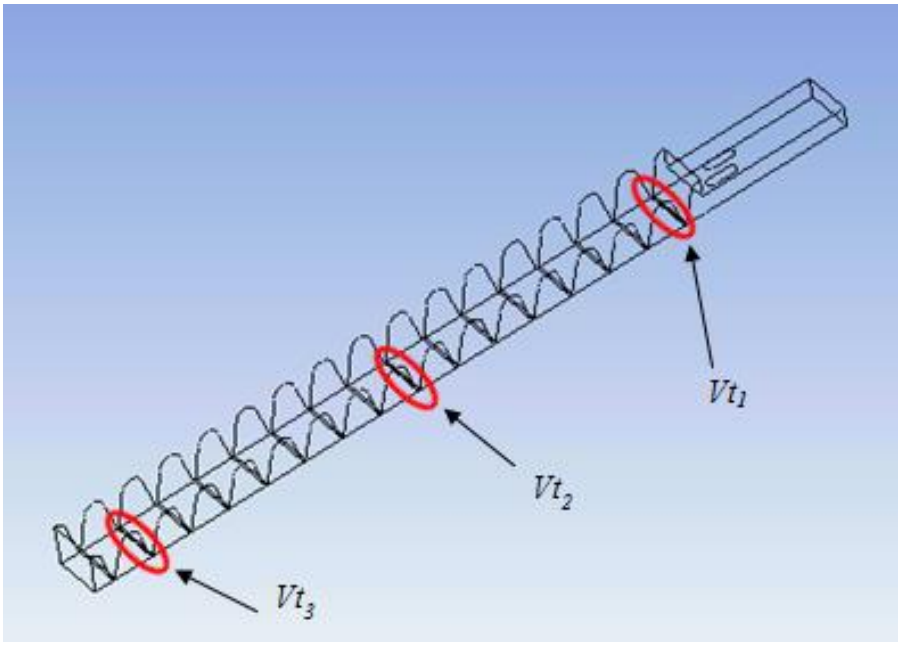

(b)

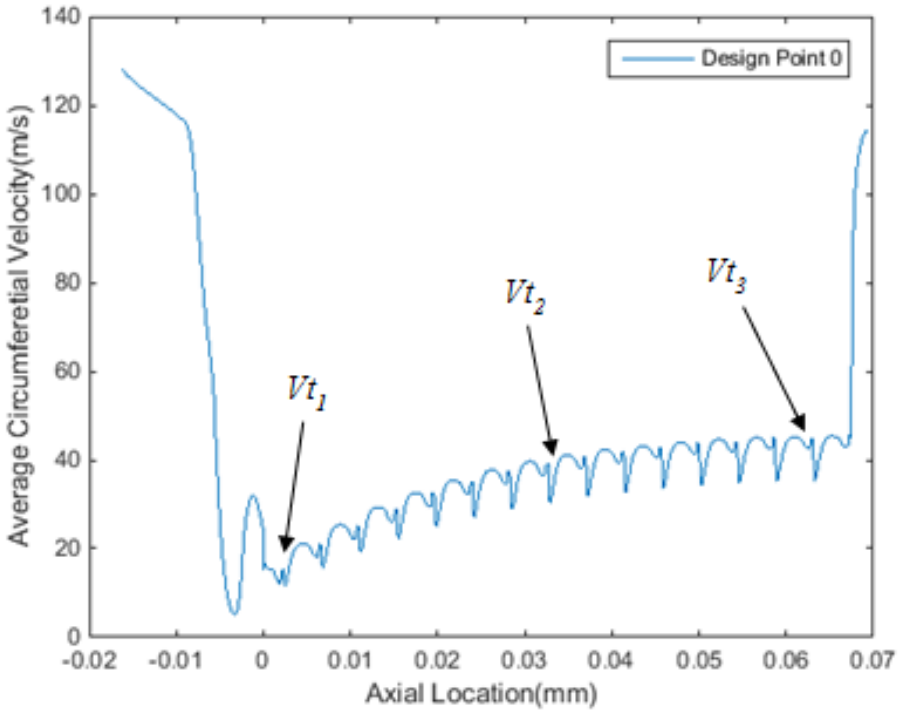

(b)

Figure 4-10 DOE outputs. (a) Locations shown in geometry (b) Locations shown in velocity profile along axial direction for baseline geometry

The DOE analysis results were extracted using Isight software. The Pareto Chart and the Main Effect Chart of the leakage rate are shown in Figure 4-11. From the Pareto Chart, it can be observed that the leakage rate is relatively sensitive to the magnitude of tilt angle, theta. Whereas, from the main effect chart, the minimum leakage rate among all the design points only has less than 5% improvement from the design point with maximum leakage rate. The R-square value is 0.73, which is relatively low. This implies that the regression model has the ability to cover only 73% of the data.

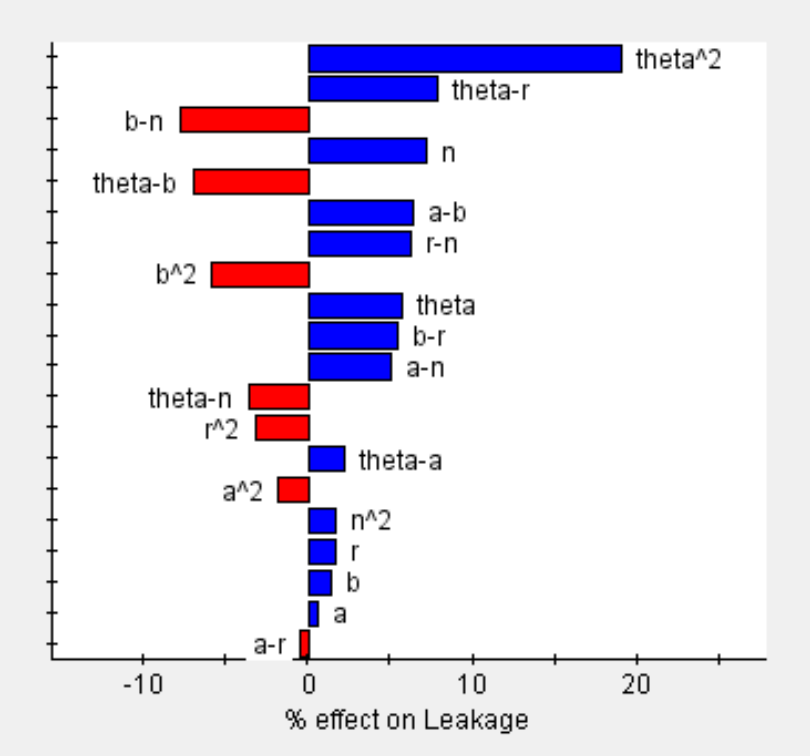

(a)

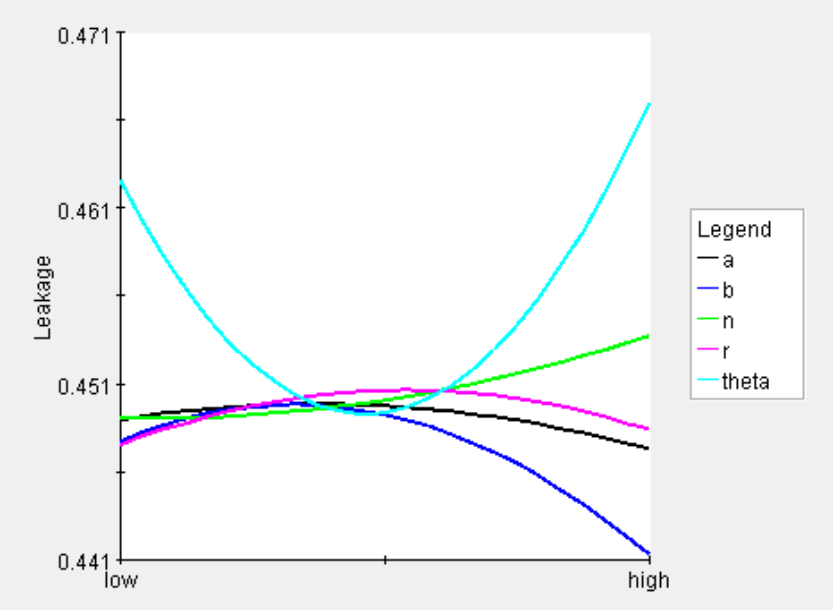

(b)

Figure 4-11 DOE analysis of leakage rate. (a) Pareto chart. (b) Main effect chart

The Pareto Chart and the Main Effect Chart of the average circumferential velocity are shown in Figure 4-12. From the two figures, one can see that the circumferential velocity is mainly affected by the tilt angle, theta, as well as the swirl brake length, a. The number of the swirl brakes along the circumferential direction has a less significant influence on the results. Even the swirl brake models with a lower value of vanes in the circumferential direction (less than 30 swirl brakes) were able to efficiently block the fluid flow in circumferential direction.

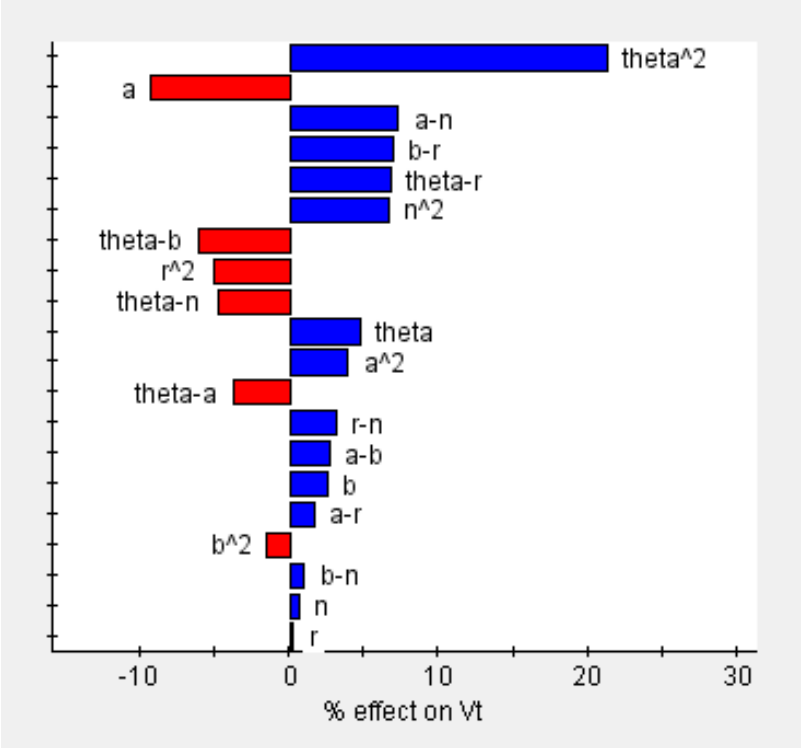

(a)

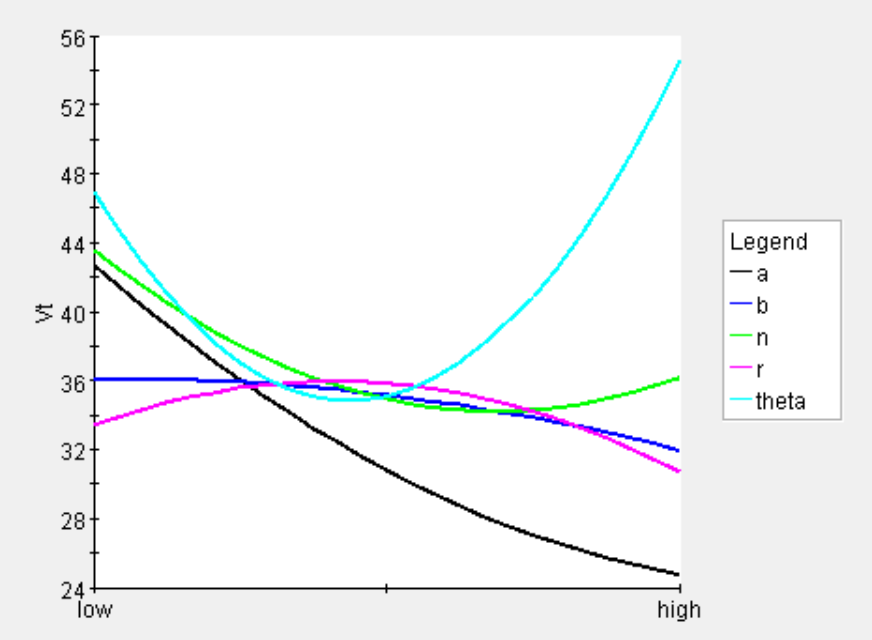

(b)

Figure 4-12 DOE analysis of circumferential velocity. (a) Pareto chart. (b) Main effect chart.

The fluid preswirl ratio was defined by the inlet circumferential velocity divided by the rotor surface speed. In the CFD model, data was extracted at a location downstream from the swirl brakes and right before the inlet of the labyrinth seal. The Pareto Chart and the Main Effect Chart of the fluid preswirl are shown in Figure 4-13. The results are very close to the circumferential velocity as expected. In this study, the average circumferential velocity was used as output for sensitivity study because of its better representation of the flow pattern inside the labyrinth seal, but analyzing the fluid preswirl ratio has similar results.

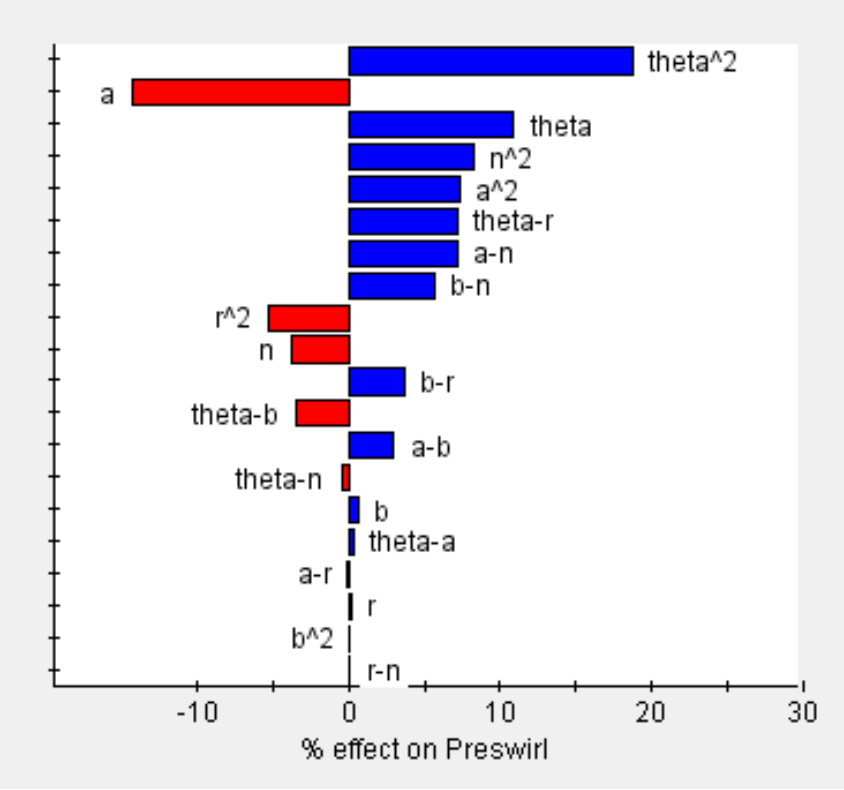

(a)

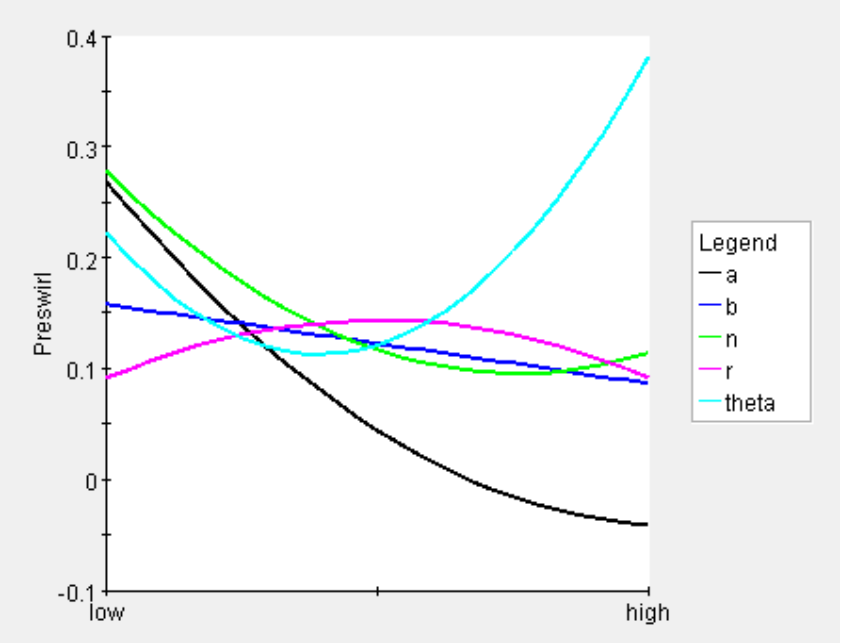

(b)

Figure 4-13 DOE analysis of preswirl ratio. (a) Pareto chart. (b) Main effect chart

The direct analysis of the design variables on the circumferential velocity was not as clear as expected. To better understand the relationship between the design variables and the output, which in this case is the circumferential velocity, a new variable, called the effective swirl brake length, was introduced through the swirl brake length a and the tilt angle θ. The effective swirl brake length (effective a, Figure 4-14) is the projected swirl brake length a along the angle β (effective angle,) which is determined by the upcoming flow direction. Overall, the effective swirl brake length could be associated to the efficiency of the swirl brakes in blocking the upcoming fluid flow.

The effective angle β was obtained numerically from the CFD simulations. Then, the effective swirl brake length a was computed by the formula $a \cdot cos(\beta+\theta)$. Note that the effective angle can be different according to the upcoming flow direction, which is illustrated in Figure 4-15.

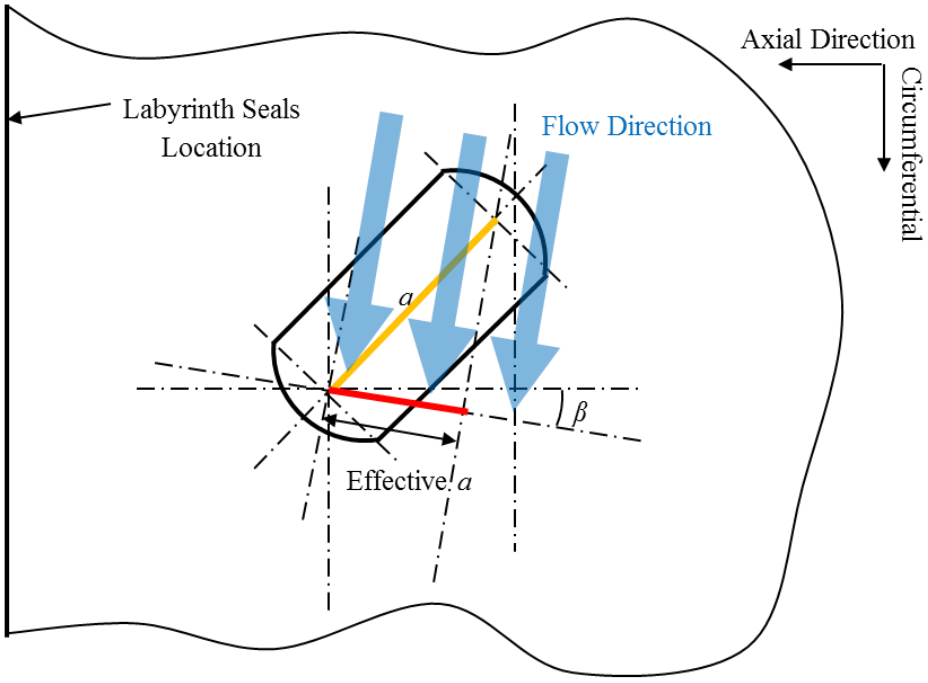

Figure 4-14 Effective swirl brake length

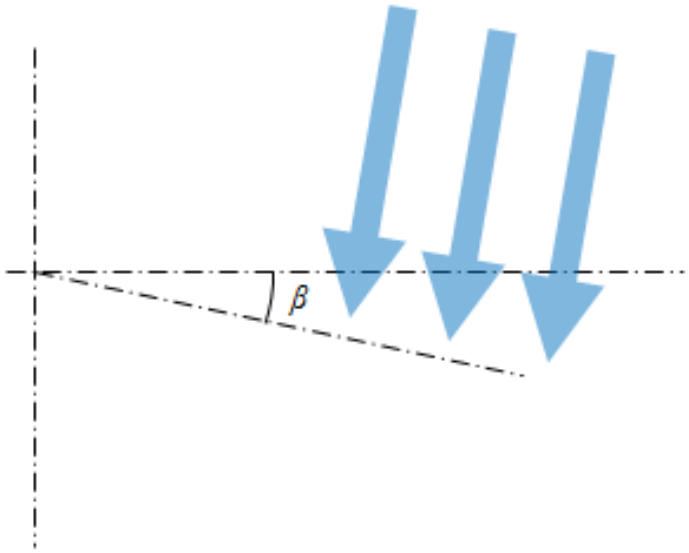

(a)

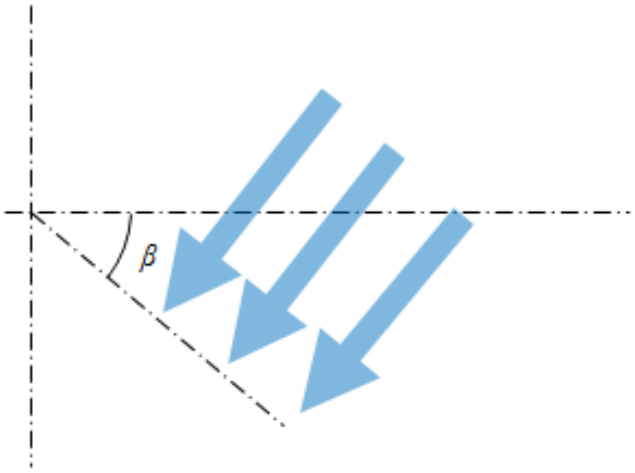

(b)

Figure 4-15 Effective angle. (a) High circumferential velocity. (b) Low circumferential velocity

A better understanding of the advantages related to the introduction of newly derived variables (effective swirl brake length and effective angle) are illustrated by plotting the swirl brake length/effective swirl brake length versus the circumferential velocity (Figure 4-16). The swirl brake length does not have a strong connection with the average circumferential velocity, therefore the design points are scattered all over the design space (Figure 4-16a). However, a good quadratic relationship with the circumferential velocity is observed for the effective swirl brake length (Figure 4-16b).

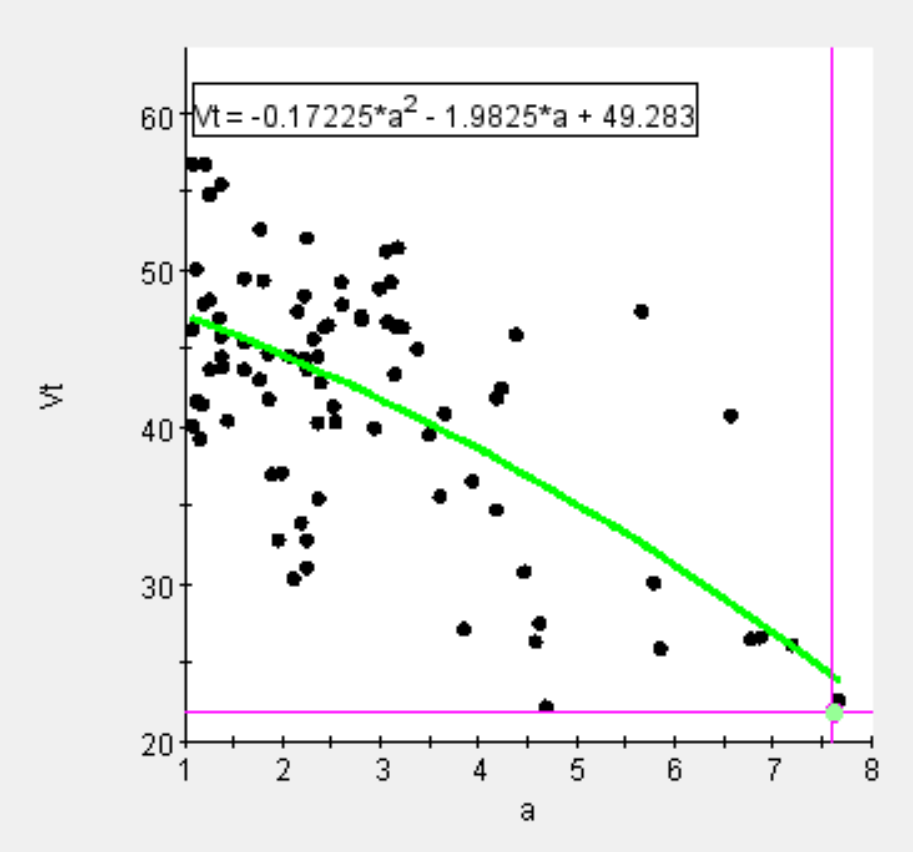

(a)

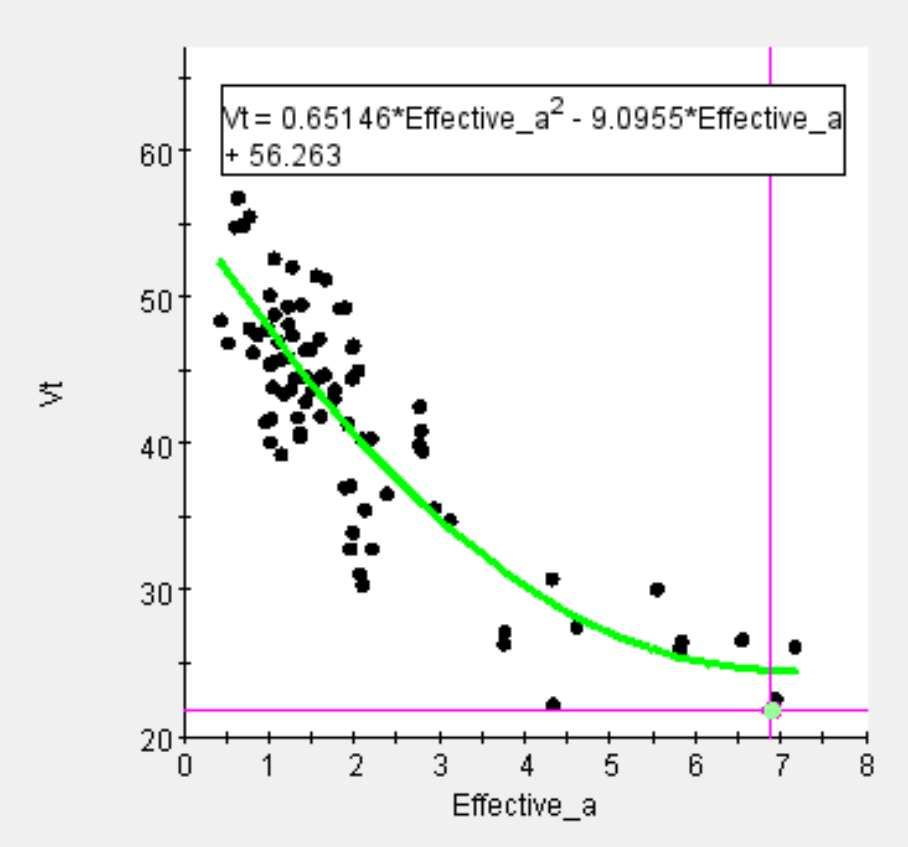

(b)

Figure 4-16 Circumferential velocity chart of Swirl brake length/Effective swirl brake length. (a) Swirl brake length. (b) Effective swirl brake length

Some examples of high performance models are shown in Figure 4-17. It is straightforward to observe how high efficiency swirl brakes look like for these models. The lengthier swirl brakes with an inappropriate tilt angle have a similar performance with shorter swirl brakes with a suitable tilt angle.

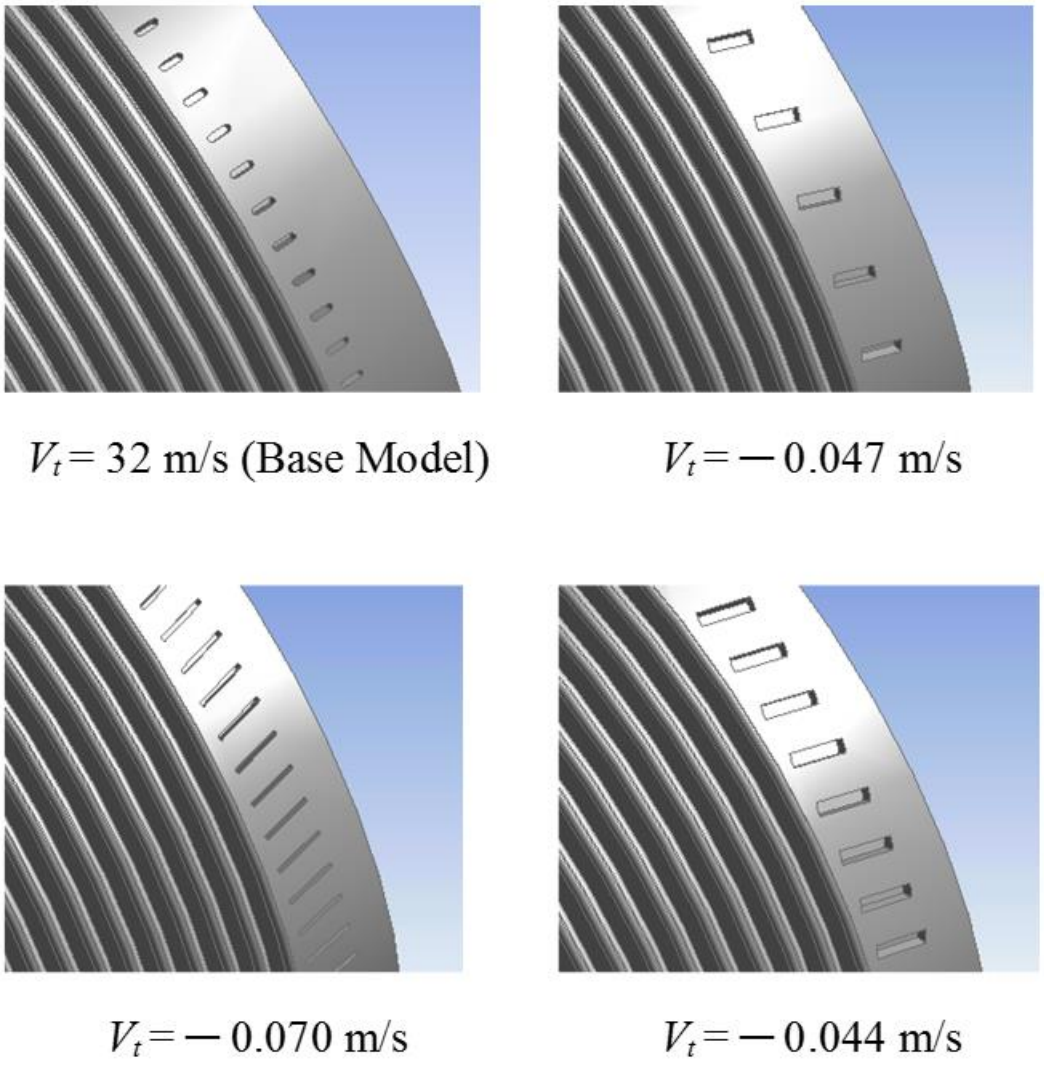

Figure 4-17 High performance model compare to the baseline model. Vt is the average circumferential velocity

This case study investigated different geometry factors of swirl brake design on effects of the performance of the non-contacting annular pressure seals used in turbomachinery. The leakage rate and the magnitude of the circumferential velocity are both analyzed using Design of Experiments technique combined with CFD simulations to assess the responses for each design point. Corresponding results are further evaluated using statistical analysis tools to get a better understanding of the co-dependence of the design variables on the outputs selected.

The results show that the swirl brakes assembled upstream of the labyrinth seal entrance have little influence on the performance of the annular pressure seals, and minimally influence the fluid leakage rate when the labyrinth seal geometry is constant. Therefore, for cases when annular seals are believed to introduce high cross-coupling forces, the so called fluid excitation forces leading to potential rotor dynamic instability conditions, swirl brakes can be added without a penalty in the sealing performance and ultimately on the overall efficiency of the turbomachine.

On the other hand, the results clearly indicate that circumferential velocity, which is directly related to the fluid cross-coupling effect on the rotor, can significantly be affected by swirl brake geometry. The magnitude of the circumferential velocity reduced by the presence of swirl brakes is mainly determined by the swirl brake effective length, which is a parameter introduced in this study to facilitate a deeper understanding of the DOE results. The effective length of the swirl brakes is not only controlled by the length of the vanes and the tilt angle but is also determined by the circumferential and axial velocity resulting from the upstream flow conditions. In addition, the results show that the number of vanes is not closely related to the magnitude of the circumferential velocity if the vanes are dense enough in the circumferential direction. It is well-known that a reduced circumferential velocity will result in reduced destabilizing cross-coupled stiffness coefficients. To design swirl brakes that efficiently reduce the destabilizing cross-coupled fluid forces and stiffness coefficients, the swirl brake effective length introduced in this study is a valuable design factor to consider.

4.2 Leakage Rate Performance - Smooth Stator/Grooved Rotor Labyrinth Seals

As one of the most widely used annular pressure seals, labyrinth seals are used to reduce the fluid leakage between different pressure stages. They are multi-toothed seals with circumferential grooves located on the rotor surfaces and/or stator surfaces, which are distributed along the axial direction. The intricacy of the surface geometry and directionality of the seal pattern assist in converting pressure into dissipated kinetic energy

without rotor-stator rub effects. The majority of previous studies focused on annular labyrinth liquid seals with smooth rotor/grooved stator (SR/GS) case, whereas this study attempts to elucidate the effects of geometric variables modification for smooth stator/grooved rotor (SS/GR) case using CFD and DOE techniques. In this study, a smooth stator/grooved rotor liquid seal was modeled and validated against experimental data. The model was then used as a baseline case for a sensitivity analysis of its geometry variations. Simulation results under different pressures/rotor speeds were used to validate the CFD setup. Four geometric parameters of the seal were then selected as design variables to adapt the baseline geometry for potential performance improvements. The design space was discretized using the DOE technique. Similar mesh/simulation setups were automatically generated for each design point. Regression analysis was applied based on the CFD results for a better understanding of the effects associated with different design variables. These results can be used to improve the current design of smooth stator/grooved rotor annular pressure seals in order to achieve lower leakage rates.

This case study focused on tooth-on-rotor case of labyrinth seals for leakage rate prediction. The geometry of smooth-stator/grooved-rotor (SS/GR) type of seal was studied using CFD and design of experiments techniques. The design variables included width of the grooves, depth of the grooves, tilt angle of the grooves with respect to the axial direction, and the number of grooves. The output of DOE study was mainly focused on leakage rate. For each design point, the leakage rate was evaluated from CFD simulations, and the results were then analyzed by statistical tools with regression models generated

4.2.1 Computational Model and Parametrization

As one of the most widely used annular pressure seals, labyrinth seals are used to reduce the fluid leakage between different pressure stages. They are multi-toothed seals with circumferential grooves located on the rotor surfaces and/or stator surfaces, which are distributed along the axial direction. The intricacy of the surface geometry and directionality of the seal pattern assist in converting pressure into dissipated kinetic energy without rotor-stator rub effects. The majority of previous studies focused on annular labyrinth liquid seals with smooth rotor/grooved stator (SR/GS) case, whereas this paper

attempts to elucidate the effects of geometric variables modification for smooth stator/grooved rotor (SS/GR) case using CFD and DOE techniques. In this study, a smooth stator/grooved rotor liquid seal was modeled and validated against experimental data. The model was then used as a baseline case for a sensitivity analysis of its geometry variations. Simulation results under different pressures/rotor speeds were used to validate the CFD setup. Four geometric parameters of the seal were then selected as design variables to adapt the baseline geometry for potential performance improvements. The design space was discretized using the DOE technique. Similar mesh/simulation setups were automatically generated for each design point. Regression analysis was applied based on the CFD results for a better understanding of the effects associated with different design variables. These results can be used to improve the current design of smooth stator/grooved rotor annular pressure seals in order to achieve lower leakage rates.

The effects of geometry variations for SS/GR seal were evaluated by the design of experiments technique in this study. In this study, key factors and settings that deliver acceptable performance were identified and presented based on the DOE analysis. The geometrical characteristics selected were studied to find the relative parameter sensitivity for variation of geometry effects

The baseline seal model was selected from an experimental study of SS/GR labyrinth seal available in the literature [71]. The selected geometrical characteristics were modeled to find the relative parameter sensitivity for variation of geometry effects. The baseline model and an example of a design point is shown in Figure 4-18. For constant design parameters, such as the seal length and rotor diameter, the values are listed in Table 4-4.

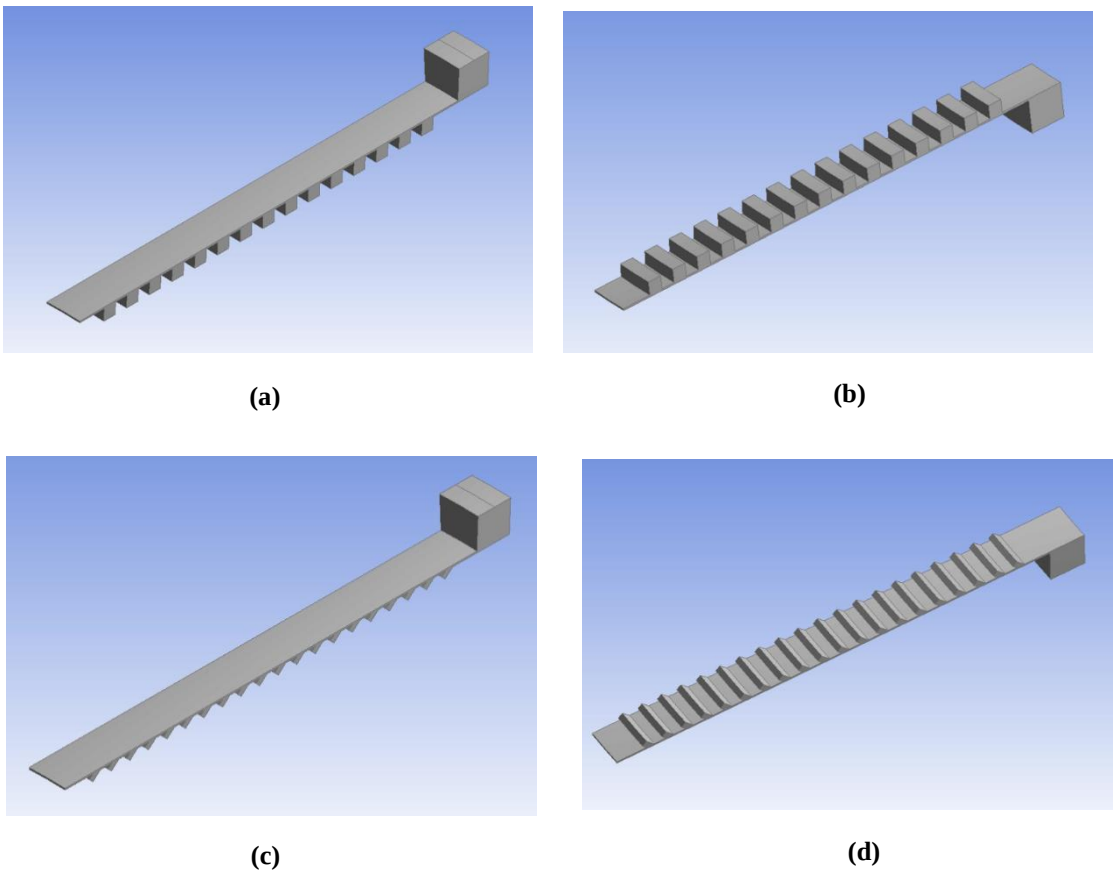

Figure 4-18 Fluid Domain (a) Baseline Model View 1 (b) Baseline Model View 2 (c) Example of a design point View 1 (d) Example of a design point View 2

Table 4-4 Constant Parameters

Parameter	Description	Base Value
Dr	Rotor Diameter	101.8 [mm]
Cr	Radial Clearance of Seal	0.203 [mm]
Ls	Seal Length	50.80 [mm]
Ds	Seal Diameter	101.6 [mm]

The design space considered in this study included 4 design variables. Variations from the design variables changed geometry of the labyrinth seal correspondingly. The design variables included number of grooves, groove height, percentage of area of grooves on rotor surface and the tilt angle of grooves; where the percentage of total groove area on rotor surface determined groove width ($W = Ls \times \beta / N$). By using intermediate design

variables for groove width, the unfeasible designs were eliminated automatically. This study focused on parameter sensitivity, as a result, the variation of the parameter values was distributed as discretized values, which differs from continuous values. The values were set as +50% and -50% of the baseline model, which ensured enough change of the baseline values and remained realistic for manufacturing. In addition, the tilt angle was expected to be a more important design variable and had 5 different discretized values, which are +25%, +50%, -25%, -50% of the 90° baseline model value. Illustration of the design variables is shown in Figure 4-19, and a list of the baseline model values/design variable values are shown in Table 4-5

The full factorial design of DOE study contains $3 \times 3 \times 3 \times 5 = 135$ design points. However, simulating all 135 design points are not necessary. In this study, to reduce the total simulation time, the Kennard-stone algorithm was used to select 60 representative design points for CFD simulation. The Kennard-Stone algorithm is sequential and consists of maximizing the Euclidean distances between the newly selected design points and the ones already selected. As new design point being assigned, distances for each design point that is not selected and the distance to each selected compound was computed. As a result, the distance to the closet design point already selected from the new design point being assigned is maximized. The sample distances in the design space had been normalized before the use of Kennard-Stone algorithm and then converted back to non-dimensionalized values after the design space was generated to facilitate the following CFD simulations.

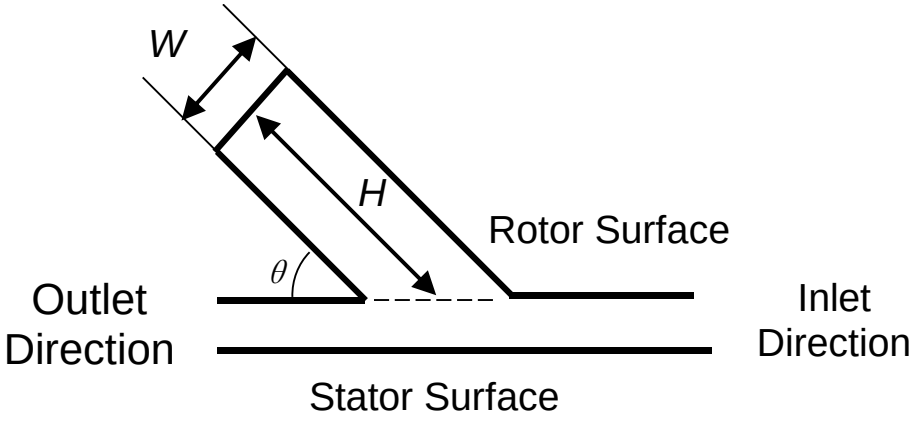

Figure 4-19 Part of Geometry Variables

Table 4-5 Design Variables

Parameter	Description	Base Value	List of Feasible Values
N	Number of grooves	15	10, 15, 20
H	Groove height	1[mm]	1, 1.5, 2 [mm]
β (determines width W)	Percentage of area of grooves on rotor surface	0.5	0.4, 0.5, 0.6
θ	Tilt Angle of grooves	90 [°]	45,67.5,90,112.5,135 [°]

4.2.2 CFD Model and Numerical Analysis

The CFD simulation setup was defined based on previous experimental study, where the detail information are listed in Table 4-6. In addition, only a small 5-degree sector out of 360-degree full model was used in the CFD simulation to reduce the simulation time cost. The periodic rotational symmetry boundary setup was used to connect the boundaries on the two sides. The CFD simulation model was verified by 8 different setups from the literature. The maximum difference from the experimental result was 15%, and the minimum difference was 1.2%. The comparison of four setup to the 2,000 rpm case is shown in Figure 4-20. For the DOE study, the 4.14 bar pressure difference and the 2,000 rpm rotor speed case was used. The baseline model mesh had 296,050 grid elements, and a 5-layers inflation area was applied on both rotor and stator surfaces. A mesh independence study had been performed to ensure the simulation was valid and design points were executed efficiently. In the mesh independence study, reducing the element number in half from the selected mesh resulted in a 7% difference in fluid leakage value, whereas increasing the element number to double the baseline model only made less than 2% difference in fluid leakage, as is shown on Figure 4-21. The number of grid elements was modified by changing the maximum element size in the model and modifying the number of inflation layers. The mesh for each design point changed automatically based

on the parameter values listed in Table 4-5, but followed same general rule. Illustration of mesh for a specific design point is shown in Figure 4-22. The *k*- ω based Shear Stress Transport turbulence model was used in this study since adverse pressure gradients and strong curvature could be observed during CFD simulation. The *k*- ε turbulence model was found easier to converge and has been used to generate an initial solution that was used for the actual simulation. However, the flow separation region, in this case, was not appropriately resolved with the *k*-ε turbulence model. The simulations run with *k*-ε turbulence model had at least 10% difference from the experimental study. The governing equations used in ANSYS CFX were the continuity and momentum equations.

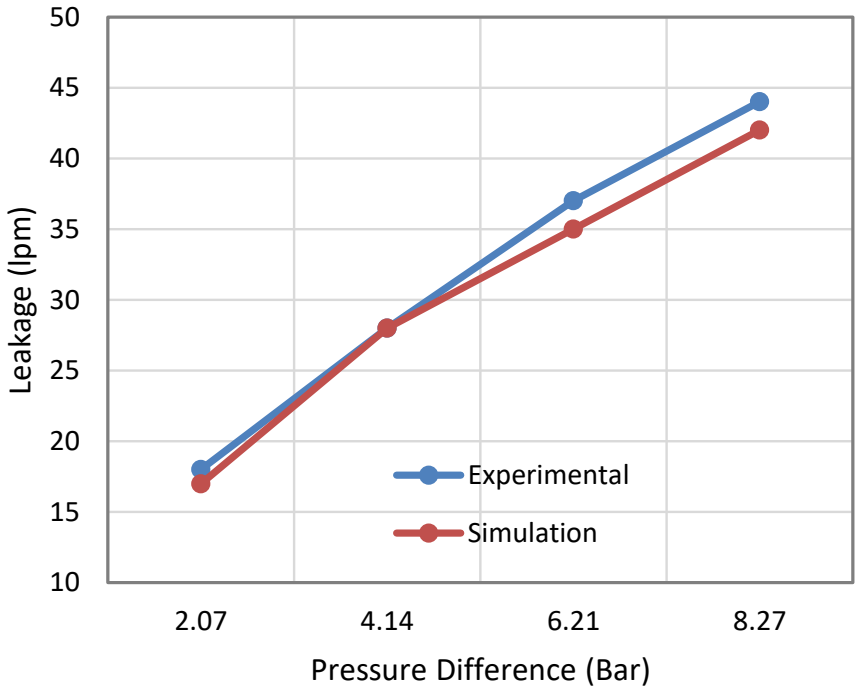

Figure 4-20 Leakage rate comparison between CFD and Experimental measurement

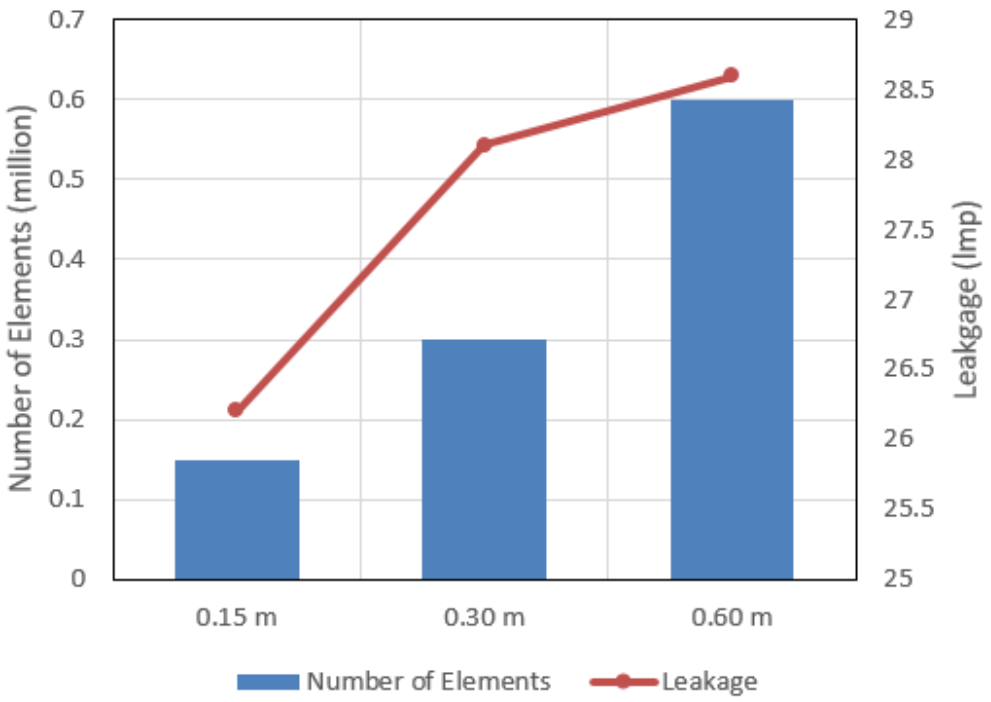

Figure 4-21 Variation of Leakage rate values as seen in Mesh Independence Study

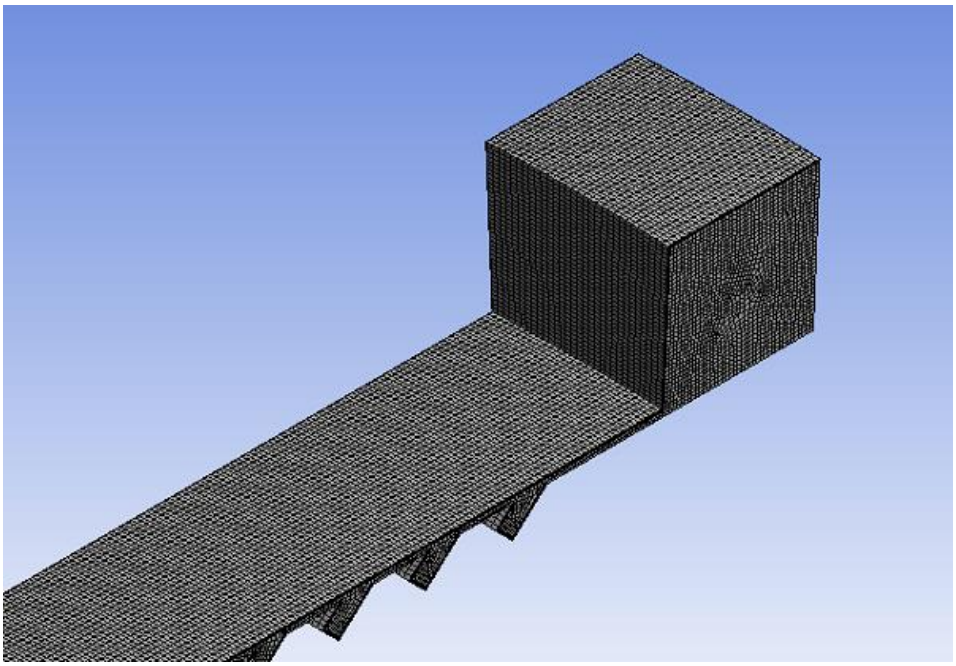

(a)

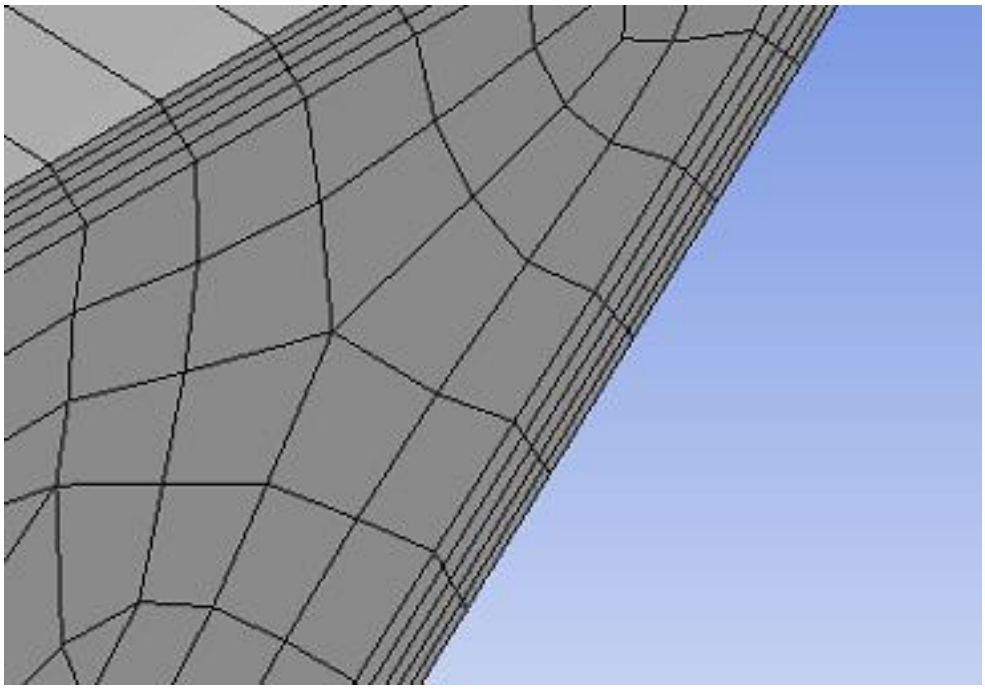

(b)

Figure 4-22 Mesh setup for CFD simulation (a) Overall View (b) Zoom in View

Table 4-6 CFD Setup of SS/GR Labyrinth Seals

Parameter	Value
Rotor Speed	2,000 [rpm]
Pressure Difference	4.14 [MPa]
Working Fluid	ISO VG2 Oil
Heat Transfer	Isothermal
Turbulence Model	SST
Analysis Type	Steady state

4.2.3 Results and Discussion

The leakage rate response was collected directly from CFD output for each design point. Reduced regression models were generated based on the CFD simulation results with the use of backward elimination process. The p-value used in backward elimination process was 0.10.

The regression model of leakage rate for 2000 rpm case is shown in Eqn. 4-1. The values ranges from 0.45 kg/s to 0.49 kg/s. and the R-squared value is 0.86.

$$\begin{aligned} M_L = {} & 0.414 + 6.096 \times 10^{-3} H + 0.065 W + 1.002 \times \theta + 0.0155 HW \\ & + 3.396 \times 10^{-4} H\theta - 9.9151 \times 10^{-4} W\theta \\ & - 6.045 \times 10^{-3} jH^2 - 0.0415 W^2 - 6.209 \times 10^{-6} \theta^2 \\ & + 2.303 \times 10^{-3} H^2 W^2 - 7.044^{-3} HW^2 - 1.801 H\theta^2 \\ & + 6.15 W\theta^2 + 0.0126 W^3 \end{aligned} \qquad \textbf{Eqn. 4-1}$$

The diagnostic figure for the cubic regression model is shown in Figure 4-23. The points closer to the line are the design points more accurately predicted by the regression model. The predicted regression model is generally reflecting the behavior of the actual data. Please note that the cubic regression model does not include design variable *N*, which is the number of grooves along the seal. In actuality, it indicates that for the design variable value range used in this study (10 to 20), the number of grooves had very little effects on the leakage rate response. If the number of grooves was set low enough, such as less than 5 grooves, the leakage rate would definitely decrease. However, for a groove number larger than 10, there were no obvious differences.

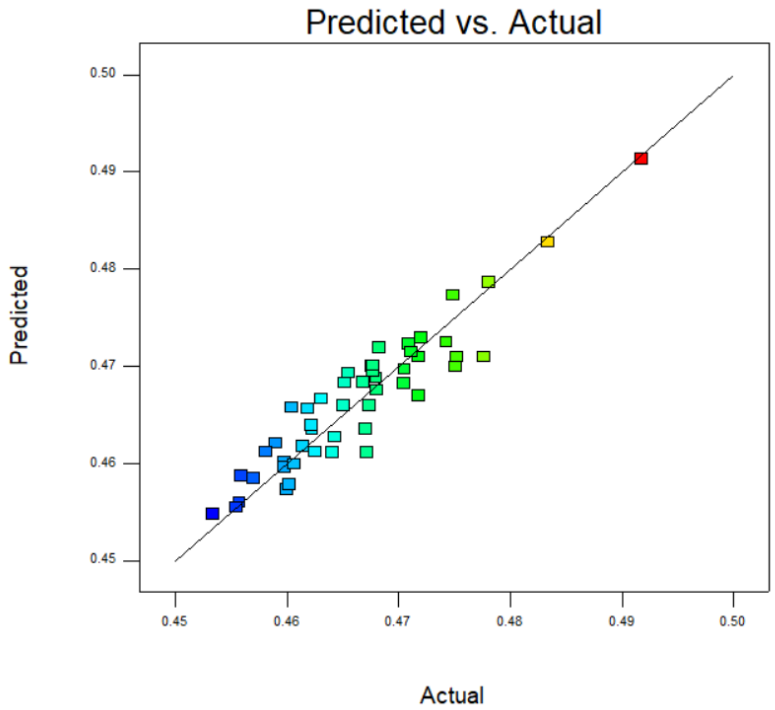

Figure 4-23 Predicted Regression vs. Actual Data

The response surface generated from the regression model is shown in Figure 4-24. The interaction effects in the regression model was from three design variables: groove depth, groove width, and tilt angle, where the number of grooves was not included. From Figure 4-24(a), lower value of groove width would lead to lower leakage rate generally. However, lower leakage rate can be observed on higher value of groove width if the tilt angle is 90 degree, which is the case of groove perpendicular to the rotor surface. Please note that this case is also similar to the baseline model, which implies that the baseline model can be already considered fairly effective to reduce the leakage rate. On the other hand, the tilt angle θ tended to be more complex and related to the leakage rate response. Higher tilt angle generally resulted in a slightly higher leakage rate. In this study, the higher tilt angle (higher than 90 degree) in this model was directed towards the inlet, which suggested a tilt angle direction pointing to the outlet results in lower leakage rate, and can be observed from Figure 4-24(a) and Figure 4-24(b). The response surface shown in Figure 4-24(c) suggests a lower leakage rate at high groove depth and low groove width. However, it is difficult to manufacture since large groove depth would not be realistic on rotor surfaces. Generally, the influence of hole depth is relatively small compared to groove width, and increasing the groove depth does not necessarily have a positive effects to reduce the leakage rate.

In summary, the baseline model itself was already close to the optimized case. The variation of the design variables proposed in this study had relatively small effects on improving the leakage rate.

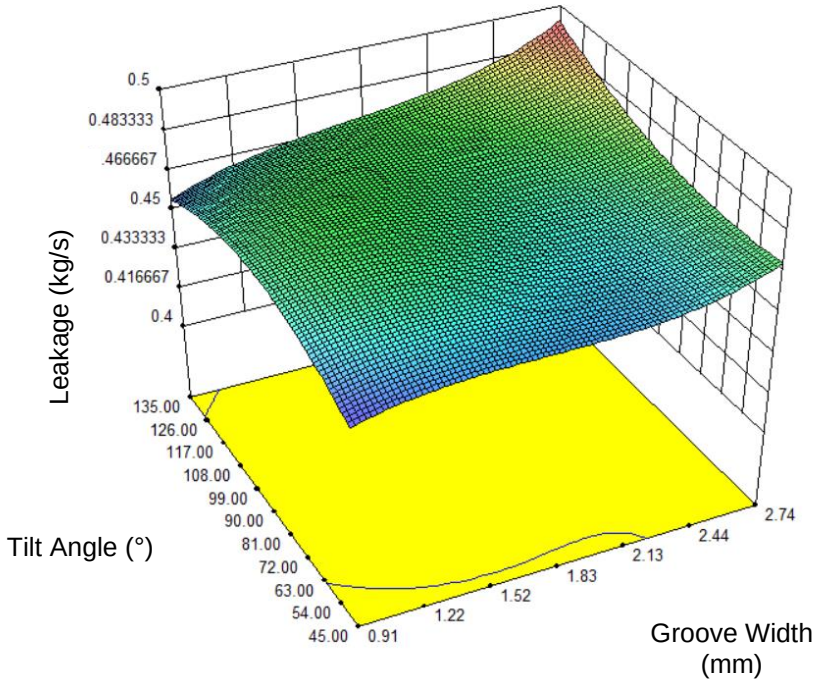
Leakage (kg/s)
0.5
0.483333
.466667
0.45
0.433333
0.416667
0.4
Tilt Angle (°)
135.00
126.00
117.00
108.00
99.00
90.00
81.00
72.00
63.00
54.00
45.00
0.91
1.22
1.52
1.83
2.13
2.44
2.74
Groove Width
(mm)

(a)

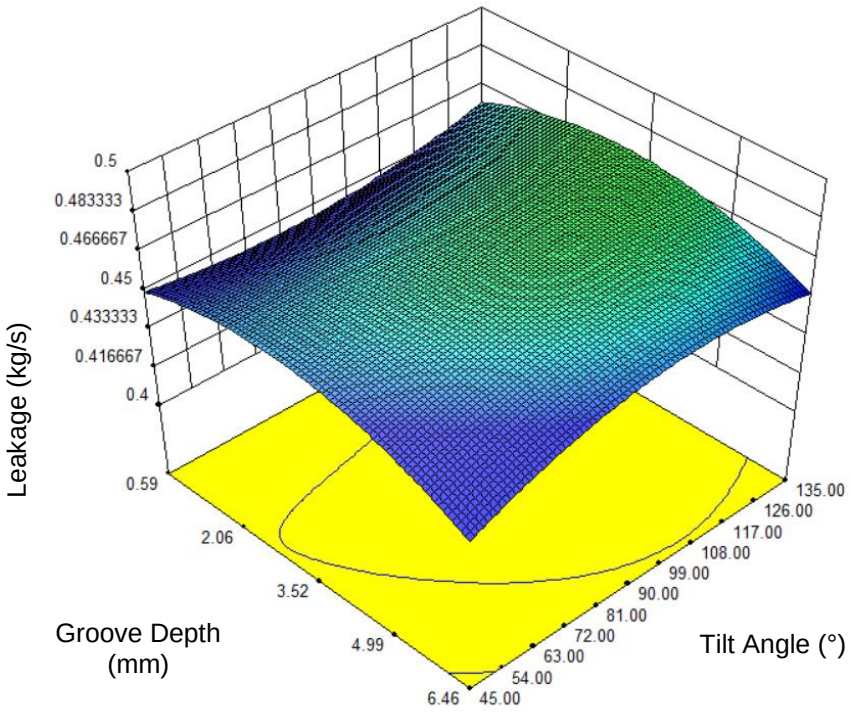
Leakage (kg/s)
0.5
0.483333
0.466667
0.45
0.433333
0.416667
0.4
Groove Depth
(mm)
0.59
2.06
3.52
4.99
6.46
Tilt Angle (°)
135.00
126.00
117.00
108.00
99.00
90.00
81.00
72.00
63.00
54.00
45.00

(a)

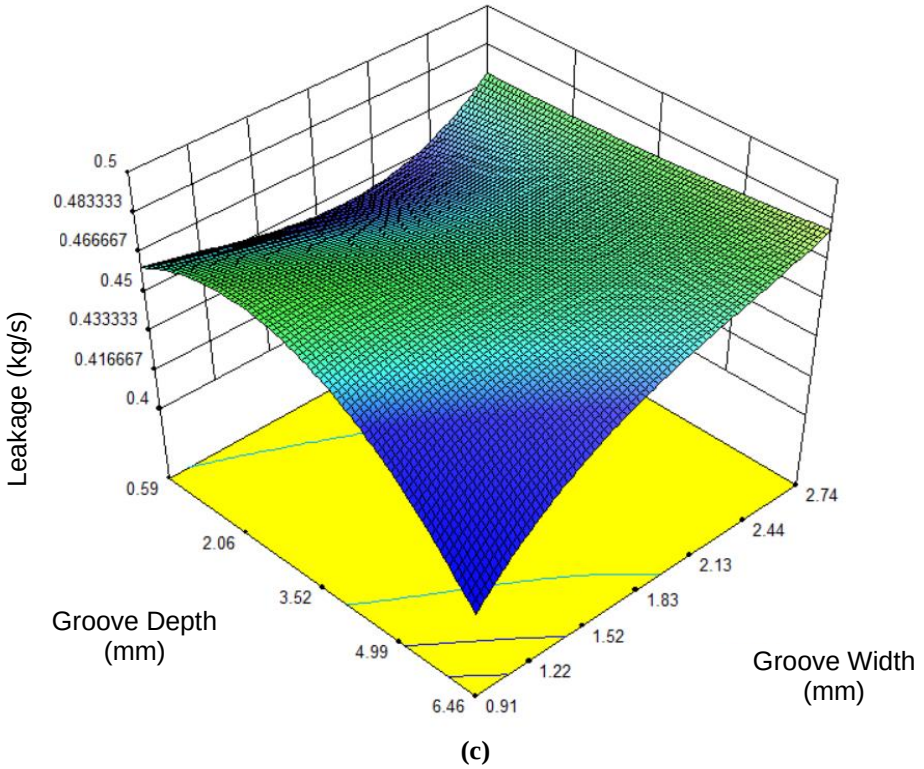

Figure 4-24 Response surfaces - leakage rate (kg/s) – (a)*W* vs. θ (b) θ *vs. H* (c) *H vs. W*

Comparison between a feasible and unfeasible geometry from the leakage rate performance perspective is given in Figure 4-25. For design point No. 19, which model is shown on Figure 4-25(a), the leakage rate is relatively low among all the geometries.

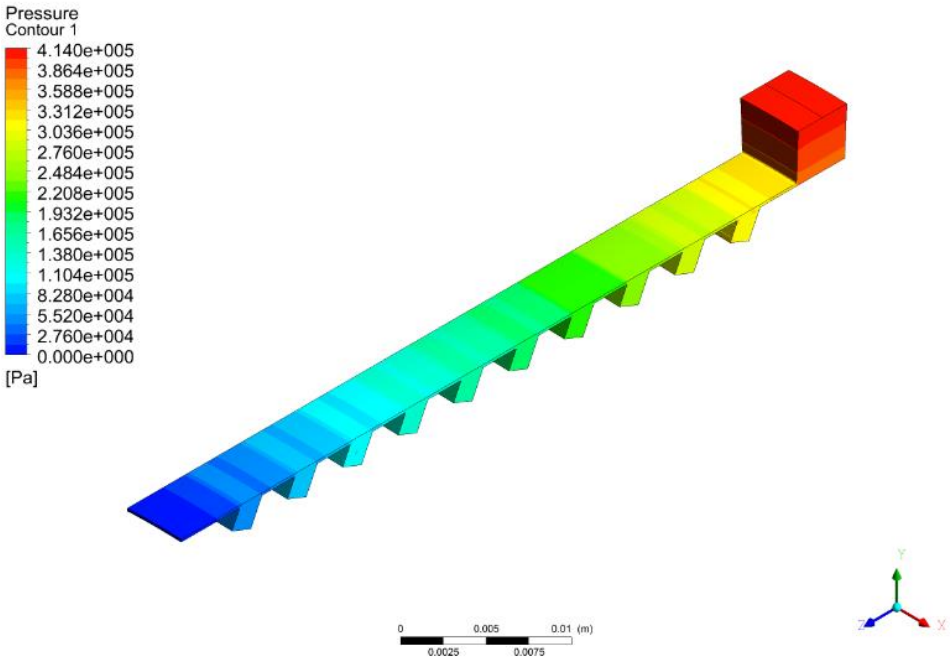

(a)

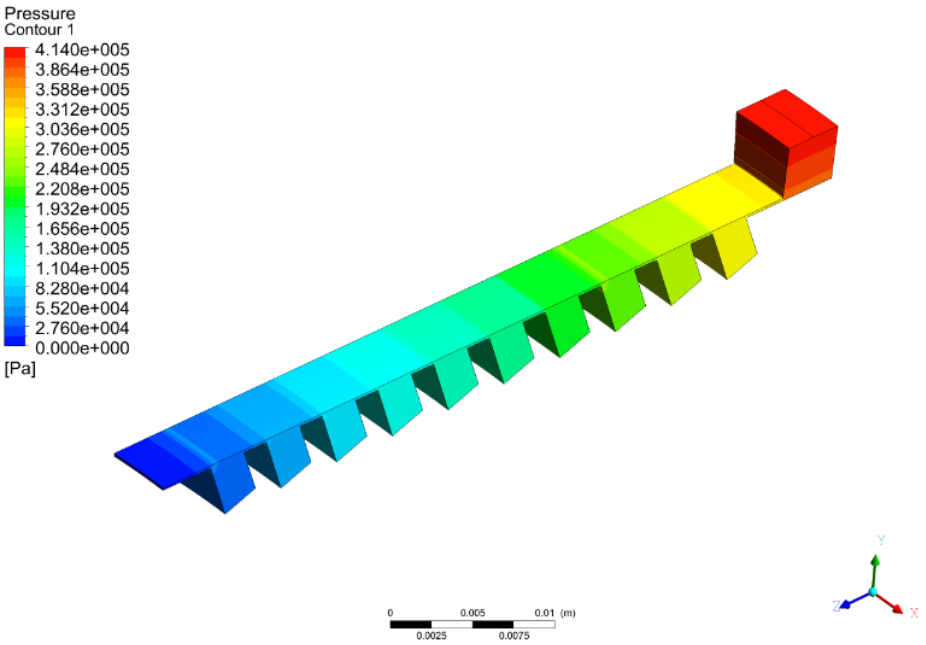

(b)

Figure 4-25 Pressure Plot for Feasible and Unfeasible Geometry Examples (a) feasible, dp19 (b) unfeasible, dp24

One can observe that the groove is tilted towards the outlet, which resulted in a lower leakage rate. The width and depth of grooves are in just moderate level compared to other design points. The geometry of this model suggested that tilting the grooves could potentially improve the performance of the annular pressure seals. On the other hand, the leakage rate was relatively high for design point No. 24, which model is shown in Figure 4-26(b). Groove depth/width for this case were high, and the tilt angle was toward to the inlet, which lowered the effectiveness in reducing the leakage rate. The difference between the two different designs points caused much lower leakage rate in the former one, despite the larger grooves size in the latter one. The streamline plots shown in Figure 4-26 suggested that new vortices could be formed in higher groove depth. The new vortices could potentially store more energy, resulting in lower leakage rates. However, the geometry in design point 24 showed worse leakage rate performance. The energy was lower inside the grooves compared to design point 19, which can be observed based on the slightly different color level in Figure 4-26. The deeper hole/more vortices does not necessarily result in better leakage performance.

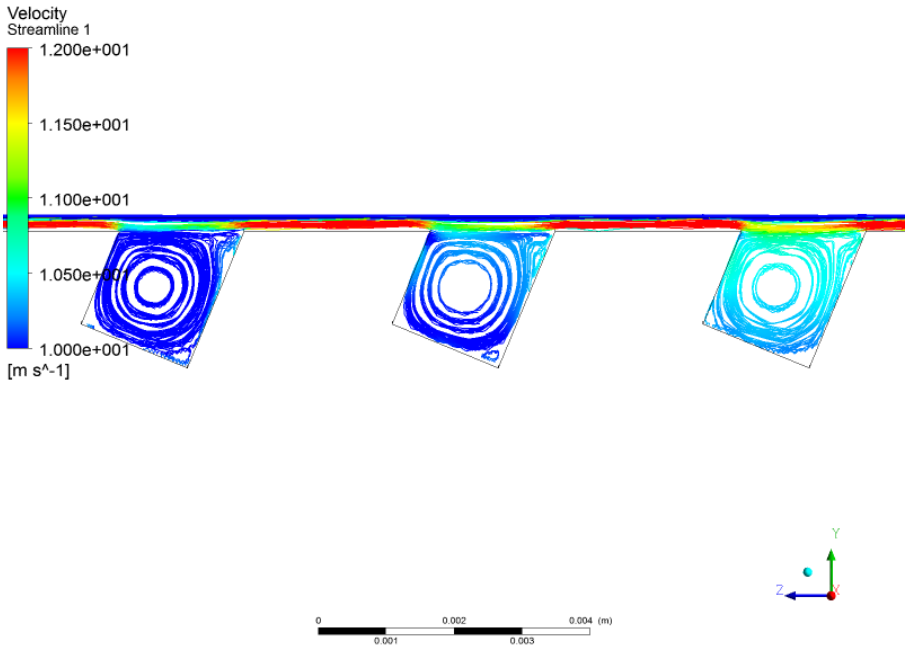

(a)

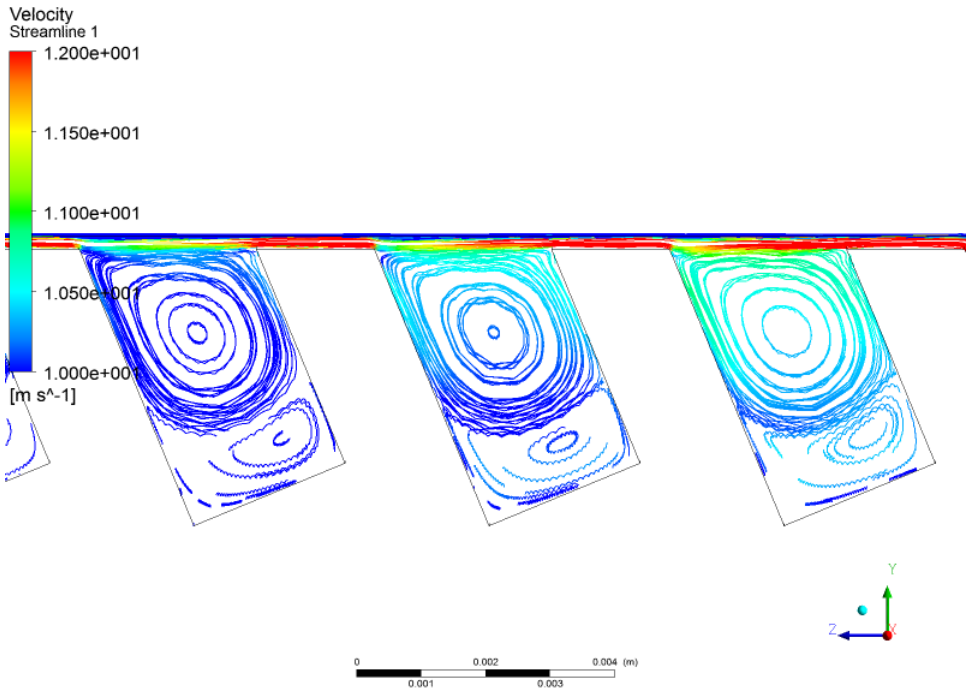

(b)

Figure 4-26 Streamline Plot for Feasible and Unfeasible Geometry Examples (a) feasible, dp19 (b) unfeasible, dp24

In this case study, Smooth Stator/Grooved Rotor labyrinth seals were presented with a parameter sensitivity study using design of experiments technique and CFD simulation. The baseline model results have been compared with the original experimental work from literature for the initial numerical model validation. The leakage rate was illustrated with reduced cubic regression models. Feasible and unfeasible design examples were presented to explain the particulars of pressure distribution.

To predict the leakage performance effects of actual SS/GR seal designs, the regression model given in this paper can be used as a guideline to modify the geometry in an allowed range. In summary, to obtain lower leakage rates, the grooves could be tilted towards the outlet direction on the rotor surface, while the other design points should maintain certain moderate values. The perpendicular default groove setup is acceptable as well from an easier manufacturing point of view. However, with the advent of the 3D-printing

technology and rapid advancements, manufacturing constraints and improved performance requirements can more easily be mitigated.

Chapter 5. Study Related to Annular Pressure Seals

5.1 Energy Decomposition and Flow Field Reconstruction for Hole-Pattern Seals using Reduced Order Model

In noncontact annular seals used in turbomachinery, the leakage flow is reduced by the recirculating flow effects and energy dissipation in the cavities. Therefore, the geometric characteristics of the leakage path play an important role on the sealing performance of annular seals. In order to better understand the mechanism that leads to the leakage of working, this study proposes the utilization of Reduced Order Model (ROM) method and snapshot techniques. The goal of this work is to study the energy distribution of the flow field in sealing components, by replacing a huge number of governing PDEs describing a complex system with only a few ODEs.

A hole-pattern seal was selected for this study and the CFD model was built in ANSYS-CFX. Transient simulations were then performed to calculate the leakage rate and flow field velocity distribution. By using the POD method, the flow field was deconstructed in elementary modes and their corresponding energy levels. In the flow fields of gas sealing components, some highly organized flow patterns were identified. This suggests that some coherent flow structures may exist and that they can be described quantitatively by some lower order modes. These flow structures provide insight into the physics of the internal flow, whereas traditional time and frequency domain approaches only predict the flow field for a specific operating condition. Since the first few modes contained the majority of the energy, the flow field can be accurately reconstructed using these few modes whose flow patterns include most of the information from the original flow field. As full 3D-CFD simulation is a time-consuming method for optimization problems, the method proposed in this study is more practical. It allows construction of the detailed flow field with enough accuracy using only a few modes from the energy composition standpoint, and the energy distribution is focused on the clearance region.

The previous works on hole-pattern mostly connect the leakage rate and rotor dynamic coefficient to the geometry of the grooves directly. However, the analysis of energy

distribution can be used to improve the seal performance by providing insight into the underlying physical mechanisms. This paper focuses on the use of the method of ROM and snapshot techniques to understand the energy distribution of different modes in control volume of working fluid of hole-pattern seals. A huge number of governing PDEs describing a complex system will be replaced with only a few ODEs in the flow field simulation of sealing components. The RPOM methodology used to solve the reduced-order model will be illustrated. The CFD model built in ANSYS-CFX and transient simulations used to obtain the velocity profile will be presented. The computational results and the typical flow pattern will be carried out to discuss the flow field velocity distribution in such hole-pattern seals.

5.1.1 Computational Model

The hole-pattern seal is modeled from Childs and Wade [44], which is identical to the base model of a parameter sensitivity study in Untaroiu and Liu [58]. The grooves on the stator are evenly distributed. The velocity distribution of the air inside the grooves is very difficult to measure with current test equipment. Therefore, the CFD simulation is appropriate to analyze the air velocity distribution. An overview of the fluid domain is presented in Figure 5-1(a). The holes are evenly distributed in both circumferential direction (58×2 = 116 holes) and axial direction (22/23 holes alternately). Note that repeated pattern exist in the model, therefore, 1/58 sector model of whole seal with cyclic periodic boundary condition is used to reduce simulation scale. The sector model is shown in Figure 5-1(b)

The grid convergence study suggested that approximately 1×10^6 number of elements with unstructured mesh are employed. In addition, to better capture the flow characteristics in the clearance region, refinement at rotor surface was used, which is illustrated in Figure 5-2.

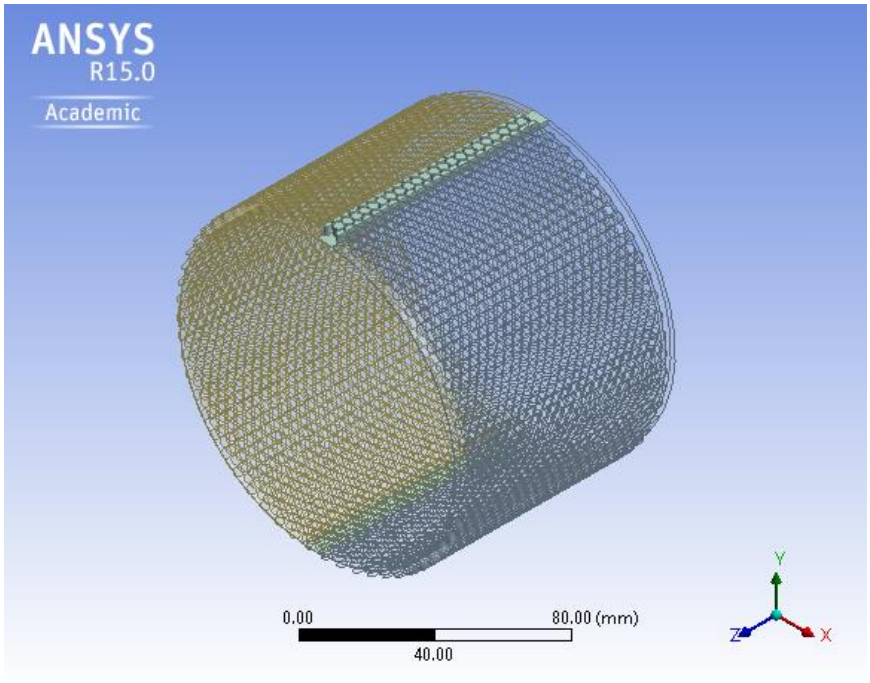

(a)

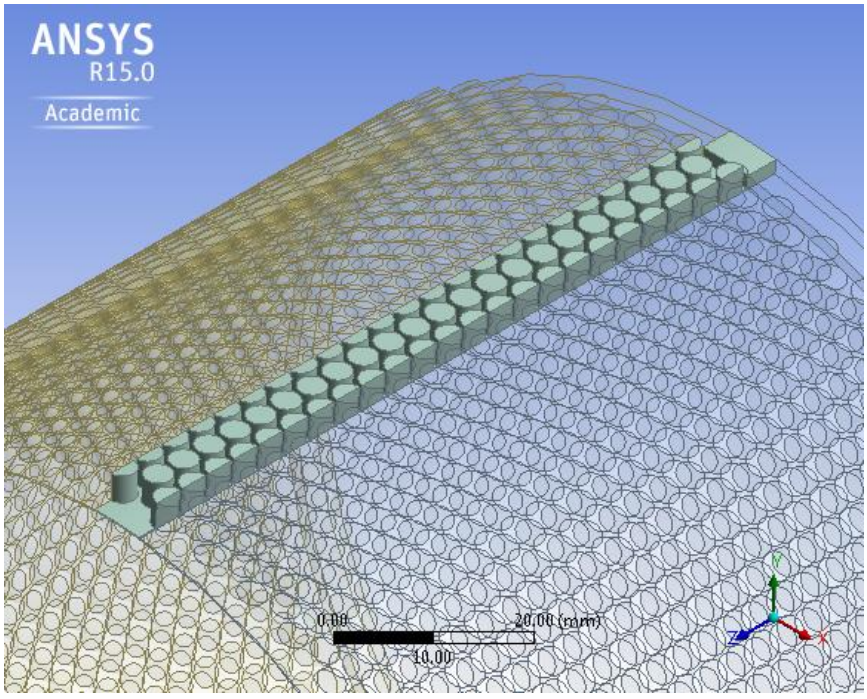

(b)

Figure 5-1 Fluid Domain of the Selected Hole-Pattern Seal Geometry. (a) Overview of the Fluid Domain. (b) Zoom in View of the 1/58 Sector Model

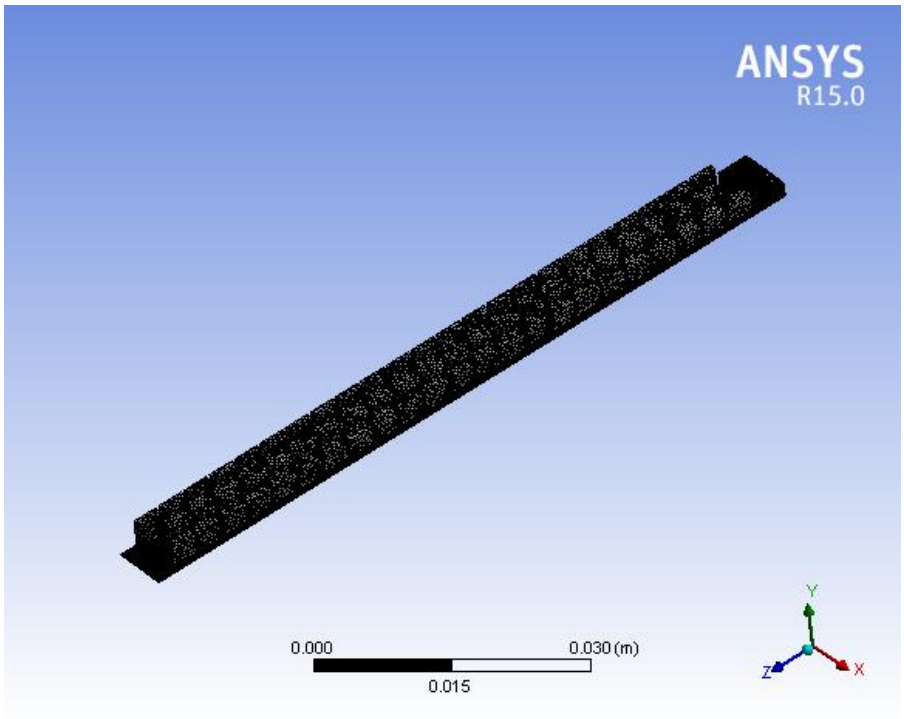

(a)

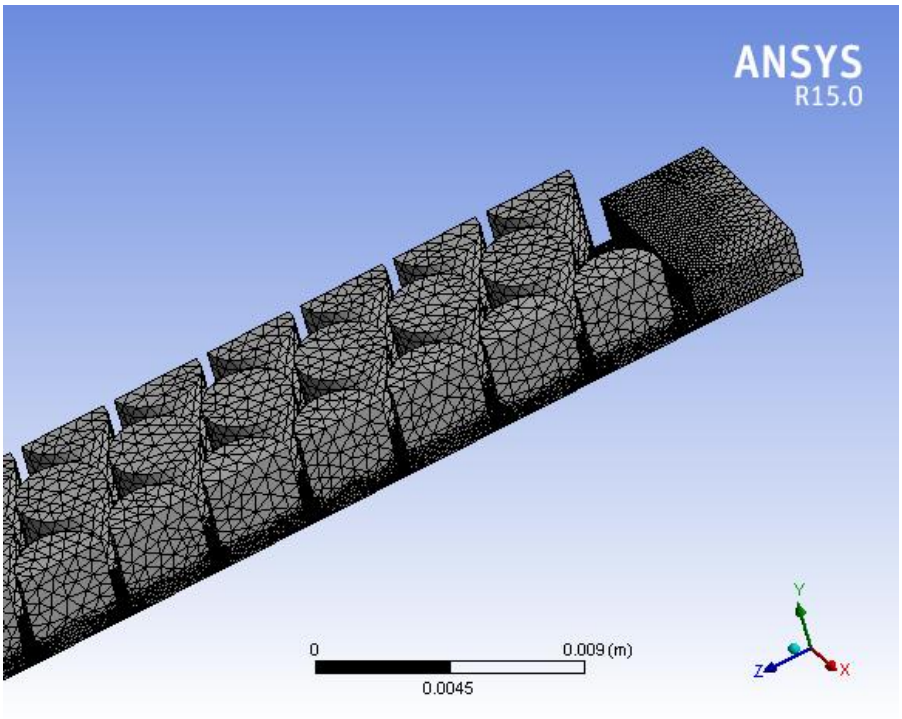

(b)

Figure 5-2 Mesh of the 1/58 Sector Model. (a) Overview of the 1/58 Sector Mesh. (b) Mesh of the Grooves

The CFD simulation is performed by ANSYS CFX package. The transient flow simulation is performed based on a previous steady state flow study. The rotational speed of the rotor is set to high angular velocity with perturbation of 1/400 of the velocity (n= (20200 + 50.5sin$2\pi ft$) rpm). The perturbation frequency f is power supply frequency 60 Hz. In each cycle, 100 time steps are used for accurate POD snapshot. The sampling frequency is therefore 6,000 Hz. The pressure at the inlet is set as 70 bar, and the pressure ratio between outlet and inlet is 0.45. The turbulence model in the domain is k-ε in conjunction with a scalable wall function. Isothermal heat transfer is used with 17.4 C gas temperature. The CFX-Pre figure is shown in Figure 5-3.

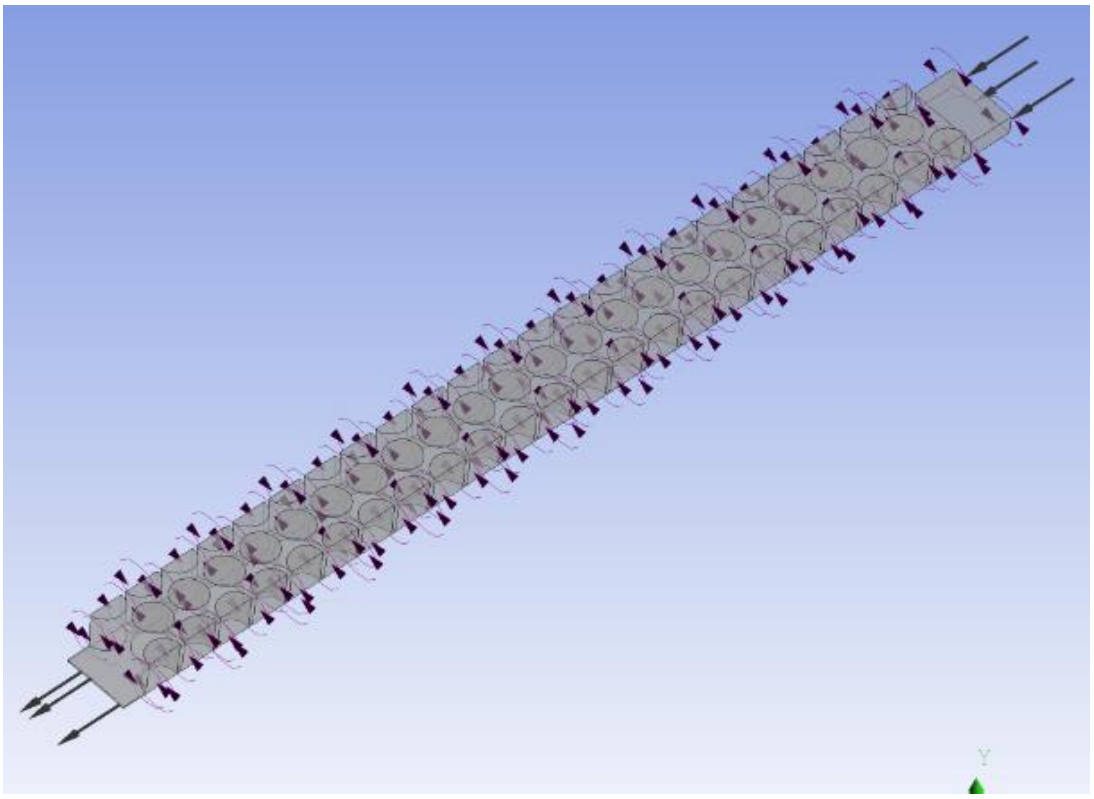

Figure 5-3 CFD Model and Boundary Conditions

5.1.2 Results and Discussion

The leakage rate of the steady state simulation result was verified using Untaroiu et al.[58], where the experimental leakage rate is 0.409 kg/s, 4.3% error to the CFD result (0.392 kg/s). The steady state solutions are used as initial condition for transient simulation, which ensured the accuracy of the transient solutions. Velocity profile data is extracted from each

of the 22 grooves along the axial direction of the seal in CFX-Post. These grooves are numbered by their distance to the inlet, from 1st to 22nd. These computational results of velocity field are used for POD analysis. To understand the flow pattern in the annual seal, five representative grooves (groove 1, 5, 10, 15, 22, shown in Figure 5-4) are analyzed with individual POD basis functions of velocities and their combination. The plane normal is in the Z direction, consequently only x and y components of velocity directions are plotted.

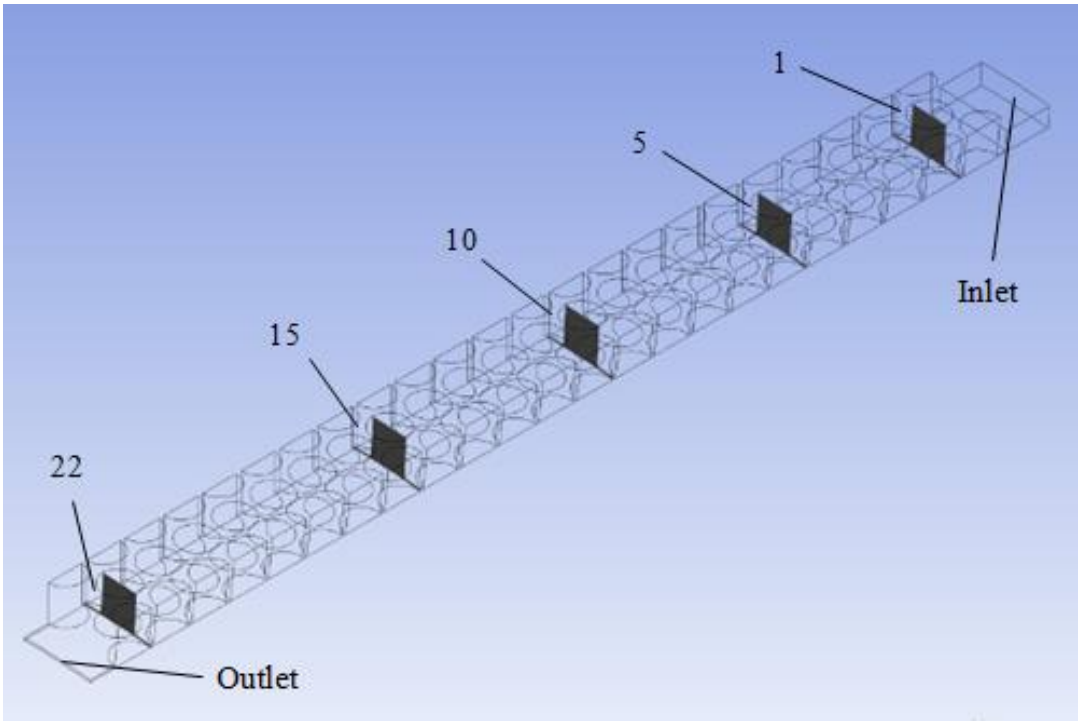

Figure 5-4 Five Representative Grooves Location

The flow patterns are presented with several different views in Figure 5-5 for the whole section of groove 1. For the overall plot of 100 modes (Φ1~Φ100), the flow is significantly concentrated in the clearance region near rotor surface. Correspondingly, the velocity components inside the groove are much less than that. A vector plot from CFX-Post is shown to be consistent with the POD results, where the velocity magnitude near the rotor surface is much higher. This is easy to observe from the vector plot. In the first mode figure, velocity distribution is similar to the case Φ1~Φ100, which implies that the first mode velocity is dominating. In the second mode figure, vortices evidently become more clear,

which shows relatively complicated flow pattern. The velocity concentration reduced in the clearance region, especially near the rotor surface at the bottom side of the groove. The velocity magnitude further averaged among the whole section in the third mode. Nonetheless, the flow concentration is still higher in the clearance region near rotor surface. The flow pattern of the third mode is even more complicated, but mode 1~3 is nearly same as mode 1 only.

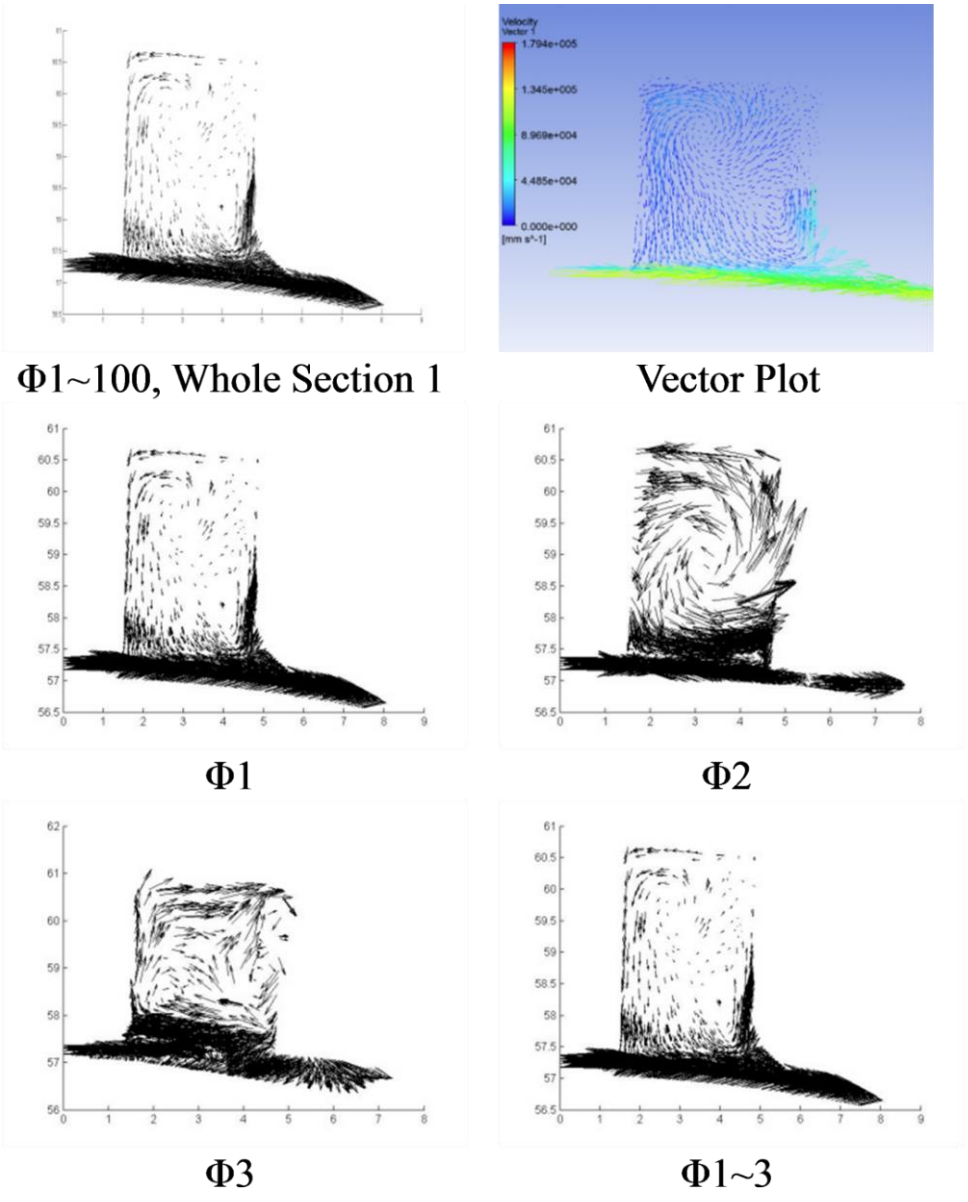

Figure 5-5 Flow Pattern for the First Three Modes in Whole Section 1

The flow patterns for the other sections are presented in Figure 5-6. The flow pattern characteristics are similar to section 1. Velocity concentration is much higher near the rotor surface. The velocity components are pointing outside in radial direction and follow the rotor rotational direction. For the other modes, the velocity magnitude concentration reduces as the mode number increases, while the velocity magnitudes are still higher in the clearance region near rotor surface. Therefore, the energy is still concentrated in the clearance region. The flow pattern in the other modes are more complicated but are not as important as the first mode, which is the same as section 1. Only the overall plot of 100 modes and vector plot from CFX-Post are shown. Vector plots from ANSYS-CFX post also show agreement with the POD plots.

The detail of the energy flow in all modes for the whole section is shown in Figure 5-7. The energy mostly exists in the first mode, which correspond to the fact that the flow pattern is dominated by the flow pattern of the first mode. An interesting phenomenon can be observed from the plots, as we move further away from the boundaries (inlet and outlet), the energy decays slower as the mode number increases. The section 1 and section 22 decay fastest as they are most closer to the boundaries, and section 10 decays the slowest being located in the middle on the axial direction of the domain. This effect may come from the influence of the boundary conditions

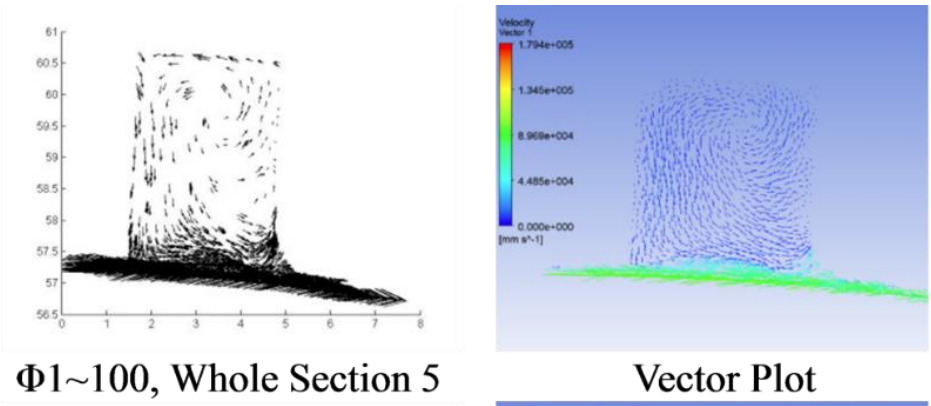

Figure 5-6 Flow Pattern in Whole Section 5, 10, 15, 22

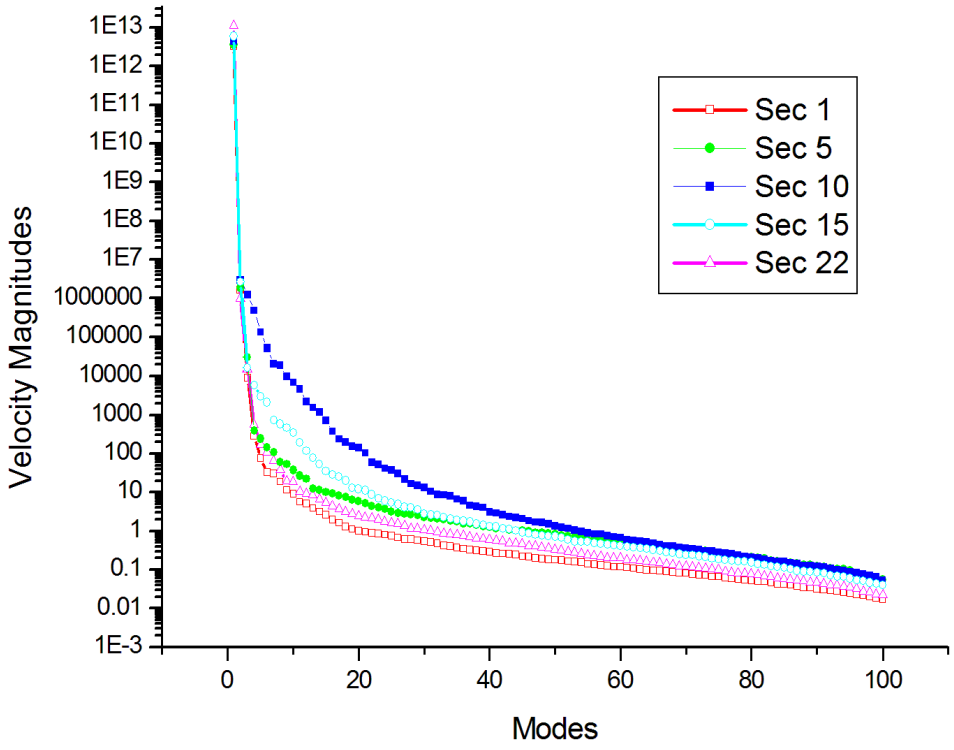

Figure 5-7 Velocity Magnitude (Energy) Plot for all Modes in Whole Section

The flow patterns inside the groove are similar to the flow pattern in the whole section, thus, only groove 1 and groove 10 are presented in Figure 5-8. Even if the clearance regions near the rotor surface are removed, the velocity magnitude and energy concentration can still be shown at the bottom side of the grooves, which is the closest region to the rotor surface.

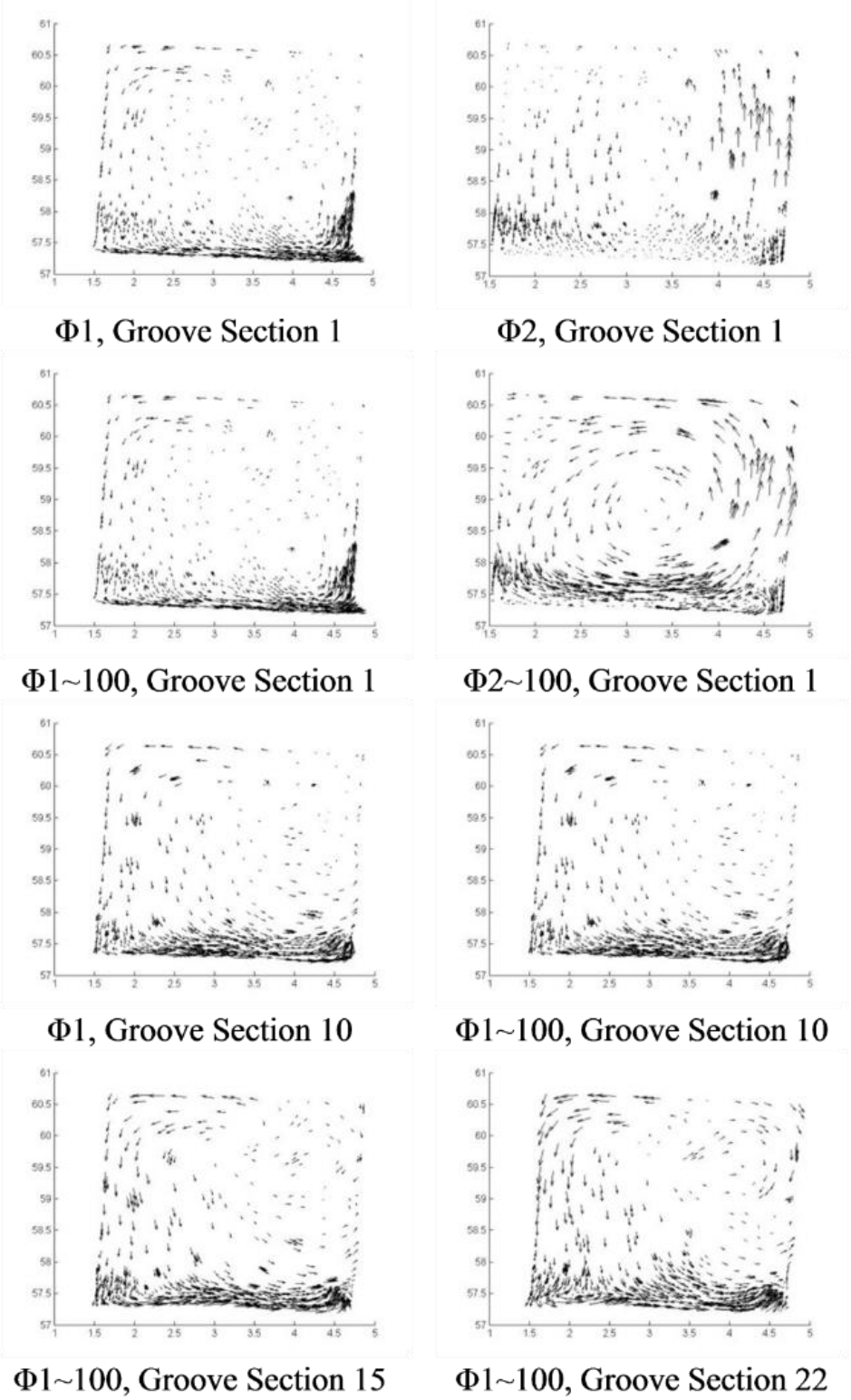

Figure 5-8 Flow Pattern in Groove Section 1 and 10

The detail of the energy for all modes inside the groove is shown in Figure 5-9. Nearly the same phenomena can be observed from the plots. The energy in the first mode is much higher than the energy in the other modes. The energy decay in section 1 and section 22 are faster than those in section 5 and section 15. The energy in section 10 decays even slower than section 5 and section 15.

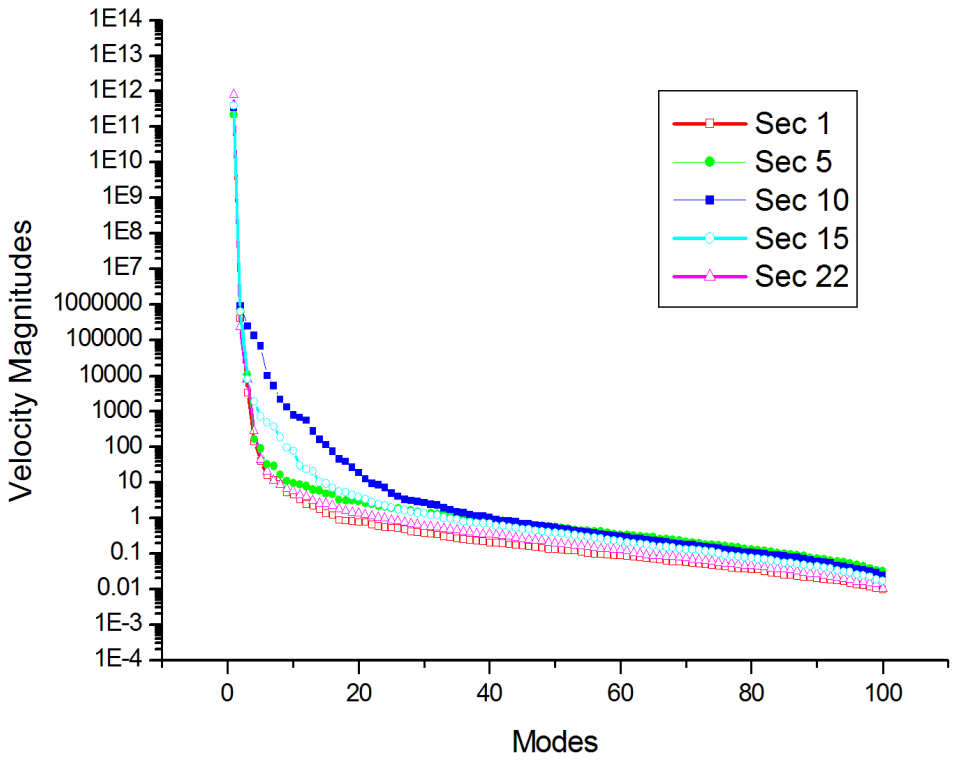

Figure 5-9 Velocity Magnitude (Energy) Plot for all Modes in Groove Section

The first mode velocity magnitude of each section is presented in Figure 5-10 for both whole and groove sections. The velocity magnitude for the groove section is in the range of 3×10^{12} to 2×10^{13}. The velocity magnitude for the groove section is in the range of 1×10^{11} to 9×10^{11}. Compared to the energy in the whole section, the energy in the groove is much lower. Thus, the energy is concentrated in the clearance region near rotor surface. The first mode energy distribution inside the grooves does not show the same tendency to the whole section from Fig. 10, this may be result from strictly geometric cut of the groove section at

the radius of the clearance region while the energy on the bottom of the grooves may not be evenly distributed in each groove.

Streamline profiles from CFX-Post along the axial direction are presented in Figure 5-11. The corresponding velocity magnitude plot for these streamlines is shown in Figure 5-12. Despite the interference velocity magnitude near the inlet, the velocity profile of the clearance region (higher value in the plot) is approximately same as the velocity magnitude plot (velocity magnitude profile in whole section is similar to that in clearance region) is presented in Figure 5-10(a); the velocity profile of the groove region (lower value in the plot) is approximately same as the velocity magnitude plot shown in Figure 5-10(b). The two results from different source match each other very well.

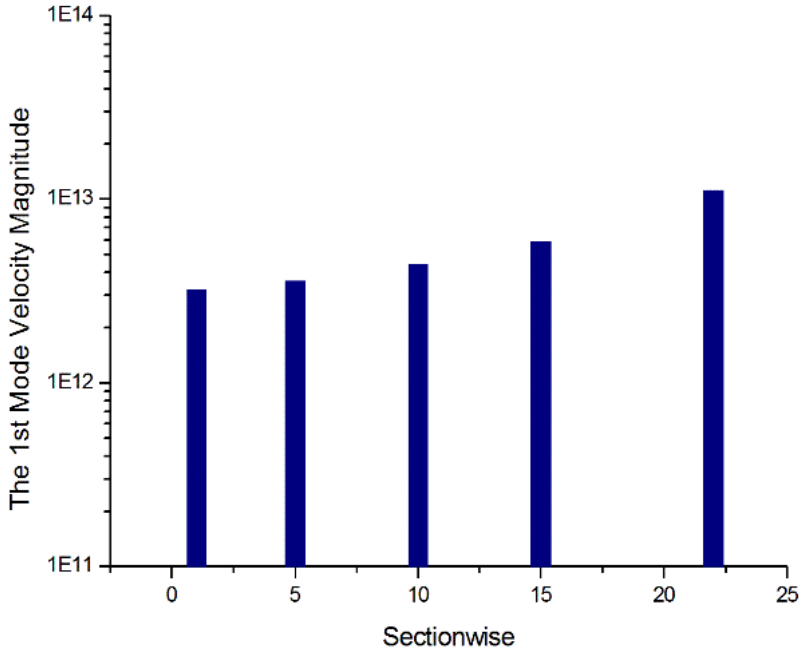

(a)

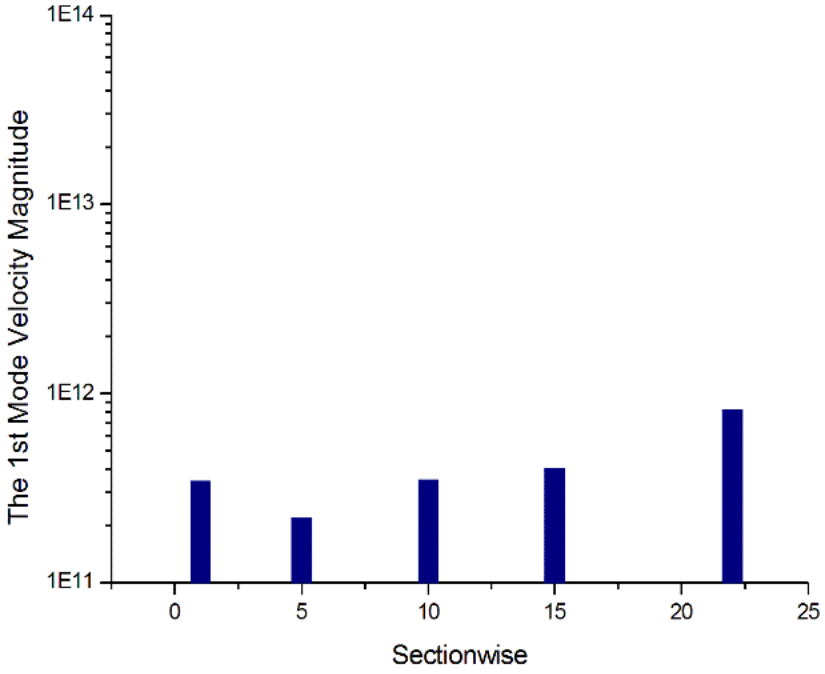

(b)

Figure 5-10 Velocity Magnitude (Energy) Plot along Axial Direction for: (a) Whole Section (b) Groove Section

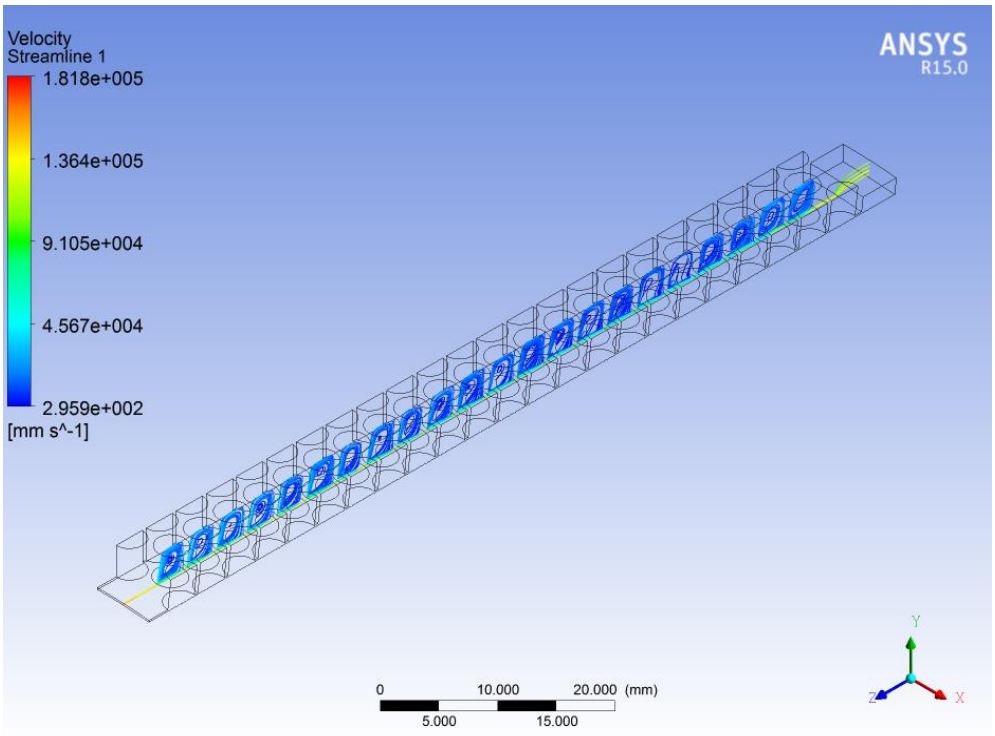

(a)

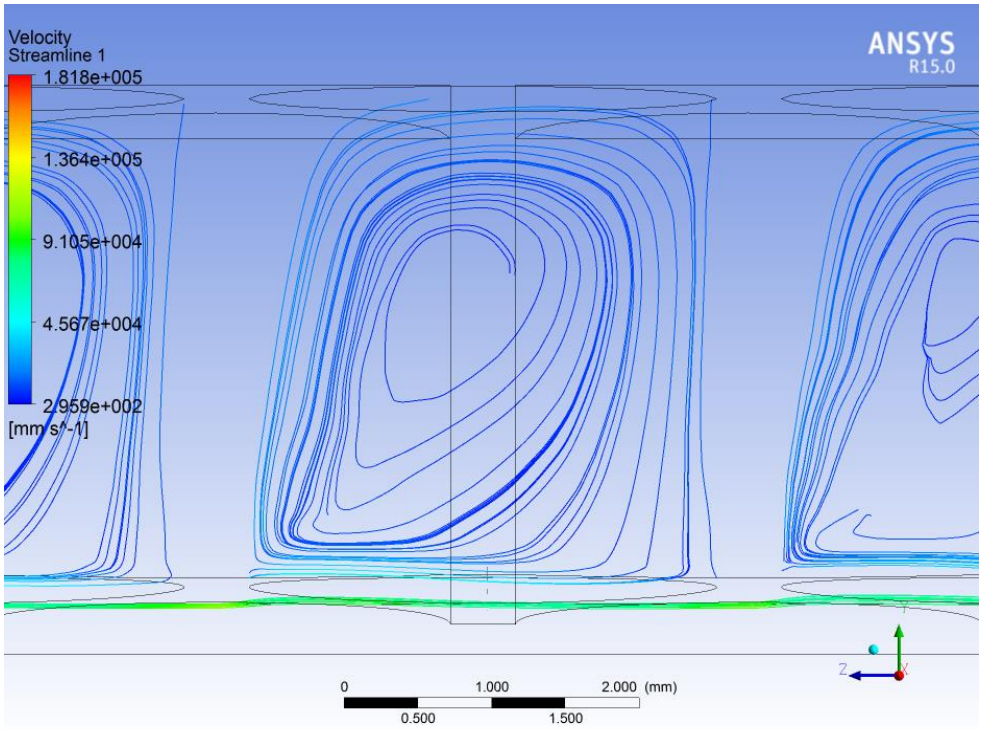

(a)

Figure 5-11 Streamline Profile along the Axial Direction for (a) Overview of the Sector (b) Zoom in View for One Groove

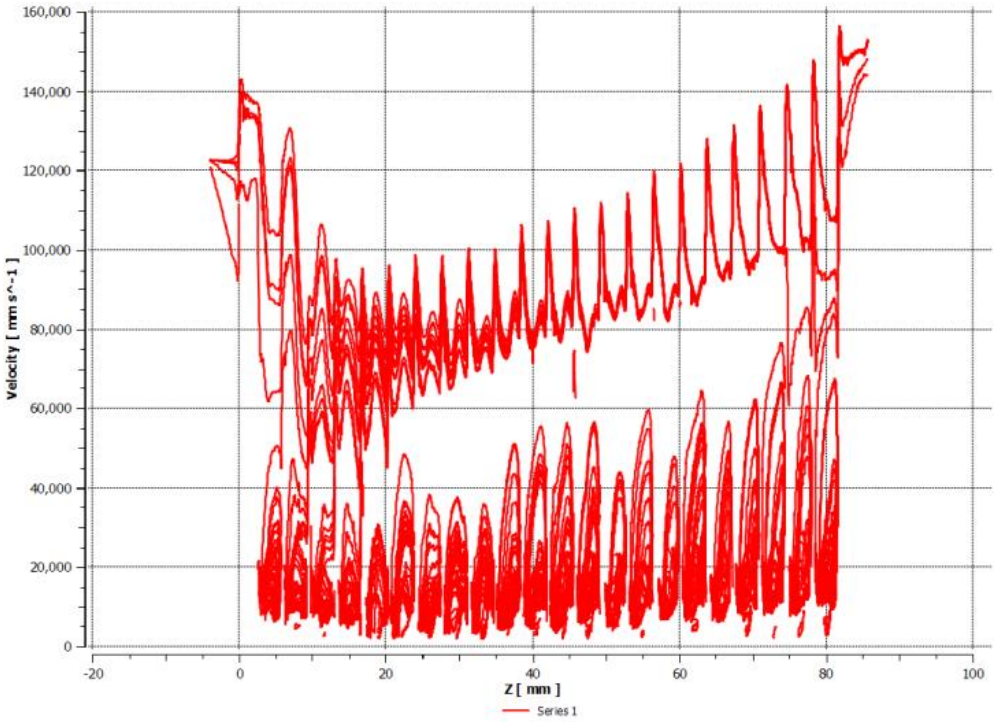

Figure 5-12 Velocity Magnitude Plot of the Streamline Profile

The flow field in hole-pattern seals can be precisely reconstructed from energy decomposition by POD snapshots technique. The details of the velocity profile inside the grooves are illustrated accurately from the relative energy of elementary modes. The first few modes contain the majority of the energy, so only these first few modes are needed to recreate the flow field.

The energy distribution is focused on the clearance region. The groove depth is not efficiently used as the energy only concentrated near the rotor surface area.

Considering that the current hole-pattern seal design is not efficiently using the space deep inside the groove, a potential improvement from the energy flow point of view can be carried out. The geometry could be adjusted to let energy flow more easily into the inner space of grooves. This potentially can be achieved by tilting the groove orientation away from the normal of rotor surface.

5.2 Comparison of 2D and 3D Reduced-Order Modeling for Labyrinth Seals

A specific shape of leakage path is formed by defining geometry of the stator surfaces and rotor surfaces. Thus, the flow rate is minimized from isobaric energy dissipation in the seal cavities through the convoluted path dependent on geometry of the stator and the rotor surfaces. To further understand the phenomenon behind the fluid leakage reduction process, a realistic model must be employed to capture the characteristics of the flow field. Traditional method to develop such a model is based on utilization of conservation laws, which introduce governing equations consisting of significantly coupled large systems of partial differential equations (PDEs).

These high dimension PDEs are hardly solvable by analytical methods. Instead, numerical methods are commonly used to solve these equations. One of the difficulties to optimizing labyrinth seal geometry design is the huge time consumption of doing the CFD simulations.

The CFD simulations have to be performed under very high angular velocity condition. The solutions take very long time to converge in some of the cases. The previous works on optimization of labyrinth seals mostly used design of experiments technique based on CFD simulations. At least 5 to 10 CFD simulations have to be performed to fully analyze the impact of a specific geometry parameter. Another limitation appears when three or more geometry parameters affect each other simultaneously. It is hard to identify the connection due to the complexity of the flow in non-contact annular seals that includes intense vorticity.

5.2.1 Computational Model

The seal geometry computational model to obtain the observations to form the data set used in proper-orthogonal decomposition for this study was selected from literature [63, 72, 73]. The specific dimensions of the numerical model are selected from related experimental work. The CFD simulation is appropriate to obtain the fluid velocity observation since it is very difficult to measure the velocity distribution experimentally. An overview of the fluid domain is presented in Fig. 1(a). There are 20 labyrinth grooves evenly distributed along the axial direction. The seal is 267 mm in length. The seal rotor diameter is 111.9 mm with a radial clearance in the jet flow region of 0.0305 mm. The diameters of alternating grooves are 3.75 mm and 4.25 mm, which are arranged as a repeated pattern as three smaller grooves followed by two bigger grooves. There is a 9.53 mm space between the inlet to the seal jet flow region and the first row of holes. The full 360° model of the seal can be seen in Figure 5-13(a). Since there is obvious repeated pattern along circumferential direction, periodic boundary condition is used to reduce computational time by choosing 1/72 of the 360° model. The upstream region of the seal, as shown in Figure 5-13(b), is incorporated in the computational domain. As a result, the flow preswirl at the inlet of the seal was generated naturally to better simulate the upstream flow.

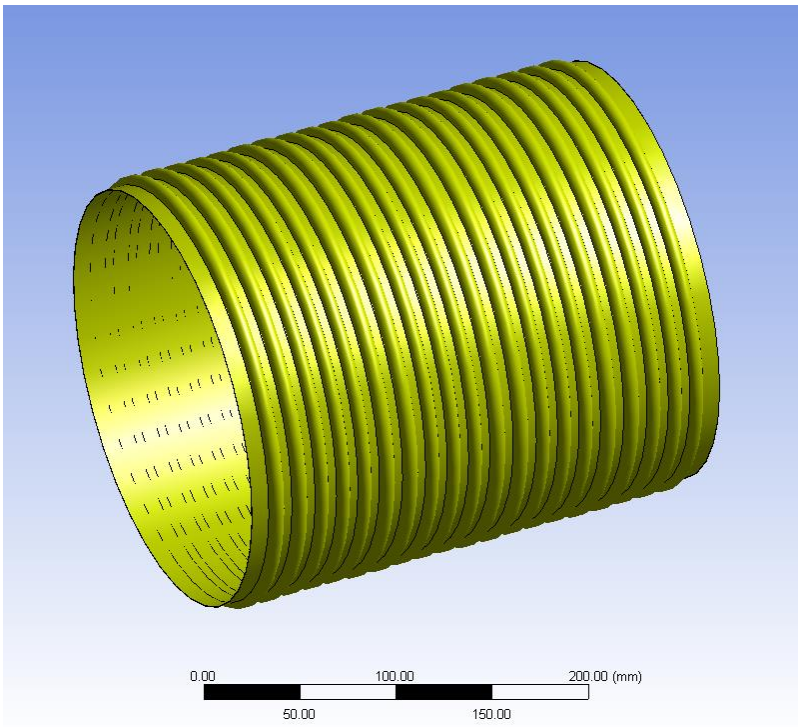

(a)

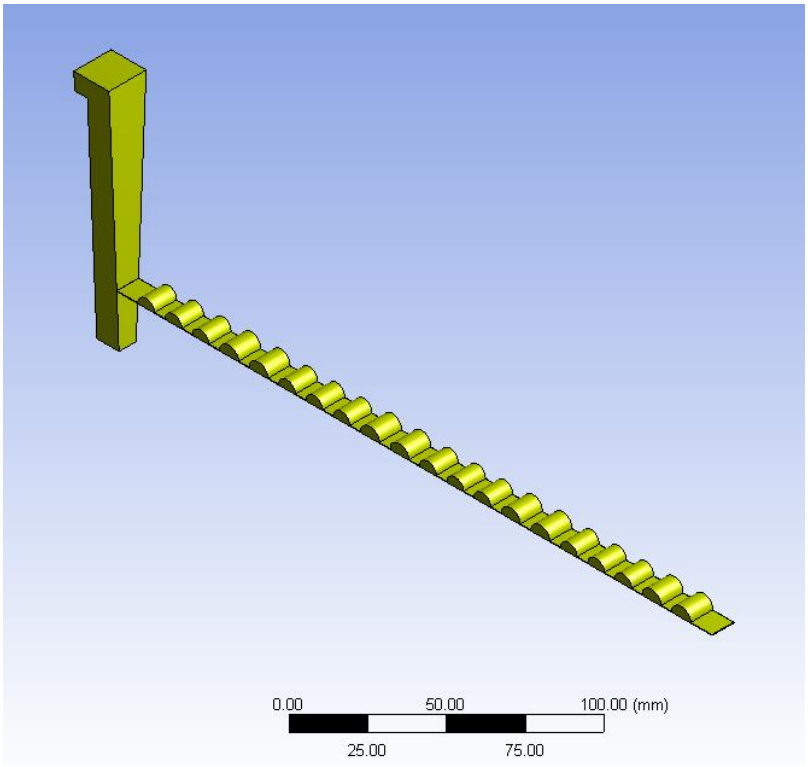

(b)

Figure 5-13 The Labyrinth Seal (A) 360° Model of the Fluid Domain. (B) 1/72 Sector Model

A mesh independence study is performed to determine an optimal number of grid elements. As a result, considering both computational efficiency and accuracy of the solution, a structured mesh with approximately 570,000 grid elements is selected for this study. The corresponding CFD results are found to be comparable to those reported in the literature for the identical seal model [66, 74]. Inflation layers are included along the stator and rotor surfaces to refine the mesh near the solid surfaces and capture the details of the boundary layer. The details of the mesh are illustrated in Figure 5-14.

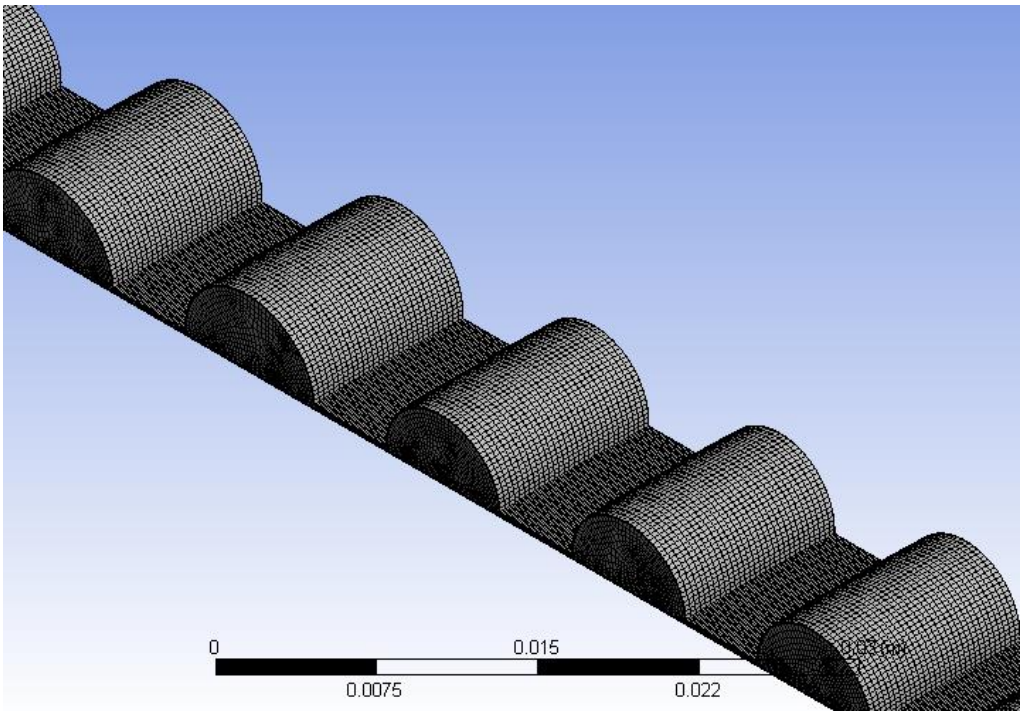

(a)

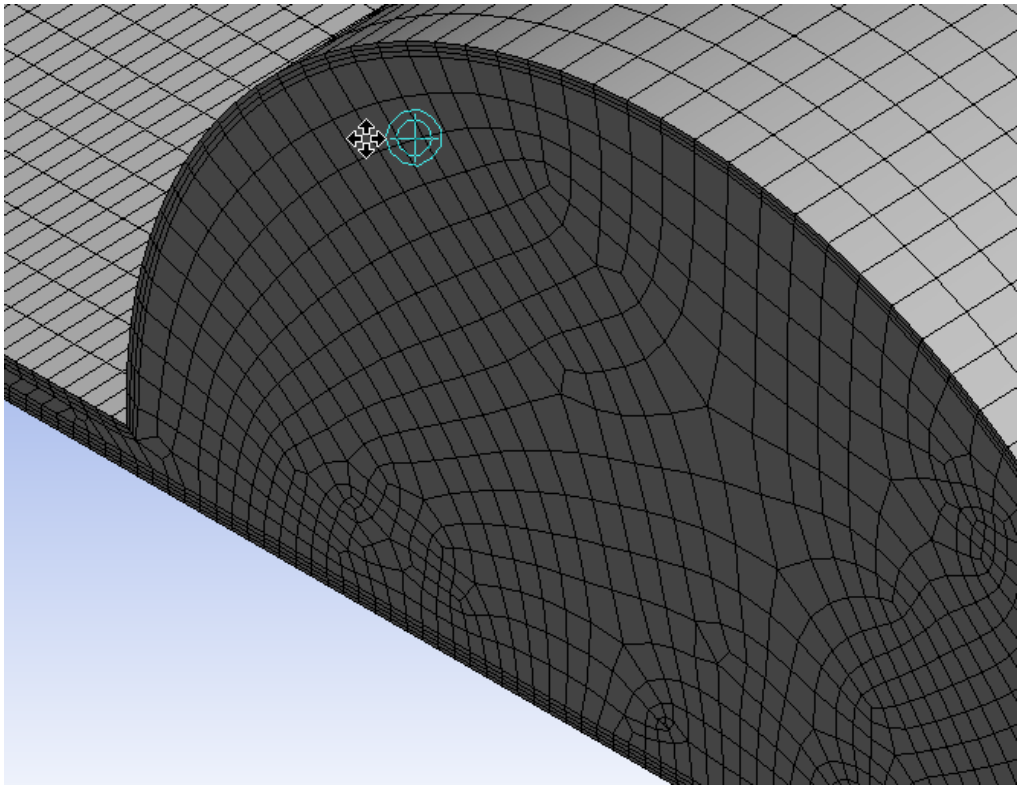

(b)

Figure 5-14 Mesh of CFD Model for the 1/72 Sector. (A) Grid Distribution (B) Detail View

The transient flow simulations are performed based on a converged steady-state simulation result. The shaft rotational speed is set to 20,200 rpm with a 5% perturbation around that value. As a result, the actual velocity used in the transient simulation is n = 20,200 + 1010·sin2πft rpm. The perturbation frequency f is the standard power supply frequency, which is 60 Hz. Six hundred time steps are used in one cycle, with data recorded every 10 time steps. This results in 60 observations per cycle to be used as input data for the proper-orthogonal decomposition. The sampling frequency is therefore 3,600 Hz. The pressure at the outlet is set to 1 atm and the pressure at the inlet of the computational model is 18.757 MPa. The turbulence model in the domain is k-ε set in conjunction with a scalable wall function. Isothermal heat transfer is used and gas temperature is set to 25 °C. The model and the boundary conditions are shown in Figure 5-15.

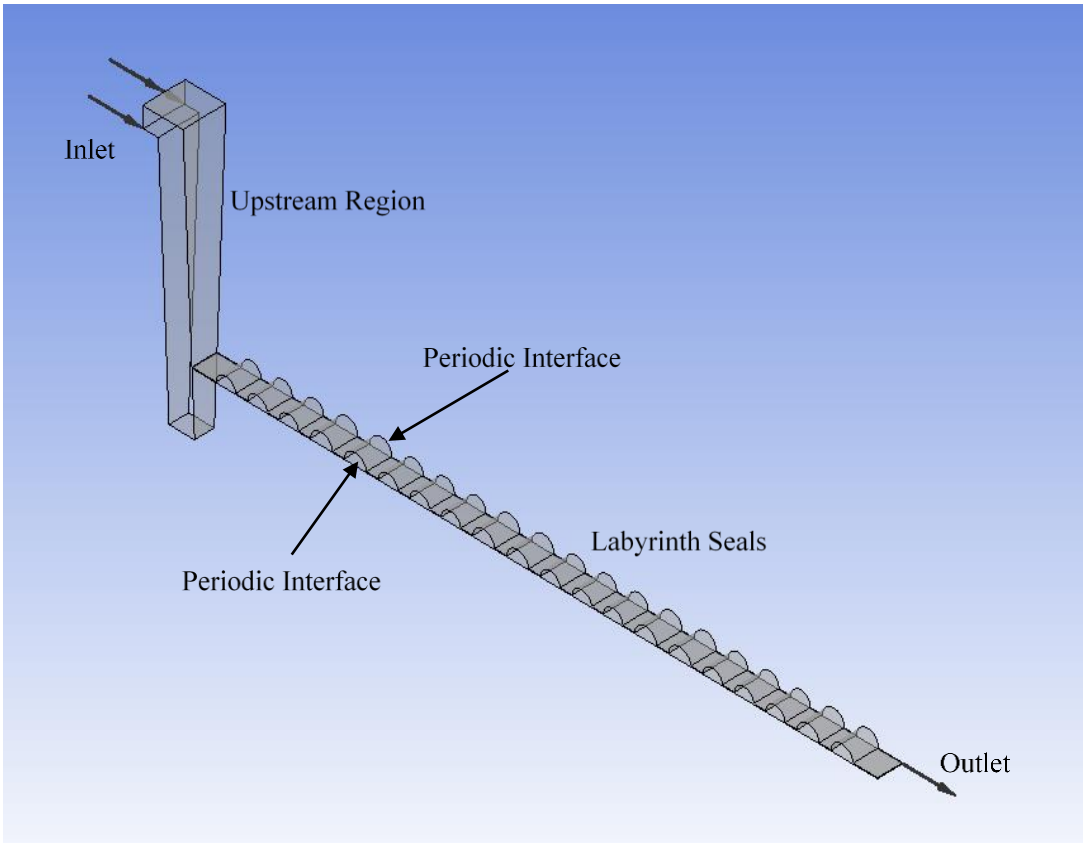

Figure 5-15 CFD Model and Boundary Conditions of Selected Labyrinth Seal

5.2.2 Results and Discussion

The steady state solution is used as the initial condition for the transient simulation. Observations of velocity data are extracted from the target plane/volume, which are then used for POD analysis.

For 3D reduced order model, the location of the target volume selected is shown in Figure 5-16. The reconstructed flow field and corresponding vector plot extracted from the CFD results using CFX post-processing tools is shown in Figure 5-17. The flow fields obtained by the two different approaches are consistent to each other.

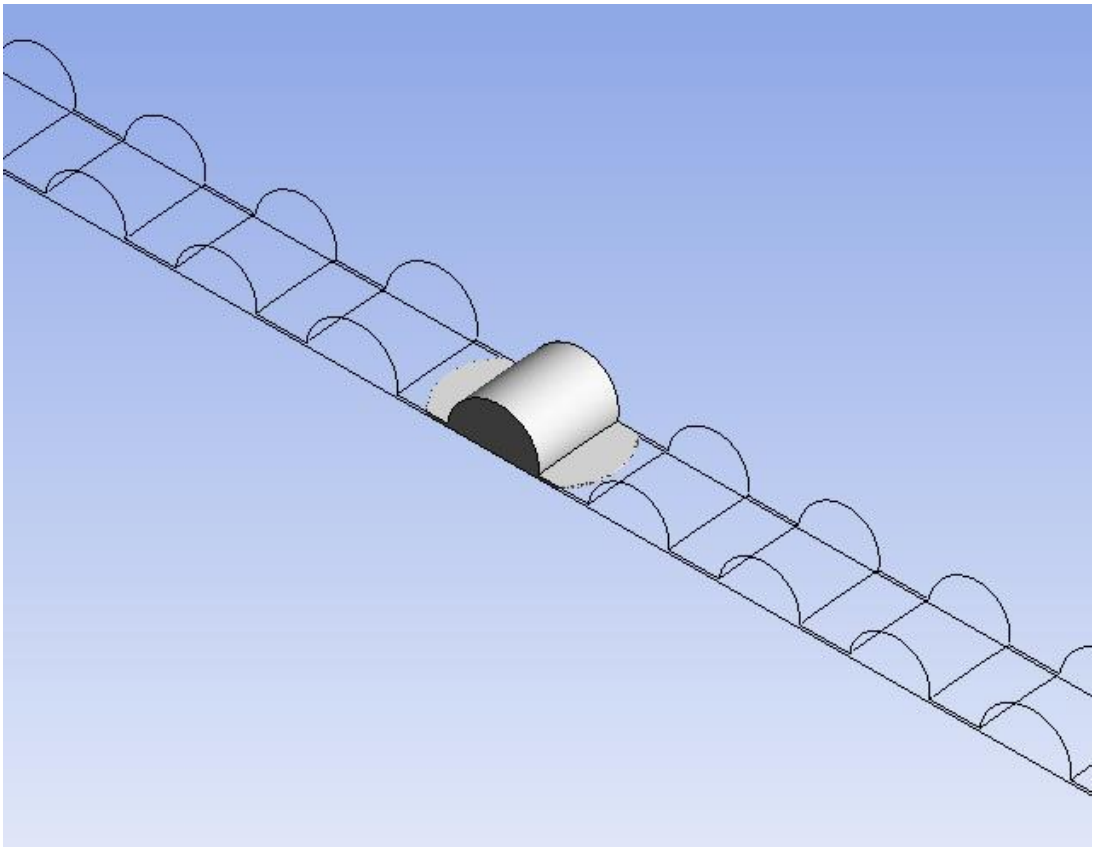

Figure 5-16 Location of the target volume selected

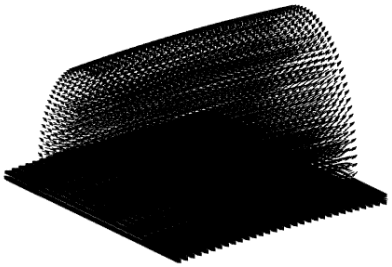

Φ1~60, 3D case

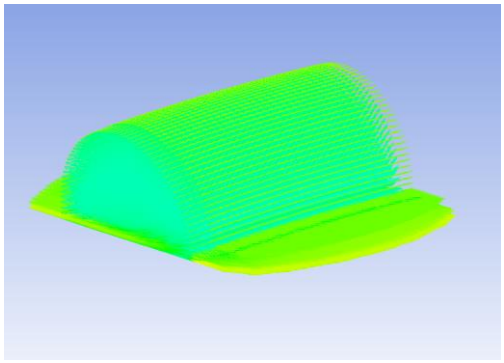

Vector Plot

Figure 5-17 Flow Pattern in Target Volume Selected

However, reconstruction of full 3D reduced order model is very time-consuming due to its high dimensionality. In addition, it is not easy to observe the spatial dominant feature from the 3D plot. Whereas, due to the simple pattern of the velocity profile on YX plane, the analysis of full 3D reduced order model is not necessary. The velocity profile in the plane normal to the axial direction contains only the circumferential velocity and doesn't have complicated flow feature, which is shown in Figure 5-18. The flow pattern reconstructed using POD and the corresponding vector plot from the CFD results are shown in Figure 5-19. The results match fairly well, with no vortices nor complicated flow features in this plane.

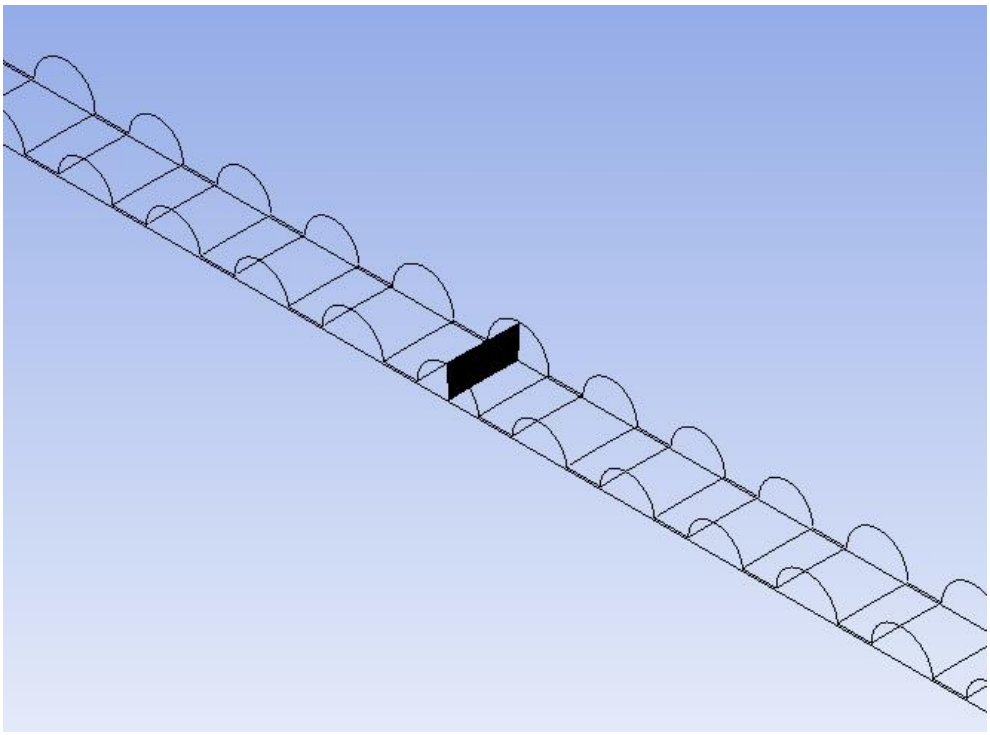

Figure 5-18 Location of the YZ Plane Contains only Circumferential Flow

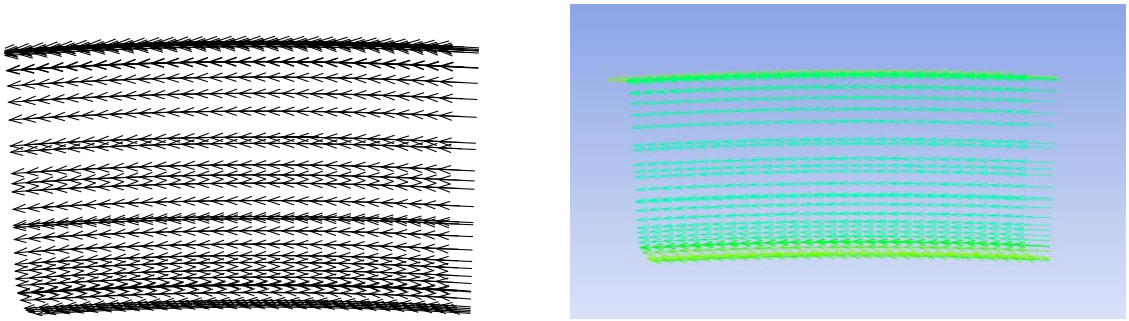

Figure 5-19 Flow Pattern in YZ Plane Contains only Circumferential Flow

The full 3D model, as well as the previous 2D model, are not ideal. The 3D model is very time consuming, while the 2D one cannot capture the dominant flow feature. As a result, one should look at the 2D model corresponding to another plane location. There are 20 grooves in the labyrinth seal and these are numbered from 1 to 20 in ascending order starting from the inlet. The observation plane, as well as five representative grooves (groove 1, 5, 10, 15 and 20), are illustrated in Figure 5-20. These five representative grooves are illustrated with following individual POD basis mode plot and their combination.

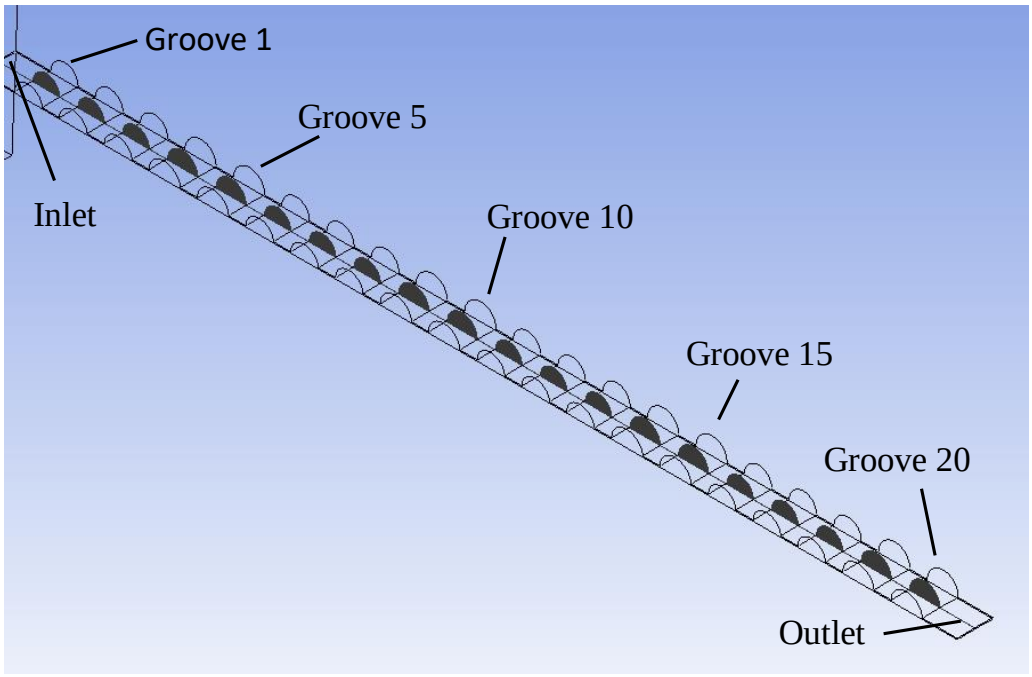

Figure 5-20 Five Representative Groove Locations and Plane used for POD Analysis

Plot of first mode (Φ1), second mode (Φ2), third mode (Φ3), combination of Φ1~3 and combination of Φ1~60 for groove 1 are presented in Figure 5-21. The arrow in the figure is relatively longer if the velocity is higher, which shows the higher velocity regions are much intense than the lower pressure region in the figures. The combination of the modes are generated with Eqn. 1, and the coefficients are obtained by projecting the data set $a_k(t_i) = (u(\boldsymbol{x}, t_i), \phi_k(\boldsymbol{x}))$ on each of the eigenfunctions. A comparison of vector plot from CFX-Post is presented on the right of the Φ 1~60 mode figure, which is consist with the POD results. One can observe that the plots of Φ1, Φ1~3, and Φ1~60 are very similar, which shows the dominance of the first mode. Only one basic vortex located at the center of the groove is observed in the first mode. In addition, the velocity of the fluid in the region below the center of that vortex is much higher than it is in the remaining part of the groove, especially the region near the rotor surface. In the second mode, the energy is not as concentrated near the rotor surface as it is in the first mode and more vortices are formed at corners of the groove. In the third mode, the vortex can be observed more clearly at the left corner of the groove.

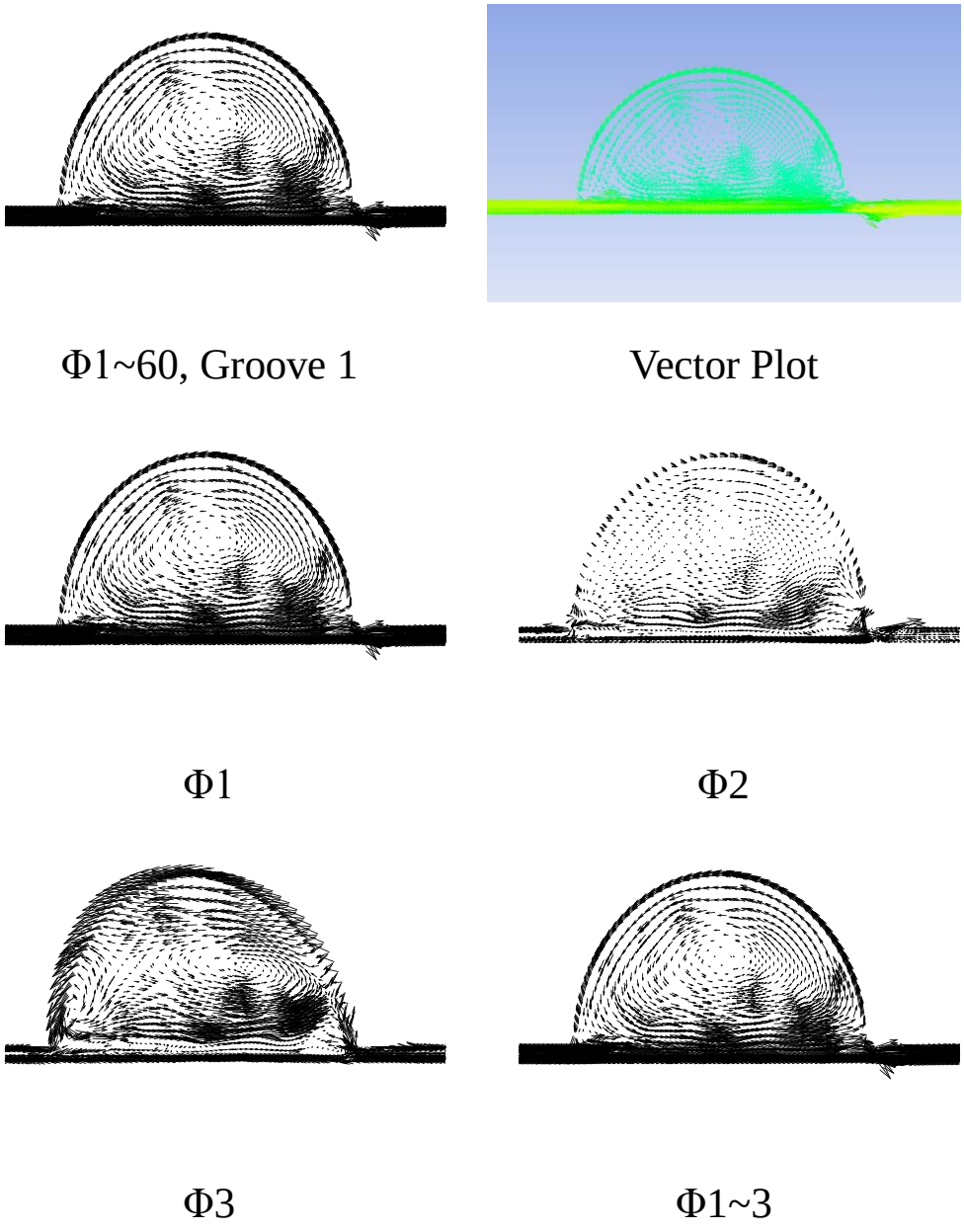

Figure 5-21 Flow Pattern for the First Three Modes of Groove 1

Plots of first mode (Φ1), second mode (Φ2), third mode (Φ3), a combination of Φ1~3 and Φ1~60 for groove 5 are presented in Figure 5-22. The overall spatial dominant feature is very similar to the features observed for groove 1. A comparison of vector plot is shown as well on the right-hand side to the Φ 1~60 mode figure for additional verification of the POD results. Similarly, one can observe that the plots of Φ1, Φ1~3, and Φ1~60 are similar

to each other. In the first mode, only one basic vortex is located at the center of the groove. The energy is also much higher in the region near the rotor surface. In the second mode, the forming of new vortex is slightly faster than that in groove 1. In the third mode, the initial vortex moves a little bit to the right and two more vortices can clearly be observed at the left and right corners.

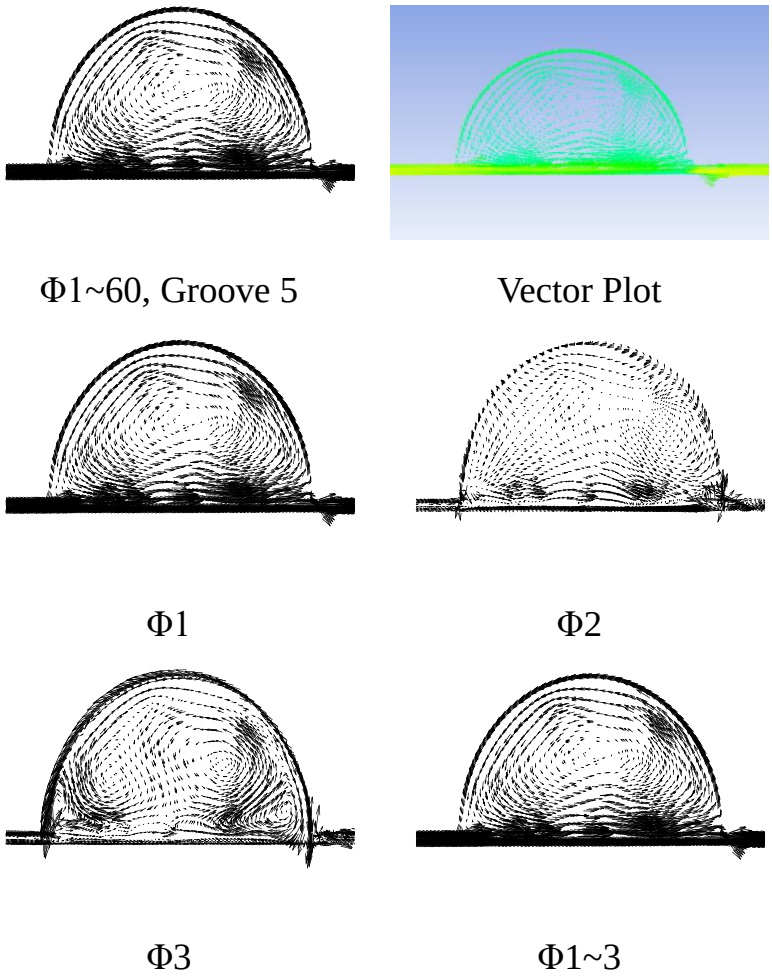

Figure 5-22 Flow Pattern for the First Three Modes in Groove 5

The flow patterns for the other three grooves are presented in Figure 5-23. The dominant flow feature is similar to groove 1 and 5, therefore only Φ1~60 case is given here with the corresponding vector plot from CFX-post. Only one vortex is observed in the plot with all modes (Φ1~60), and the velocity magnitude is much higher near the rotor surface. Similar to the pattern observed in groove 1 and groove 5, the energy concentration is reduced near

the rotor surface as mode number increases. The number of vortices and the overall complexity of the flow pattern increases with the increase in number of modes.

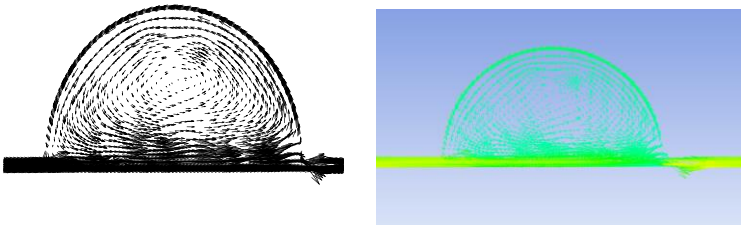

Φ1~60, Groove 10 Vector Plot

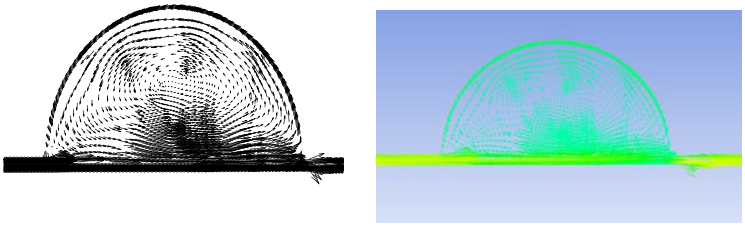

Φ1~60, Groove 15 Vector Plot

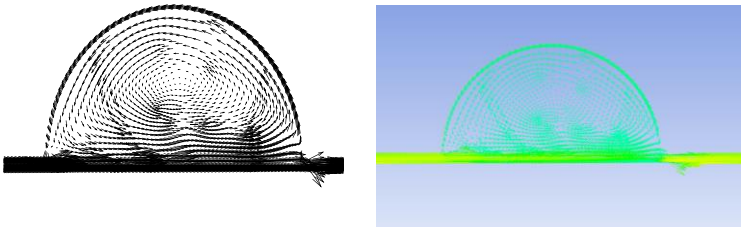

Φ1~60, Groove 20 Vector Plot

Figure 5-23 Flow Pattern in Whole Section 10, 15, 20

The energy levels in all the modes are illustrated in Figure 5-24. Since the distribution of energy among modes for all the grooves is similar, only groove 1, 10 and 20 are presented here. Note that the energy levels are obtained from the eigenvalues thus do not have a unit here. It can be used to obtain the relative energy level. From the log plot, one can observe that the energy exists mostly in the first few modes, especially the first mode. Therefore 3 modes are enough to capture the dominant feature in the flow field. In addition to the

energy levels corresponding to the entire groove (groove and clearance region), the energy corresponding only to the groove (without clearance region) is also plotted for comparison. The energy near the clearance region is relatively high compared to the space inside the groove. For example, the energy level corresponding to the first mode is 2.69×10^{6}, and the energy associated with the groove only is 1.04×10^{6}, which means that 61.3% of the energy is distributed near the rotor surface.

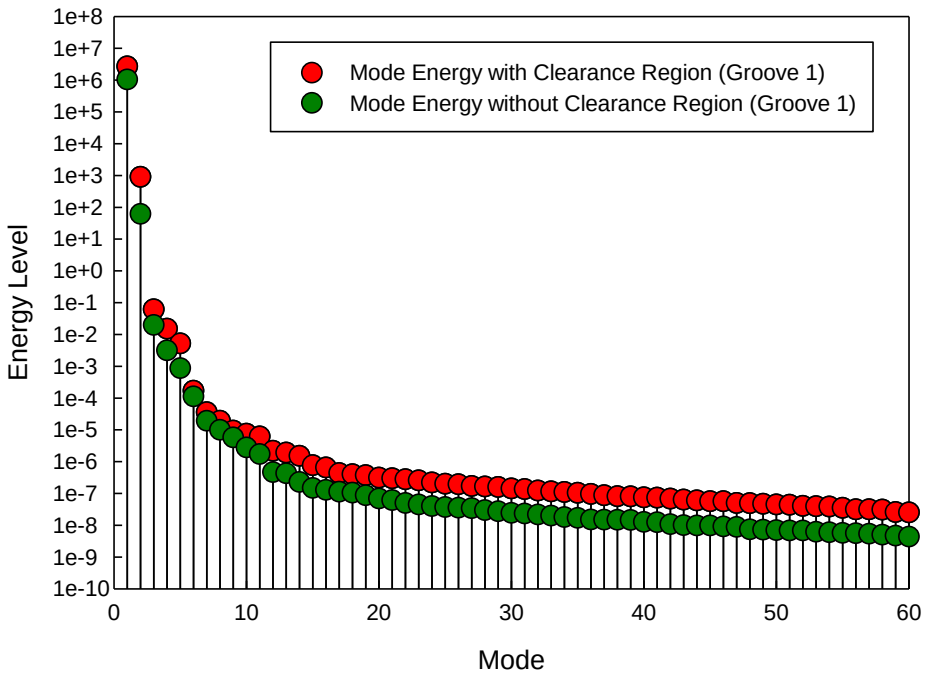

(a)

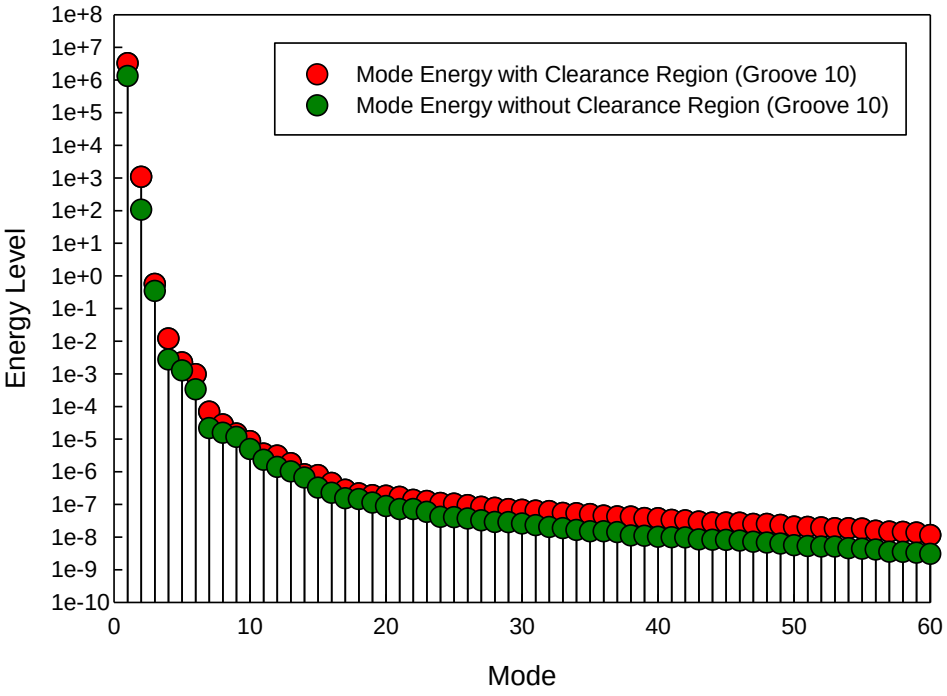

(b)

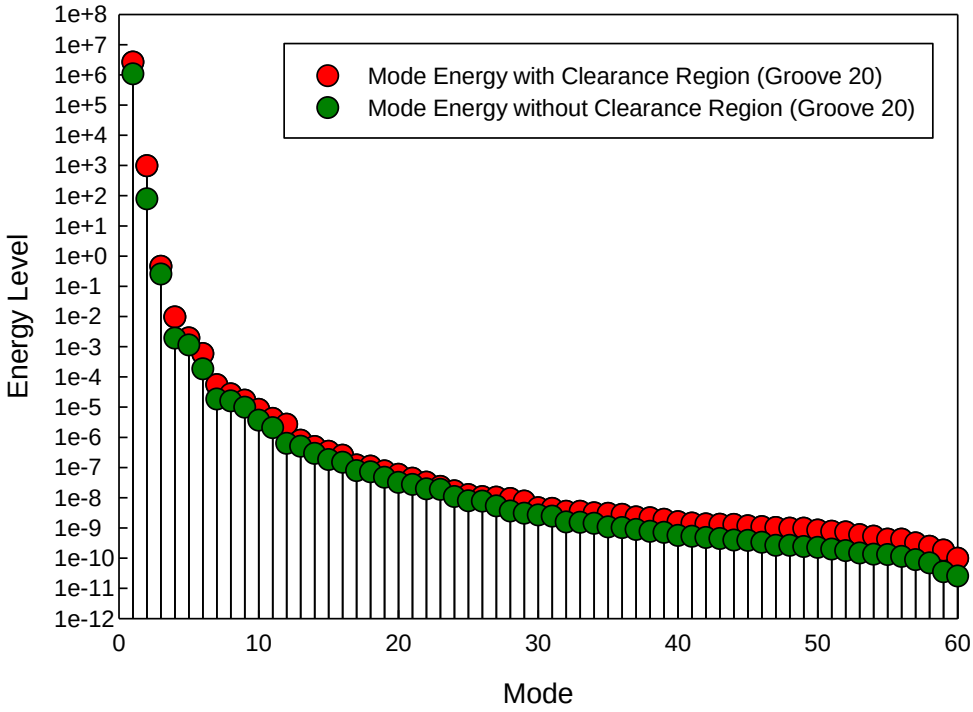

(c)

Figure 5-24 Velocity Magnitude (Energy) in Individual Mode Plot for: (a) Groove 1; (b) Groove 10; (c) Groove 20

The total energy E is obtained by summation of energy levels in all 60 modes. A plot of the total energy for all five grooves is presented in Figure 5-25. Similar to the energy plot for individual modes, the energy levels corresponding only to the grooves are plotted separately as green circle. The energy difference between the two cases is easier to observe here. The energy at the mid-section location of the labyrinth seal (at groove 10) is slightly higher than that at the two ends (at groove 1 and groove 20).

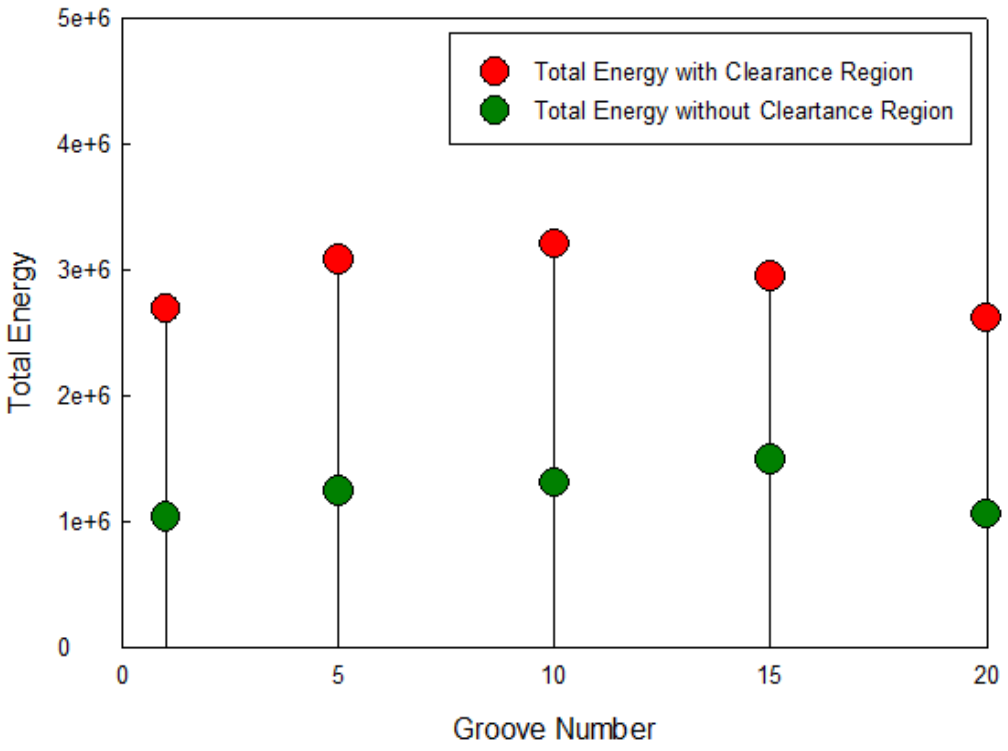

Figure 5-25 Total Energy Plot along Axial Direction

Due to the simple pattern of the flow characteristics in the circumferential direction, the flow field in labyrinth seals can be precisely reconstructed by 2D reduced order models obtained using proper orthogonal decomposition and snapshots technique. Therefore, 3D reduced order models are not necessary for this particular type of seal. The spatial dominant

features of the velocity profile inside the grooves are illustrated accurately from the modes calculated with POD. Most of the energy is present in the first few modes only, and as a result, only these first few modes are needed to recreate the flow field.

Compared to the energy level corresponding to the groove region, the energy level is much higher near the rotor surface, which indicates that the space inside the groove is not efficiently used from the energy distribution standpoint. Future modification of groove geometry can be developed based on this particular observation. This may include groove geometry adjustments that would allow more energy to be associated with the groove region and could have beneficial effects on reducing the leakage rate

5.3 Supercritical Carbon Dioxide used in Annular Pressure Seals

Supercritical state of carbon dioxide process fluid characteristics that benefit high efficiency power cycle. The density of such kind of fluid is relatively high while the viscosity is relatively low. In turbomachinery, the application of supercritical carbon dioxide still needs to be examined for potential system issue, where the leakage rate of rotordynamic components using supercritical carbon dioxide can by higher. In this study, the flow mechanics of a previously used hole-pattern seal example are analyzed to understand more details.

5.3.1 Computational Model

ANSYS CFX package was used in this study to perform the CFD simulations. If the fluid properties are computed through a complex set equation of state, significant time consumption would be expected. In this study, the fluid properties were obtained directly from a set of data tables, which were generated through NIST Reference Fluid Thermodynamic and Transport Properties Database (REPPROP). The mesh and boundary condition setup were similar to the seal model illustrated in chapter III, except the fluid material and inlet/outlet pressure, which is presented in Table 5-1. From the table, it can be observed that the pressure difference was kept same for all three cases, whereas the inlet pressure was increased from 7 Mpa to 8.853 Mpa. This setup was intended to show the

effects of pressure change to the rotordynamic performance when supercritical fluid is involved.

Table 5-1: Boundary Conditions - Supercritical Carbon Dioxide

Run #	Inlet Pressure [Mpa]	Outlet Pressure [Mpa]	Pressure Difference [Mpa]
1	7	3.15	3.85
2	8.115	4.265	3.85
3	8.853	5.003	3.85

The fluid properties of supercritical carbon dioxide were created as a RGP file and directly read by ANSYS CFX during CFD simulation. In this study, the thermal state was assumed to be isothermal, which significantly reduced simulation time. Whereas this setup is only appropriate for early stage of the study, detail analysis should be accomplished with full thermal equation used.

5.3.2 Results and Discussion

The leakage rate performance using supercritical carbon dioxide fluid material for the selected hole-pattern seal model is presented in Table 5-2. From the table, it can observed that the leakage rate from the selected hole-pattern seal showed lower leakage as the pressure increase. Whereas, the effective damping was increased, even if the pressure difference between inlet and outlet kept same for all three cases.

Table 5-2: Leakage Rate Performance – Supercritical Carbon Dioxide

Run #	Leakage [kg/s]	Effective Damping [Ns/m]
1	0.566	11,678
2	0.474	18,491
3	0.333	22,484

The results illustrated potential increase in seal efficiency is likely to be expected when supercritical fluids are used in turbomachinery component. This initial study only examined a simple setup for hole-pattern annular pressure seals. In practice, labyrinth seals were used commonly as well and the pressure difference may not be kept same as the pressure increased. In this case, the flow can be choked and the fluid phase may change

between supercritical phase and vapor phase. A thorough study may require transient simulation to capture the details of the flow characteristics.

Chapter 6. Conclusion and Future Work

6.1 Conclusion

In this dissertation, the effects of the surface patterning on different types of the annular pressure seals were investigated to understand the rotordynamic response related to different geometry variations. The stability issue, which can be illustrated from the rotordynamic coefficients and swirl ratio inside the cavities, was addressed with design of experiments technique and hybrid CFD/bulk flow method. For each different type of the annular pressure seals, a CFD computational model and parametrization of the geometry was presented to construct design of experiments model. CFD simulations was conducted to further understand the flow characteristics inside the annular pressure seals. The results of the CFD simulations were used to extract related flow variables as replacement of solution for the zeroth order bulk-flow equations to increase the accuracy of rotordynamic coefficients computations compared to conventional bulk-flow method. The corresponding results were illustrated by regression models that did not exist before this study and provide a basis for future use as guidelines for annular pressure seal design in the future. For instance, the regression models can be used as tools at the designing stage to obtain an estimation of the rotordynamic coefficients for a given geometry. Therefore, the stability of the annular pressure seals can be estimated. If the system has a relatively low effective damping, the current geometry should be improved immediately instead of solving it at later designing stages, which would be much less efficient. The idea to develop regression models could be applied to other turbomachinery component. For the annular pressure seals, the comparison of design procedures with and without the regression models is illustrated in Figure 6-1.

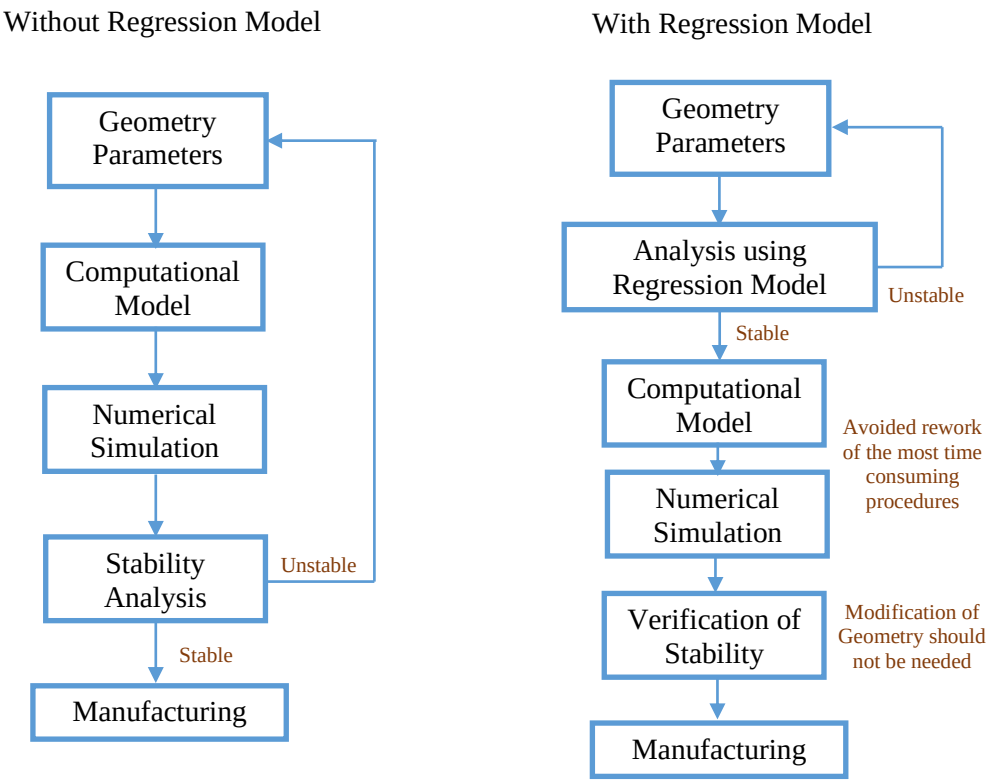

Figure 6-1 Simplified Annular Pressure Seal Design Procedures using Regression Models

For hole-pattern seal, corresponding regression model of leakage rate performance and rotordynamic coefficients are presented. The effective damping coefficients were summarized to give an overall estimation of the stability property in the component. For labyrinth seals, the effects of swirl brakes were illustrated to reduce the swirl ratios across the seal and in some cases reducing the circumferential velocity to negative values at the seal inlet. Therefore, the stability of the turbomachinery component may be changed from unstable to stable. Leakage rate performance was presented as a result of the geometry variation.

Some related studies were conducted in addition to better understand the challenges related to annular pressure seal design and to facilitate future studies in this field. The reduced order model of both hole-pattern seals and labyrinth seals were illustrated. The results

showed that the flow field representing the flow dynamics in annular pressure seals can be expressed as a combination of first three POD modes. In higher Reynolds number cases, more POD modes may be required to obtain relevant reduced order models. In labyrinth seals, the results showed that 2D reduced order model was enough to reconstruct the flow field and 3D models were not necessary. The energy distribution across the cavity and clearance region provided the idea that potential improvement of performance in seal design is totally possible. In addition, sCO_2 was examined as the working fluid in a hole-pattern seal. This initial study aimed to better understand the effects on annular pressure seals as the density of such fluid state is relatively high while the viscosity is relatively low. The initial results showed that the performance and stability in the annular pressure seals can be improved by using sCO_2. Potential improvement when supercritical fluid being used should be based on high accuracy CFD simulation.

6.2 Future Work

Several potential extensions of this work are interesting to investigate and can be fulfilled in the future. Detailed rotordynamic coefficients in labyrinth seals based on three control-volume method can be illustrated with more details by either further developeing hybrid CFD/bulk flow method or full 3D-CFD simulation. Reduced order modeling used in Chapter V can also be used to accelerate the CFD process and achieve much higher efficiency in seal design. However, commercial CFD software may not be feasible any longer since modification of the governing equations might be required. More detailed supercritical CO_2 material properties used in the annular pressure seals can be achieved through the modeling of temperature variation and performing transient simulations at designing stage.

References

[1] Childs, D. W., Mclean, J. E., Zhang, M., and Arthur, S. P., 2016, "Rotordynamic Performance of a Negative-Swirl Brake for a Tooth-on-Stator Labyrinth Seal," J Eng Gas Turb Power, 138(6), p. 062505.

[2] Alford, J. S., 1965, "Protecting turbomachinery from self-excited rotor whirl," Transactions of the ASME Journal of Engineering for Power, pp. 333-444.

[3] Childs, D., and Moyer, D., 1985, "Vibration Characteristics of the HPOTP High Pressure Oxygen Turbopump) of the SSME (Space Shuttle Main Engine)," ASME J. Eng. Gas Turbines Power, 107, pp. 152-159.

[4] Childs, D. W., 1993, Turbomachinery Rotordynamics-Phenomena, Modeling, and Analysis, John Wiley & Sons, Inc.

[5] Kostyuk, A. G., 1972, "A theoretical analysis of the aerodynamic forces in the labyrinth glands of turbomachines," Teploenergetica, 419(11), pp. 29-33.

[6] Hirs, G. G., 1973, "A Bulk-Flow Theory for Turbulence in Lubrication Technology," Journal of Lubrication Technology, 95(137-146).

[7] Iwatsubo, T., 1980, "Evaluation of instability forces of labyrinth seals in turbines or compressors," NASA Conference Publication, 2133: Rotordynamic Instability Problems in High-Performance Turbomachinery, pp. 139-168.

[8] Childs, D. W., 1986, "An Iwatsubo-based solution for labyrinth seals: Comparison to experimental results," Journal of Engineering for Gas Turbines and Power, 108, pp. 325-331.

[9] Rosen, M. C., 1986, "Calculation of leakage and stiffness/damping coefficients for compressible flow in straight-throught labyrinth seals: User's guide for pro-gram LABY2 Report No. UVA/643092/MAE86/346," University of Virgina.

[10] W., C. D., and J.K., S., 1988, "Theory Versus Experiment for the Rotordynamic Coefficients of Labyrinth Gas Seals," Journal of Vibration, 110, pp. 281-287.

[11] Rajakumar, C., and Sisto, F., 1988, "Labyrinth Seal Force Coefficients for Small Motion of the Rotor about an Arbitrary Eccentric Position," ASME Gas Turbine Conference, 88(G7), p. 194.

[12] P., W. B., 1992, "The calculation of Rotordynamic Coefficients for Labyrinth Seals," Master, University of Virginia.

[13] Iwatsubo, T., N., Motooka, and Kawai, R., 1982, "Flow Induced force of labyrinth seal," NASA Conference Publication, 2250: Rotordynamic Instability Problems in High-Performance Turbomachinery, pp. 205-222.

[14] Wyssmann, H. R. T. C. P., and R. J. Jenny., 1984, "Prediction of stiffness and damping coefficients for centrifugal compressor labyrinth seals.," ASME Journal of Engineering for Gas Turbines and Power, 106, pp. 920-926.

[15] Scharrer, and K., J., 1988, "Theory Versus Experiment For The Rotordynamic Coefficients Of Labyrinth Gas Seals. Part I: A Two Control Volume Model," Journal of Vibration, 110, pp. 270-280.

[16] Rhode, D. L., and Sobolik , S. R., 1986, "Simulation of Subsonic Flow Through a Geneic Labyrinth seal," ASME Journal of Engineering for Gas Turbines and power, 108, pp. 674-680.

[17] Nordmann, R., and Weiser., P., 1990, "Evaluation of rotordynamic coefficients of straight-through labyrinths by means of a three volume bulk flow model," NASA Conference Publication, 3122: Rotordynamci Instability Problems in High-Performance Turbomachinery.
[18] S., L. Y. M. M., and D., B. R., 1984, "Experimental investigations of lateral forces induced by flow through model labyrinth glands," NASA Conference Publication, 2338: Rotordynamci Instability Problems in High-Performance Tur-bomachinery.
[19] Nordmann, R., Dietzen, F. J., Janson, W., and Florjancic, S., "Rotordynamics Coefficients and leakage Flow of Parallel Grooved Seals and smooth seals.," Proc. Rotordynamic Instability problem in high-performance turbomachinery, NASA CP No. 2338, pp. 129-153.
[20] Nordmann, R., and Weiser, P., 1988, "Rotordynamic coefficients for labyrinth seals calculated by means of a ¯nite difference technique," NASA Conference Publication, 3026: Rotordynamci Instability Problems in High-Performance Tur-bomachinery.
[21] Nordmann, R., and Weiser, P., 1990, "Evaluation of rotordynamic coefficients of straight-through labyrinths by means of a three volume bulk flow mode," NASA Conference Publication, 3122: Rotordynamci Instability Problems in High-Performance Turbomachinery.
[22] R., M. O., and W.6., C. D., 1996, "An Extended Three-Control-Volume Theory for Circumferentially-Grooved Liquid Seals," Journal of Tribology, 118, pp. 276-285.
[23] Dietzen, F. J., and Nordmann, R., 1988, "A three-dimensional finite difference method for calculating the dynamic coefficients of seals," NASA Conference Publication, 3026: Rotordynamic Instability problems in High-Performance Tur-bomachinery, pp. 211-228.
[24] Stocker, H., 1978, "Determining labyrinth seal performance in current and ad-vanced high performance gas turbines."
[25] Benckert, H., and Wachter, J., "Flow induced spring coe±cients of labyrinth seals for application in rotor dynamics.," Proc. NASA Conference Publication, pp. 189-212.
[26] V., W. D., "Labyrinth seal forces on a whirling rotor," Proc. Proceedings of the ASME Applied Mechanics, Bioengineering and Fluids Engineering Conference.
[27] W., C. D., and J.K., S., 1986, "Experimental Rotordynamic Coefficients Results for Teeth-on-rotor and Teeth-on-stator Labyrinth Gas Seals," Journal of Engineeringfor Gas Turbines and Power, 108, pp. 599-604.
[28] Y., K., and M., O., "Experimetnal Study on Flow-Induced Force of Labyrinth Seal," Proc. IFToMM, pp. 106-112.
[29] Hisa, S., Sahakida, H., Asata, S., and Sakamoto, T., "Steam Excited Vibration in Rotor-bearing System," Proc. proceedings of the IFToMM International Conference, pp. 635-641.
[30] Marquette, O. R., and Child, D. W., 1996, "An Extended Three-Control-Volume Theory for Circumferentially-Grooved Liquid Seals," Journal of Tribology, 118, pp. 276-285.
[31] Prasad, B. V. S. S. S., Manavalan, V. S., and Rao, N. N., 1997, "Computational and experimental investigations of straight-through labyrinth seals," International Gas Turbine & Aeroengine congress & ExhibitionOralndo, Florida.
[32] G.L., M., M.C., J., and G.B., T., 1991, "3-D Laser Anemometer Measurements in a Labyrinth Seal," Journal of Engineering for Gas Turbines and Power, 113, pp. 119-125.
[33] G.L., M., and M.C., J., 1997, "Upstream Swirl Effects on the Flow In-side a Labyrinth Seal," National Aeronautics and Space Administration.
[34] K., K., 1997, "Dynamic coefficients of stepped labyrinth gas seals," International Gas Turbine & Aeroengine Congress & Exhibition.
[35] Soto, E. A., and Childs, D. W., 1999, "Experimental rotordynamic coefficient results for (a) a labyrinth seal with and without shunt injection and (b) a honeycomb seal," 121, p. 153.

[36] Hirano, T., Guo, and Z., K., R.G., "Application of CFD Analysis for Rotating Machinery, Part 2: Labyrinth Seal Analysis," Proc. Proceedings of ASME Turbo Expo 2003.
[37] Dietzen, F. J., and Nordmann, R., 1987, "Calculating Rotordynamic Coefficients of Seals by Finite-Difference Techniques," ASME J. Tribol, 109(3), pp. 388-394.
[38] Rhode, D. L., Hensel, S. J., and Guidry, M. J., 1992, "Labyrinth Seal Rotordynamic orces Using a Three-Dimensional Navier-Stokes Code," ASME J. Tribol, 14(4), pp. 683-689.
[39] Athavale, M. M., and Hendricks, R., 1996, "A Small Perturbation CFD Method for Calculation of Seal Rotordynamic Coefficients," Int. J. Rotating Mach, 2(3), pp. 167-177.
[40] Moore, J. J., 2003, "Three-Dimensional CFD Rotordynamic Analysis of Gas Labyrinth Seals," ASME J. Vib. Acoust, 125(4), pp. 427–433.
[41] Untaroiu, A., Migliorini, P., Wood, H. G., Allaire, P. E., and Kocur, J. A., "Hole-Pattern Seals: A Three Dimensional CFD Approach for Computing Rotordynamic Coefficient and Leakage Characteristics," Proc. ASME Conference Proceedings, pp. 981-990.
[42] Untaroiu, A., Dimond, T. W., Allaire, P. E., and Armentrout, R., 2009, "CFD Analysis of a Canned Pump Rotor Considering an Annular Fluid With Axial Flow," ASME Conference Proceedings, 48876, pp. 1013-1022.
[43] Chochua, G., and Soulas, T. A., 2007, "Numerical Modeling of Rotordynamic Coefficients for Deliberately Roughened Stator Gas Annular Seals," ASME J. Tribol., 129(2), pp. 424-429.
[44] Childs, D. W., and Wade, J., 2004, "Rotordynamic-Coefficient and Leakage Characteristics for Hole-Pattern-Stator Annular Gas Seals—Measurements Versus Predictions," ASME J. Tribol., 126(2), pp. 326-333.
[45] Yan, X., Li, J., and Feng, Z., 2011, "Investigations on the Rotordynamic Characteristics of a Hole-Pattern Seal Using Transient CFD and Periodic Circular Orbit Model," ASME J. Vib. Acoust, 133(4), p. 041007.
[46] Kleynhans, G. F., 1996, "A Two-Control-Volume Bulk-Flow Rotordynamics Analysis for Smooth-Rotor/Honeycomb-Stator Gas Annular Seals," Ph.D., Texas A&M University.
[47] Sirovich, L., 1987, "Turbulence and the dynamics of coherent structures," Quarterly of Applied Mathematics, 45(3), pp. 451-590.
[48] Kirby, M., Boris J. P., 1990, "A Proper Orthogonal Decomposition of a Simulated Supersonic Shear Layer," International Journal for Numerical Methods in Fluids, 10(4), pp. 411-428.
[49] Cizmas, P. G. A., and C., H. K., 1995, "Computation of steady and unsteady viscous Flows Using a Simultaneously Coupled Inviscid-viscous Interaction Technique," Journal of Fluids and Structures, 9, pp. 639-657.
[50] Ito, K., and Ravindran, S. S., 1998, "A Reduced-Order Method for Simulation and Control of Fluid Flows," Journal of Computational Physics, 143(2), pp. 403-425.
[51] Cizmas, P. G. A., Palacios, A., and O'Brien, T., 2003, "Proper-Orthogonal Decomposition of Spatio-Temporal Patterns in Fluidized Beds," Chemical Engineering Science, 58(19), pp. 4417-4427.
[52] Puragliesi, R., and Leriche, E., 2012, "Proper Orthogonal Decomposition of a Fully Confined Cubical Differentially Heated Cavity Flow at Rayleigh Number Ra =109," Computers & Fluids, 61, pp. 14-20.
[53] Iliescu, T., and Wang, Z., 2013, "Variational multiscale proper orthogonal decomposition: Navier ‐ stokes equations," Numerical Methods for Partial Differential Equations.
[54] Iliescu, T., Liu, H., and Xie, X., 2017, "Regularized Reduced Order Models for a Stochastic Burgers Equation," arXiv:1701.01155v1 [physics.flu-dyn].

[55] Daniel, C., 1976, Applications of Statistics to Industrial Experimentation, John Whiley & Sons, Inc, New York.
[56] Box, G. E. P., Hunter, J. S., and Hunter, W. G., 2005, Statistics for Experimenters. Design, Innovation, and Discovery 2nd ed., John Wiley & Sons, Inc., Hoboken, NJ.
[57] Fisher, R. A., 1974, Design of Experiments, Hafner Press, New York.
[58] Untaroiu, A., Liu, C., Migliorini, P. J., W., H. G., and Untaroiu, C. D., 2013, "Hole-Pattern Seals Performance Optimization Using Computational Fluid Dynamics and Design of Experiment Techniques," ASME Proceedings 2013, p. V07BT08A058.
[59] Liu, C., Untaroiu, A., Wood, H. G., Yan, Q., and Wei, W., 2015, "Parametric Analysis and Optimization of Inlet Deflection Angle in Torque Convertors," J. Fluids Eng., 137(3), p. 031101.
[60] Wu, J., Antaki, J. F., V., J., S., S., and Ricci, M., "Computational Fluid Dynamics-Based Design Optimization for an Implantable Miniature Maglev Pediatric Ventricular Assist Device," J. Fluids Eng. , 134(4), p. 041101.
[61] Morgan, N. R., Wood, H. G., and Untaroiu, A., 2016, "Design of Experiments to Investigate Geometric Effects on Fluid Leakage Rate in a Balance Drum Seal," J. Eng. Gas Turbines Power, 138(7), p. 072506.
[62] Strasser, W., 2007, "CFD Investigation of Gear Pump Mixing Using Deforming/Agglomerating Mesh," ASME J. Fluids Eng., 129(4), pp. 476-484.
[63] Migliorini, P. J., Untaroiu, A., and Wood, H. G., 2012, "A Computational Fluid Dynamics/Bulk-Flow Hybrid Method for Determining Rotordynamic Coefficients of Annular Gas Seals," ASME J. Tribol, 134(2), p. 022202.
[64] Yu, Z., and Childs, D. W., 1998, "A Comparison of Experimental Rotordynamic Coefficients and Leakage Characteristics between Hold-Pattern Gas Damper Seals and Honeycomb Seal," ASME J. Eng. Gas Turb. Power, 120(10), pp. 778-783.
[65] Untaroiu, A., Liu, C., Migliorini, P. J., Wood, H. G., and Untaroiu, C. D., 2014, "Hole-Pattern Seals Performance Evaluation Using Computational Fluid Dynamics and Design of Experiment Techniques," J Eng Gas Turb Power, 136(10), p. 102501.
[66] Untaroiu, A., Untaroiu, C. D., Wood, H. G., and Allaire, P. E., 2013, "Numerical Modeling of Fluid-Induced Rotordynamic Forces in Seals With Large Aspect Ratios," J Eng Gas Turb Power, 135(1), p. 012501.
[67] Morgan, N. R., Wood, H. G., and Untaroiu, A., "Numerical Optimization of Leakage by Multifactor Regression of Trapezoidal Groove Geometries for a Balance Drum Labyrinth Seal," Proc. ASME Turbo Expo, p. V02CT45A021.
[68] Migliorini, P. J., Untaroiu, A., and Wood, H. G., 2015, "A Numerical Study on the Influence of Hole Depth on the Static and Dynamic Performance of Hole-Pattern Seals," J Tribol-T, 137(1), p. 011702.
[69] Jin, H. X., and Untaroiu, A., "Elliptical Shape Hole-Pattern Seals Performance Evaluation Using Design of Experiments Technique," Proc. Proceeding of the Asme Fluids Engineering Division Summer Meeting, p. V01AT03A013.
[70] Childs, D. W., Mclean, J. E., Zhang, M., and Arthur, S. P., 2016, "Rotordynamic Performance of a Negative-Swirl Brake for a Tooth-on-Stator Labyrinth Seal," J Eng Gas Turb Power, 138(6).
[71] Moreland, J., Childs, D. W., and Bullock, J. T., "Measured Static And Rotordynamic Characteristics Of a Smooth-Stator/Grooved-Rotor Liquid Annular Seal," Proc. ASME Fluids Engneering Division Summer Meeting.

[72] Childs, D. W., and Scharrer, J. K., 1998, "Theory Versus Experiment for the Rotordynamic Coefficient of Labyrinth Gas Seals: Part II—A Comparison to Experiment," ASME J. of Vibration Acoustics, Stress and Reliability in Design, 110(3).
[73] Picardo, A., and Childs, D. W., 2005, "Rotordynamic Coefficients for a Tooth-on-Stator Labyrinth Seal at 70 Bar Supply Pressures: Measurements Versus Theory and Comparisons to a Hole-Pattern Stator Seal," ASME J. of Engineering for Gas Turbines and Power, 127(4).
[74] Untaroiu, A., Hayrapetian, V., Untaroiu, C. D., Wood, H. G., Schiavello, B., and McGuire, J., 2013, "On the Dynamic properties of pump liquid seals," ASME Journal of Fluids Engineering, 135(5), p. 051104.

Appendix A: Copyright Release

Chapter 3.1 of this dissertation was reproduced from Jin, H., Untaroiu, A., 2018, Elliptical Shape Hole-Pattern Seals Performance Evaluation Using Design of Experiments Technique. J. Fluids Eng 140(7), 071101, with the permission of AIP Publishing.
Detailed information on the copyright policy of AIP Publishing can be found on https://publishing.aip.org/resources/researchers/rights-and-permissions/permissions/.
The original publication can be accessed at: https://doi.org/10.1115/1.4039249

Chapter 3.2 of this dissertation was reproduced from Jin H, Fu G, Untaroiu, A. Effect of Surface Patterning on the Dynamic Response of Annular Hole-Pattern Seals. Proceedings of the ASME 2017 Turbo Expo 2017: Structure and Dynamics, Paper no. GT2017-64875, June 26-30, 2017, Charlotte, North Carolina, with the permission of AIP Publishing.
Detailed information on the copyright policy of AIP Publishing can be found on https://publishing.aip.org/resources/researchers/rights-and-permissions/permissions/.
The original publication can be accessed at: https://doi.org/10.1115/1.4039249

Chapter 4.1 of this dissertation was reproduced from Jin, H, Untaroiu, A., Hayrapetian, V, Elebiary, K, 2018, The effects of Fluid Pre-Swirl and Swirl Brakes Design on the Performance of Labyrinth Seals. Journal of Engineering for Gas Turbines and Power. 140(8), 082503, with the permission of AIP Publishing.
Detailed information on the copyright policy of AIP Publishing can be found on https://publishing.aip.org/resources/researchers/rights-and-permissions/permissions/.
The original publication can be accessed at: https://doi.org/10.1115/1.4039249

Chapter 4.2 of this dissertation was reproduced from Jin, H, Untaroiu, A, Leakage Rate Performance Mapping of Smooth Stator/Grooved Rotor Labyrinth Seals Using Statistical Tools. ASME - JSME - KSME Joint Fluids Engineering Conference, AJKFLUIDS 2019, Paper no. AJKFLUIDS2019-5429, July 28- August 1, 2019, Hyatt Regency (Downtown), San Francisco, CA, with the permission of AIP Publishing.